January 2017

A Comprehensive Analysis Of Clouds, Radiation, And Precipitation In The North Pacific Itcz In The NASA GISS Modele GCM And Satellite Observations

Ryan Evan Stanfield

Follow this and additional works at: https://commons.und.edu/theses

A Comprehensive Analysis of Clouds, Radiation, and Precipitation in the North Pacific
ITCZ in the NASA GISS ModelE GCM and Satellite Observations

by

Ryan Evan Stanfield
Bachelor of Science, Texas A&M University, 2008
Master of Science, University of North Dakota, 2012

A Dissertation

Submitted to the Graduate Faculty

of the

University of North Dakota

in partial fulfillment of the requirements

for the degree of

Doctor of Philosophy

Grand Forks, North Dakota
August
2017

This dissertation, submitted by Ryan E. Stanfield in partial fulfillment of the requirements for the Degree of Doctor of Philosophy from the University of North Dakota, has been read by the Faculty Advisory Committee under whom the work has been done and is hereby approved.

_____
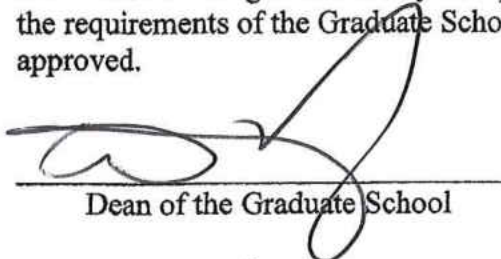Xiquan Dong
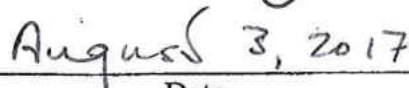
_____
Baike Xi

_____
Aaron Kennedy

_____
Jonathan Jiang

_____
Tony Del Genio

_____
Enru Wang

This thesis is being submitted by the appointed advisory committee as having met all of the requirements of the Graduate School at the University of North Dakota and is hereby approved.

_____
Dean of the Graduate School

August 3, 2017
_____
Date

iii

PERMISSION

Title   A Comprehensive Analysis of Clouds, Radiation, and Precipitation in the North Pacific ITCZ in the NASA GISS ModelE GCM and Satellite Observations

Department   Atmospheric Sciences

Degree   Doctor of Philosophy

In presenting this dissertation in partial fulfillment of the requirements for a graduate degree from the University of North Dakota, I agree that the library of this University shall make it freely available for inspection. I further agree that permission for extensive copying for scholarly purposes may be granted by the professor who supervised my dissertation work or, in his absence, by the chairperson of the department or the dean of the Graduate School. It is understood that any copying or publication or other use of this dissertation or part thereof for financial gain shall not be allowed without my written permission. It is also understood that due recognition shall be given to me and to the University of North Dakota in any scholarly use which may be made of any material in my dissertation.

Signature   Ryan Stanfield

Date   May 31st, 2017

TABLE OF CONTENTS

LIST OF FIGURES

LIST OF TABLES

ABSTRACT

Global circulation/climate models (GCMs) remain as an invaluable tool to predict future potential climate change. To best advise policy makers, assessing and increasing the accuracy of climate models is paramount. The treatment of clouds, radiation and precipitation in climate models and their associated feedbacks have long been one of the largest sources of uncertainty in predicting any potential future climate changes.

Three versions of the NASA GISS ModelE GCM (the frozen CMIP5 version [C5], a post-CMIP5 version with modifications to cumulus and boundary layer turbulence parameterizations [P5], and the most recent version of the GCM which builds on the post-CMIP5 version with further modifications to convective cloud ice and cold pool parameterizations [E5]) have been compared with various satellite observations to analyze how recent modifications to the GCM has impacted cloud, radiation, and precipitation properties. In addition to global comparisons, two areas are showcased in regional analyses: the Eastern Pacific Northern ITCZ (EP-ITCZ), and Indonesia and the Western Pacific (INDO-WP).

Changes to the cumulus and boundary layer turbulence parameterizations in the P5 version of the GCM have improved cloud and radiation estimations in areas of descending motion, such as the Southern Mid-Latitudes. Ice particle size and fall speed modifications in the E5 version of the GCM have decreased ice cloud water contents and cloud fractions globally while increasing precipitable water vapor in the model.

Comparisons of IWC profiles show that the GCM simulated IWCs increase with height and peak in the upper portions of the atmosphere, while 2C-ICE observations peak in the lower levels of the atmosphere and decrease with height, effectively opposite of each other. Profiles of CF peak at lower heights in the E5 simulation, which will potentially increase outgoing longwave radiation due to higher cloud top temperatures, which will counterbalance the decrease in reflected shortwave associated with lower CFs and the thinner optical depths associated with decreased IWC and LWC in the E5 simulation.

Vertical motion within the newest E5 simulation is greatly weakened over the EP-ITCZ region, potentially due to atmospheric loading from enhanced ice particle fall speeds. Comparatively, E5 simulated upward motion in the INDO-WP is stronger than its predecessors. Changes in the E5 simulation have resulted in stronger/weaker upward motion over the ocean/land in the INDO-WP region in comparison with both the C5 and P5 predecessors.

Multimodel precipitation analysis shows that most of the GCMs tend to produce a wider ITCZ with stronger precipitation compared to GPCP and TRMM precipitation products. E5-simulated precipitation decreases and shifts Southward over the Easter Pacific ITCZ, which warrants further investigation into meridional heat transport and radiation fields.

CHAPTER I

INTRODUCTION

Statement of Problem

The treatment of clouds and precipitation in climate models and their associated feedbacks have long been one of the largest sources of uncertainty in predicting any potential future climate changes. Although many improvements have been made in Phase 5 of the Coupled Model Intercomparison Project (CMIP5) (Lauer and Hamilton 2012; Wang and Su 2013; Li et al. 2013; Klein et al. 2013; Chen et al. 2013; Stanfield 2012), clouds, precipitation, and their feedbacks are still a problem in climate models as concluded in the Intergovernmental Panel on Climate Change (IPCC) 5th Assessment Report (AR5) (2013), and have been illustrated in many studies (e.g., Jiang et al. 2012; Stanfield et al. 2014, 2015, and 2016; Dolinar et al. 2015a&b).

Clouds and Radiation

Lauer and Hamilton (2012) have revealed that the model simulated cloud radiative effects (CREs) tend to outperform cloud fractions (CFs), suggesting that models are not accurately depicting fundamental cloud processes; rather, the models are being tuned to provide simulations closer to observations. Jiang et al. (2012) developed a grading scale to rate each model based upon spatial mean, standard deviation, and correlation, and highlighted that there exists a large spread in the models and a high

1

degree of discrepancy from observations, particularly in the upper troposphere. Dolinar et al. (2015a) evaluated 28 CMIP5 AMIP GCMs simulated CFs and concluded that the multi-model ensemble mean CF (57.6%) is, on average, underestimated by 7.6% when compared to CERES-MODIS results between 65° S and 65° N. What makes this particularly interesting is that many studies have shown that there is a good agreement between GCMs simulations and observations in the radiation budget at the top-of-the-atmosphere (TOA) (Dolinar et al. 2015a&b; Stanfield et al. 2015).

Precipitation

As described in chapter 9 of the IPCC AR5 (Flato et al. 2013), the majority of the general circulation models (GCMs) underestimate the sensitivity of extreme precipitation to temperature variability or trends, especially in the tropics, which implies that the models may underestimate the projected increase in extreme precipitation in the future. Kendon et al. (2014) studied the intensification of extremes with climate change on a regional scale, over the United Kingdom using a model generally used for weather forecasting with a grid spacing of 1.5 km. Kendon et al. (2014) found that a warmer climate produced an increase in winter hourly rainfall intensities and an increase in high-intensity summer precipitation events indicative of flash flooding. To understand how future climate change might impact precipitation at various scales, it is imperative for us to accurately simulate and predict past and present precipitation.

Many studies (e.g., Stanfield et al. 2014, 2015, and 2016; Dolinar et al. 2015a&b) have shown that modeled clouds, radiation, and precipitation agree with observations within a certain range on a global scale, however, large biases occur at the regional scale.

For example, Dolinar et al. (2015b) compared five reanalyzed precipitation rates (PRs) with PRs from the Tropical Rainfall Measurement Mission (TRMM) and found that while the reanalyzed PRs overestimate the large-scale TRMM mean (3.0 mm/day) by only 0.1–0.6 mm/day, the reanalyses oversimulate PRs in both ascent and descent regimes with PR biases over the ascent regime being roughly an order of magnitude larger than those over the descent regime.

The intertropical convergence zone (ITCZ), a narrow east-west band of vigorous cumulonimbus convection and heavy precipitation (Holton et al. 1971), is located in the ascent regime. In addition to the traditional North Pacific ITCZ, a well-known secondary ITCZ is often found in the southern tropics of many GCMs when they are coupled with their respective ocean model, resulting in a "double-ITCZ" and excessive precipitation in zones south of the equator in the Atlantic and the Eastern Pacific (Lin 2007; Pincus et al. 2008). The double-ITCZ has been a long-standing problem within the GCMs. Hirota et al. (2011) examined precipitation in many CMIP3 models and found that models with low skills scores, as defined by Taylor et al. (2001), tended to have a stronger correlation with sea surface temperatures (SSTs), a weaker correlation with vertical motion ($\omega500$), and tended to overestimate (underestimate) precipitation over large-scale subsidence (ascending) regions when compared to models with higher skill scores. Other studies have also examined the interaction of the ITCZ and the equatorial Pacific cold tongue bias in the models (Misra et al. 2008, Li and Xie 2014, Li et al. 2015). In Stanfield et al. (2016), we focused precipitation in the traditional North Pacific ITCZ and will continue to focus on precipitation in this region in this study.

Importance and Purpose of the Study

GCMs are an essential tool for simulating possible future climate scenarios. However, as concluded by the IPCC AR5, the GCMs still have many uncertainties to contend with in regards to clouds, precipitation, and their associated feedbacks, and any improvements we can make in regards to the GCMs are vital to forecasting future climate changes.

Three studies have been published at the University of North Dakota since 2014. The first two studies in conjunction analyzed changes to cloud (Stanfield et al. 2014) and radiative properties (Stanfield et al. 2015) in the NASA GISS-E2-R Post-CMIP5 GCM, and compared new results with the frozen CMIP5 version of the GCM as well as various observations. Stanfield et al. (2016) compared precipitation coverage and magnitude from 29 GCM AMIP simulations with GPCP (Adler et al. 2003) and TRMM (Huffman and Bolvin, 2011) precipitation products over the North Pacific ITCZ, as well as comparing them with their linked CMIP5 historical ocean-coupled runs. A new algorithm has been developed to define the North Pacific ITCZ through several metrics with the intent of quantifying magnitude-, location-, and width-based biases within the GCMs. Recently, these studies have been updated by examining three versions of the NASA GISS ModelE GCM in comparison with a suite of space- and ground-based observations.

The goal of this study is to determine how recent parameterization changes to the NASA GISS ModelE GCM have impacted simulated IWC, LWC, and updraft strength, and to determine how changes in these variables have impacted simulated clouds and precipitation both globally and regionally, with a special focus on two regions of interest

within the ITCZ: the Eastern Pacific, and the Western Pacific. This study seeks to provide feedback to improve the NASA GISS ModelE GCM simulations.

Limitations of the Study

All GCM data acquired for this study have a monthly temporal output and have been provided for us either by a data center or by NASA GISS directly. Dynamic analysis is challenging without access to higher temporal resolutions, such as hourly or daily GCM runs. Without running the GCMs in house, analysis essentially left to a black box in which it can be seen how each field has evolved with time, however, multiple changes have been made between each time step. Determining how each modification to the GCM has specifically affected relevant variables is challenging given the complex interactions between simulated variables. Data availability was limited as two of the GCM simulations were provided by outside sources, meaning available variables and temporal resolution were not controllable factors. Examining CMIP6 GCM results was proposed originally, but unfortunately time was another limitation as CMIP6 GCM simulations were not available at the time of this study.

Outline

The dissertation is organized as follows. In Chapter II, relevant information on data used in this study will be provided, grouped based on the data source. Overarching methodologies used across multiple chapters are discussed in Chapter III. In detail, basic statistical methods, calculations of global and zonal means, and the reasoning for establishing two focus regions which are showcased in the regional analyses provided in

Chapter IV and VI updates are discussed. Chapters IV through VI contain more specific additions to the methodology employed when appropriate only for that section of the chapter.

Chapters IV through VI discuss the results of this study, split into three parts based on the topic discussed. Chapter IV discusses the findings of Stanfield et al. (2014) which analyzed multiple cloud properties in a newer NASA GISS-E2-R Post-CMIP5 version of the GCM and compared these results with the frozen CMIP5 version of the GCM as well as various observations. An update to Stanfield et al. (2014) is provided which discusses how recent changes in the E5 GCM simulation have impacted IWP, IWC, LWP, LWC, vertical motion, total column cloud fraction, cloud fraction profiles, and precipitable water vapor in the CMIP5, Post-CMIP5, and most recent E5 versions of the models.

- Stanfield RE, Dong X, Xi B, Kennedy A, Del Genio AD, Minnis P, Jiang JH (2014) Assessment of NASA GISS CMIP5 and post-CMIP5 simulated clouds and TOA radiation budgets using satellite observations: Part I: Cloud fraction and properties. J. Clim., 27 (11): 4189-4208, doi:10.1175/JCLI-D-13-00558.1.

Chapter V discusses the findings of Stanfield et al. (2015) which analyzed radiative properties in the NASA GISS-E2-R Post-CMIP5 GCM and compared new results with the frozen CMIP5 version of the GCM as well as various observations. Radiative properties are not available in the E5 version of the GCM at the time of this study, and as such an update to Stanfield et al. (2015) is provided which speculates on how observed changes in E5-simulated cloud properties might impact radiative fields in the new version of the GCM.

- Stanfield RE, Dong X, Xi B, Del Genio AD, Minnis P, Doelling D, Loeb N (2015) Assessment of NASA GISS CMIP5 and Post-CMIP5 simulated clouds and TOA radiation budgets using satellite observations. Part II: TOA radiation budget and CREs. J Clim 28 (5): 1842–1864. doi:10.1175/JCLI-D-14-00249.1

Chapter VI discusses the findings of Stanfield et al. (2016) which compared precipitation coverage and magnitudes from 29 GCM AMIP simulations with GPCP (Adler et al. 2003) and TRMM (Huffman and Bolvin, 2011) precipitation products over the North Pacific ITCZ, as well as with their linked CMIP5 historical ocean-coupled runs. More specifically, a new algorithm has been developed to define the North Pacific ITCZ through several metrics with the intent of quantifying magnitude-, location-, and width-based biases within the GCMs. An update to Stanfield et al. (2016) is provided which analyzes how recent changes in the E5 GCM simulation have impacted precipitation on global and regional scales.

- Stanfield RE, Jiang J, Dong X, Xi B, Su H, Donner L, Rotstayn L, Wu T, Cole J, and Shinodo E (2016) A Quantitative Assessment of Precipitation Associated with the ITCZ in the CMIP GCM Simulations. Climate Dynamics, 47: 1863. doi:10.1007/s00382-015-2937-y

A summary of updated conclusions, potential future work, and suggestions are provided in Chapter VII.

CHAPTER II

DATA

The NASA GISS ModelE Global Climate Model

This section will outline the general concept behind the suite of GCMs used in this study while providing specific details about the CMIP5 version of the NASA GISS Model E2 (GISS-E2) GCM, parameterization changes made in the post-CMIP5 (P5) iteration of the NASA GISS GCM, as well as new changes made to the P5 version of the model outlined in Elsaessor et al. (2017).

C5 GCM data are provided by the Earth System Grid Federation (ESGF) Program for Climate Model Diagnosis and Intercomparison (PCMDI) database from various modeling groups at various temporal resolutions. The spatial resolutions of the GCMs are varied and dependent on the modeling group. Each ensemble member within the ESGF PCMDI database is given three integers (N,M,L), in r<N>i<M>p<L> format to distinguish related simulations, where N is the realization number, M is the initialization method indicator, and L is the perturbed physics number as described in Taylor et al. (2010). In Stanfield et al. (2016), monthly data from each respective r1i1p1 GCM simulation during the period January 2000 - December 2005 were used. This period is used frequently in this study as it best represents the climate mean as there are no strong ENSO signals during this observational period. It should be noted, however, that the

models were not screened for their respective ENSO signal during this time period, and as such there may be bias introduced into our comparison because of this.

CMIP5 GISS ModelE GCM

While multiple simulations of each model are provided by the ESGF PCMDI CMIP5 database, Stanfield et al. (2014) used the r5i1p3 ensemble member of the GISS ModelE GCM, outlined in Taylor et al. (2012). The third version of model physics (p3) includes aerosol direct, semi-direct, and first indirect effects, although differences in mean fields between this model version and the version with non-interactive aerosols (p1) are small (Schmidt et al. 2014). The r1i1p1 ensemble member was used in Stanfield et al. (2016), and is used again in the updates provided in this study for consistency. The minimum relative humidity at which clouds are formed is tuned in order to reach global mean radiative balance within the GISS GCM. The GISS-E2 has a native horizontal resolution of $2° \times 2.5°$ (latitude $\times$ longitude) with 40 vertical layers. A detailed analysis of the C5 run can be found in Schmidt et al. (2014).

The GISS convective parameterization is a mass flux scheme triggered when a parcel lifted from one model layer becomes buoyant. The resulting mass flux restores cloud base to neutral buoyancy over a specified convective adjustment time. The mass flux is partitioned into two bulk "plumes" with different interactive entrainment rates, based on the parameterization of Gregory (2001). Vertical velocity is diagnosed and cloud top is defined as the level at which the vertical velocity becomes zero or negative (Del Genio et al. 2007). Condensed water in the updraft is assumed to follow a Marshall-Palmer distribution, and by comparing the updraft speed to fall speeds for different

9

particle sizes, the fractions of the condensate that precipitates, detrains, and advects upward are determined (Del Genio et al. 2005).

Post-CMIP5 GISS ModelE GCM

Two versions of NASA GISS ModelE Post-CMIP5 (P5) intermediate diagnostic data were provided by NASA GISS at different times for this study. Stanfield et al. (2014) and Stanfield et al. (2015) used four years of P5 diagnostic data provided directly by NASA GISS in 2013, while updates to these studies use only one year of a more recently released version of the P5 diagnostic data which was provided indirectly by NASA GISS through the Jet Propulsion Laboratory. Consistency of the minor changes between these two versions cannot be 100% guaranteed, however, the two major parameterization changes are confirmed to be consistent between each version. The cumulus parameterization has been modified with increased entrainment and rain evaporation and changes in the convective downdraft as detailed in Del Genio et al. (2012). For example, the stronger entrainment allows the new cumulus parameterization to produce MJO (Madden–Julian Oscillation)-like variability (Kim et al. 2012). Increased entrainment and rain evaporation decrease convective drying and thus can cause a small local increase in water vapor and cloudiness, especially in regions where convective depth is most sensitive to entrainment.

The boundary layer turbulence parameterization has been modified as well in the P5 simulation (Yao and Cheng 2012). According to Yao and Cheng (2012), this new scheme differs in its computation of nonlocal transports, turbulent length scale, and PBL height, and shows improvements in cloud and radiation simulations, particularly over the

subtropical eastern oceans and the southern oceans, despite the fact that the stratiform cloud parameterization itself is unchanged from the C5 version.

ModelE GCM with Elsaessor et al. (2017) Ice Modifications

Recently, an improved parameterization of convective cloud ice was developed by Elsaesser et al. (2017) which incorporates new particle size distributions for convective outflow and a new ice particle fall speed formulation. Elsaessor et al. (2017) modified convective outflow particle size distributions and ice particle fall speeds in the NASA GISS ModelE convective cloud ice parameterization using data gathered from four field campaigns: the NASA African Monsoon Multidisciplinary Analysis (NAMMA), NASA Tropical Composition, Cloud and Climate Coupling (TC4), DOE ARM-NASA Midlatitude Continental Convective Clouds Experiment (MC3E), and DOE ARM Small Particles in Cirrus (SPARTICUS). Going forward, the GISS team is actively preparing the CMIP6 configuration of the GISS model, which may include the modified parameterizations described in Elsaesser et al. (2017).

CERES-MODIS (CM)

This research utilized three data products provided by the NASA Clouds and Earth's Radiant Energy System (CERES) team: the SYN1 cloud products and the EBAF-TOA and EBAF-SFC radiation products.

CERES SYN1 Cloud Products

This study uses the CERES-MODIS SYNoptic radiative fluxes and clouds (SYN1) Edition 3 dataset for global and regional cloud fraction (CF), ice water path (IWP) and liquid water path (LWP) comparisons, which includes CERES Edition 2 cloud properties (Minnis et al. 2011a). Note that the CERES science team uses different algorithms to retrieve MODIS cloud properties than those used by the MODIS Atmospheres Science Team (MOD06) (Platnick et al. 2003) as discussed by Minnis et al. (2011b). More than 5 years of SYN1 data are used in this study (March 2000 to December 2005).

The CM Aqua and Terra CF retrievals have been extensively compared with other observational data in Minnis et al. (2008), which documented a 7% uncertainty in CM global CF retrievals. The global mean CM Edition 2 CF is among the lowest values from twelve different satellite retrievals that ranged from 0.56 to 0.73 (Stubenrauch et al. 2013). The mean CM low and high CFs, however, are close to the respective averages for the twelve datasets. Thus, other than having lower midlevel cloud fractions than all other retrievals, except for CALIPSO, the CM CFs are representative of passive satellite cloud amounts.

The SYN1 Edition 3 dataset has a well-known issue in its IWP and LWP estimations due to the relatively large uncertainties in regard to nighttime CWP retrievals when CWP > 50 g m^{-2}. Dong et al. (2008) documented uncertainties in the CM retrieved cloud LWP and found mean LWP differences of 11.3 ± 51.0 g m^{-2} compared to DOE Atmospheric Radiation Measurement Program ground-based microwave radiometer retrieved LWPs at the Southern Great Plains Central Facility. Minnis et al. (2011b) found

that the CM LWP over ocean was, on average, 0.2 ± 53.6 g m^{-2} less than LWP from matched overcast AMSR-E footprints. For single layer cirrus clouds, Mace et al. (2005) found that the CM IWP was 3.3 ± 16.2 g m^{-2} less than IWP derived from a ground-based radar. Although not quantified precisely, the CM IWP means for all ice clouds are similar in magnitude and distribution compared to IWP from CloudSat (Waliser et al. 2009). Minnis et al. (2007) found that for ice-over-water cloud systems, CWP from the single-phase retrieval (CWP = IWP) was 10-15% greater than when IWP and LWP were retrieved explicitly using microwave and visible-infrared imagers together. Thus, in these situations, the CM IWP (CWP) is probably overestimated by 10-15%. Further discussion of the CM cloud properties uncertainties is found in Minnis et al. (2011b).

CERES EBAF-TOA and EBAF-SFC Radiation Products

The CERES energy balanced and filled at the top of the atmosphere (EBAF-TOA) Ed2.7 dataset is used for needed radiation calculations in this study. The CERES EBAF-TOA product is derived using the CERES SYN1deg-lite product, adjusted within the uncertainty to be consistent with the net planetary imbalance derived from ocean heating rates from Argo in-situ ocean temperature measurements (Loeb et al. 2012). CERES TOA radiative fluxes have been validated across multiple studies (Loeb et al. 2006 and 2007; Kato and Loeb 2005; Doelling et al. 2013). For more detailed information regarding the derivation of CERES results, please consult the following sources: Loeb et al. (2001, 2003, 2005, 2012), Kopp and Lawrence (2005), and Minnis et al. (2011a). Based on documentation, CERES EBAF regional errors/uncertainties, meaning more specifically average error across any singular 1°x1° gridbox, are as follows: TOA clear-

sky OLR (3.6 W m^{-2}) and TOA clear-sky SW (2.6 W m^{-2}). TOA all-sky SW errors/uncertainties are ~ 5 W m^{-2} during the period of March 2000-June 2002 and ~4 W m^{-2} during the period of July 2002-December 2010. Monthly mean fluxes were determined by the CERES team through spatially averaging the instantaneous values on a 1°×1° grid, temporally interpolating between observed values at one hour increments for each hour of every month, and then averaging all hour boxes in a month (Young et al. 1998; Doelling et al. 2013). Level-3 processing is performed on a nested grid, which uses 1° equal-angle regions between 45°N and 45°S, maintaining area consistency at higher latitudes. The fluxes from the nested grid are then output to a complete 360x180 1°×1° grid using replication. In the CERES EBAF-TOA radiation product, clear-sky TOA fluxes are supplemented with fluxes derived from partly cloudy CERES footprints via narrow-to-broadband regression (Loeb et al. 2009).

Cloudsat / CALIPSO Cloud Products

The CALIPSO and Cloudsat satellites were launched in April 2006 as part of the A-Train constellation (Winker et al. 2007). CALIPSO carries the Cloud-Aerosol Lidar with Orthogonal Polarization (CALIOP) instrument, a nadir-viewing two-wavelength (1064 and 532 nm) polarization lidar. The CloudSat millimeter wavelength cloud profiling radar (CPR) has a unique ability to observe the majority of cloud condensate and precipitation within its nadir field of view. The CloudSat-retrieved properties have a vertical resolution of 500 m (Stephens et al. 2002). When combined with CALIPSO, they yield a nearly complete vertical cloud profile, the exception being hydrometeors in the

14

lower troposphere that may be masked due to attenuation or surface clutter (Marchand et al. 2008).

CCCM Cloud Products

The CALIOP and CPR retrievals from the CALIPSO-Cloudsat-CERES-MODIS (CCCM, Kato et al. 2010) RelB1 data product are used for total column CF comparisons. Given that CCCM CFs are based on active scanning strategies, we expect that CF results from CCCM will be generally higher than other CF observations based on passive scanning strategies.

2C-ICE Ice Cloud Products

The Cloudsat and CALIPSO Ice Cloud Property Product (2C-ICE) contains retrieved estimates of ice cloud water content (IWC) and effective radius (r_e) for identified ice clouds measured by Cloud Profiling Radar (CPR) on CloudSat and/or the CALIPSO Cloud-Aerosol Lidar with Orthogonal Polarization (CALIOP; hereafter referred as the Lidar). This 2C-ICE cloud product uses combined inputs of measured radar reflectivity factor from the CloudSat 2BGEOGPROF product and measured attenuated backscattering coefficients at 532 nm from CALISPO lidar to constrain the ice cloud retrieval more tightly than the radar-only product and to generate more accurate results.

AIRS Water Vapor Products

This study uses the Level 3 AIRS AIRX3STD dataset for observations of atmospheric precipitable water vapor (PWV; Olsen et al. 2007b). AIRS is one of the six instruments on board the Aqua satellite with a spatial resolution of 50 km reported on a 1° x 1° grid. PWV retrievals are more reliable from 1000 hPa to 300 hPa over ocean, and 850 hPa to 300 hPa over land, with an estimated uncertainty of 25% in the tropics, 30% within the midlatitudes, 50% at high latitudes, and 30% globally averaged (Jiang et al. 2012). Because AIRS cannot retrieve water vapor amounts in largely overcast scenes, which are usually more humid than clear scenes, it is dry-biased by 5-10% over much of the globe; the opposite is true in subtropical stratocumulus regions in which near-overcast scenes are overlain by very dry air (Fetzer et al. 2006).

AMSR-E Water Vapor Products

AMSR-E Level 3 Version 5 PWV data (Wentz 1997) are obtained from Remote Sensing Systems in their native gridded resolution of 0.25° x 0.25°. The product is estimated to have a random error up to ~1.2 kg m^{-2}. The AIRS and AMSR-E PWV data over the oceans have been extensively compared by the AIRS science team, described in Fetzer et al. (2006), who found a difference of no more than 5% when both instruments view the same scene. The AMSR-E PWV retrievals over oceans are higher than their AIRS counterparts simply because AMSR-E is capable of measuring PWV from the surface to TOA, while reliable AIRS retrievals are restricted from 1000 hPa to 300 hPa, and also because of the dry bias due to the omission of nearly overcast scenes described above. The AMSR-E retrievals are valid for the full column of the atmosphere, but are

limited to ocean-only retrievals, while the AIRS retrievals are provided over both land and ocean, but are restricted from 1000 hPa to 300 hPa. As such, AMSR-E will be more reliable for comparisons over the ocean, while AIRS should be considered over land.

GPCP Precipitation Product

The Global Precipitation Climatology Project (GPCP, Adler et al. 2003) is part of the Global Energy and Water Cycle Exchanges Project (GEWEX) established by the World Climate Research Programme (WCRP). The GPCP precipitation product used in this study, as used in Stanfield et al. (2016), is the GPCP satellite-gauge (SG) monthly precipitation product which provides monthly precipitation estimates on a global 2.5°×2.5° grid based on a combination of data from geostationary satellites, polar satellites, surface reference data, and station observations. Uncertainty of precipitation in the GPCP-SG product is estimated at ~15% (Huffman et al. 1997).

TRMM Precipitation Product

The Tropical Rainfall Measuring Mission (TRMM, Huffman and Bolvin 2011) precipitation product is generated through a combination of four sources: the TRMM precipitation radar data, passive microwave radiances at multiple frequencies and polarizations (observed from a mixed constellation of operational and research low-earth-orbit [LEO] satellites), thermal infrared brightness temperatures from geosynchronous satellites, and surface precipitation gauge measurements (Huffman et al. 2007; Huffman and Bolvin 2011). This study uses the 3B43 monthly TRMM dataset, as used in Stanfield et al. (2016), with a native resolution of 0.25° × 0.25° (latitude × longitude). The TRMM

microwave imager is available between ±37° of latitude. An important difference between the GPCP and TRMM products is the inclusion of the precipitation radar on-board the TRMM satellite. Given the higher spatial resolution and ability of the precipitation radar to detect precipitating clouds, we expect the precipitation features identified by TRMM to be finer/sharper than features identified by GPCP.

The uncertainties of 3-hourly TRMM precipitation data are estimated at 90% - 120% for light rain (< 0.25 mm/hr) and 20% - 40% for heavy rain (Habib and Krajewski 2002; AghaKouchak et al. 2009). TRMM data is known to have up to a ~30% positive bias during the northern summer when compared to other measurements (e.g. Nicholson et al. 2003), which cannot be removed through monthly averaging. It should be noted that at the time of these studies, generation of the GPCP product does not include TRMM observations (Huffman and Bolvin 2012).

MERRA-2 Reanalysis

A multi-level updraft analysis to examine changes in the strength of the updraft associated within the ascending branch of the Hadley Cell is performed in this study. Three-dimensional wind field observations are particularly challenging to come by, and as such we rely on "semi-observational" data from the MERRA-2 reanalysis to compare with the GCM runs. MERRA-2 has a native resolution of 0.67° × 0.5° (longitude × latitude), and uses a 3D-VAR assimilation method with incremental updates (Molod et al. 2015).

CHAPTER III

OVERARCHING METHODOLOGY

Methodologies used across multiple chapters are discussed in this section. In detail, basic statistical methods employed across every chapter in this study are described in section 3.1, calculations of global and zonal means are discussed in section 3.2, and the reasoning behind the establishment of two areas of focus which are showcased in regional analyses provided in the updates to Chapters IV and VI are discussed in section 3.3.

3.1 Statistical Methods

In order to properly assess the GISS GCM and its sensitivities, a few basic statistical methods are employed and presented in Table 1. Global averages are computed through the following two steps (temporal average first, and then spatial). First, the monthly averages (for example January) are binned and averaged from all monthly means (for all available Januaries) for a grid box, and then the seasonal and annual averages are calculated from the averages from January to December. Once the monthly, seasonal and annual averages over a grid box are created, a global mean is computed using a cosine weighting scheme, where the weight applied to each datum is the cosine of the latitude to which that datum belongs. After dividing by the sum of the weights, a global cosine weighted mean is achieved.

Table 1. Basic statistics used for calculating the weighted mean bias, standard deviation, and correlation between the GCM and observations.

Statistic	Equation
Mean	$\bar{x} = \frac{1}{N}\sum_{i=1}^{N} x_i$
Weighted Mean	$\bar{x} = \frac{\sum_{i=1}^{N} w_i x_i}{\sum_{i=1}^{N} w_i}$
Standard Deviation	$\sigma_N = \sqrt{\frac{1}{N-1}\sum_{i-1}^{N}(x_i - \bar{x})^2}$
Covariance	$Cov(X,Y) = \sum_{i=1}^{N} \frac{(X_i - \bar{X})(Y_i - \bar{Y})}{(N-1)}$
Correlation	$Corr(X,Y) = \frac{Cov(X,Y)}{\sigma_X \sigma_Y}$
Root-Moon-Square Deviation (RMSD)	$RMSD = \sqrt{\frac{\sum_{t=1}^{n}(x_{1,t} - x_{2,t})^2}{n}}$

3.2 Global and Zonal Means

Global averages are calculated using two different methods in this study, based on the global property being averaged. Specifically, global averages of albedo must be calculated in a manner that differs from other variables. For most variables, available data within each grid box for the specified variable are averaged into an array of 12 months (from January to December) by averaging like months, such as all Marches during the available timeframe. This particularly helps to account for missing data associated with the 2C-ICE dataset used in this study, namely in 2007 where 2C-ICE has intermittent

20

days of missing data as well as an entire missing month of data. After this, the values of each grid box for all 12 months are averaged to generate a yearly mean for the aforementioned grid box, generating a global grid of yearly means, as is shown in all annually averaged global plots. Zonal averages are generated from the gridded global means by averaging across latitudinal bands. A cosine-weighting scheme is employed to calculate total global averages, where each point is weighted by the cosine of the latitude. A global average is finally calculated by the ratio of the sum of the values to the sum of the weights.

As mentioned prior, the method for calculating the global mean albedo differs slightly from this procedure. Given that albedo is a ratio of reflected SW to downwelling SW, the previously listed method leads to erroneous global averages. Instead, global averages of albedo are calculated using the ratio of the sum of the weighted reflected SW to the sum of the weighted downwelling SW. That is, values of reflected SW and downwelling SW are weighted using the cosine-weighting scheme mentioned prior, summed up respectively across the globe, divided by the sum of the weights, and then the global mean albedo is calculated as the weighted sum of reflected SW over the weighted sum of downwelling SW.

3.3 Defining Areas of Focus

Based on the most recent changes made to the E5 version of the NASA GISS GCM, two regions are showcased in regional analyses provided in the updates to Chapters IV and VI. These two regions are shown in Figure 1 and are labeled as follows: (1) the Eastern Pacific Northern ITCZ (EP-ITCZ), and (2) Indonesia and the Western

Pacific (INDO-WP). Boundaries of these regions are outlined in Table 2. These regions are selected based on their opposite behavior in regard to how many of the variables change with the most recent changes made in the NASA GISS E5 GCM simulation. Boundaries for these two regions were tested and selected based on maximizing coverage area where large inter-model differences were found while trying to minimize outside influences.
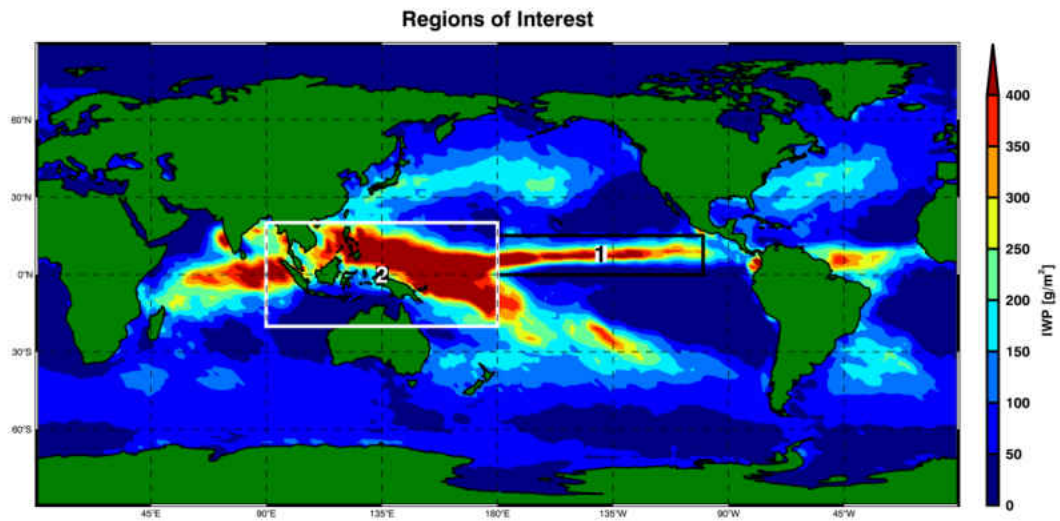
Figure 1. Two regions are showcased in regional analyses provided in the updates to Chapters IV and VI: (1) the Eastern Pacific Northern ITCZ (EP-ITCZ), and (2) Indonesia and the Western Pacific (INDO-WP).

Table 2. The longitudinal and latitudinal boundaries of the two regions of interest selected for this study.

Region	Region Label	Longitudinal Boundaries		Latitudinal Boundaries	
EP-ITCZ	1	180°	260° E	0°	15° N
INDO-WP	2	90°	180° E	20° S	20° N

CHAPTER IV

CLOUD PROPERTIES

This chapter details the analysis of cloud properties discussed in Stanfield et al. (2014), and examines how new modifications in the NASA GISS ModelE GCM have impacted model simulated cloud properties.

4.1 Stanfield et al. (2014) – NASA GISS CMIP5 vs Post-CMIP5 Cloud Analysis

Stanfield et al. (2014) focused on understanding the connections between cloud properties and their environmental conditions. Although globally averaged cloud fraction (CF) simulated by the CMIP5 version of the GCM is closer to that from satellite observations (Schmidt et al. 2013) relative to its CMIP3 predecessor (Schmidt et al. 2006; Kennedy et al. 2010; Naud et al. 2010), the GISS E2 GCM, like most other CMIP5 GCMs, underestimates marine boundary layer (MBL) clouds over the subtropical marine stratocumulus regions and the southern mid-latitude (SML) oceans (Stanfield 2012; Dolinar et al. 2014). Recent GISS-E2 runs, denoted as Post-CMIP5, have newly updated turbulence (Yao and Cheng 2012) and moist convection (Del Genio et al. 2012) parameterizations that have yielded substantial improvements over the SMLs and moderate improvement in coastal areas where MBL clouds frequently occur. Stanfield et al. (2014) looked at comparisons of CFs and cloud properties simulated by GISS-E2 CMIP5 and post-CMIP5 versions and NASA satellite observations. In detail, CMIP5 and post-CMIP5 simulated CFs and cloud water path (CWP) were compared with CERES-MODIS (MODerate resolution Imaging Spectroradiometer) Edition 2 cloud results (Minnis et al. 2011a) and CALIPSO (Cloud-Aerosol Lidar and Infrared Pathfinder

Satellite Observation) profiles (Kato et al. 2010). Model-simulated liquid and ice water paths (LWP, IWP) were compared with CloudSat results (Austin et al. 2009). Simulated precipitable water vapor (PWV) is compared to Advanced Microwave Scanning Radiometer (AMSR-E) retrievals (Wentz 1997), while both PWV and relative humidity (RH) profiles are compared with Atmospheric InfraRed Sounder (AIRS) retrievals (Olsen et al. 2007a&b).

4.1.1 Methodology

Cloud fraction height classifications as well as the term "bias" used in Stanfield et al. (2014) are discussed in the following.

4.1.1.1 Cloud Height Classifications and Total Column Cloud Fraction Calculations

P5-simulated CFs are stratified into high (P < 440 hPa), middle (440 hPa < P < 680 hPa), and low (P > 680 hPa) level cloud fractions based on the ISCCP classifications presented in Rossow and Schiffer (1999). Combinations of CFs within similar layer classifications were performed in-house by NASA GISS for both the P5 and C5 simulations, ensuring a proper vertical CF comparison.

4.1.1.2 The Term "Bias" in Stanfield et al. (2014)

Errors in satellite retrieved results are not explicitly accounted for in the figures shown in this comparison. While satellite retrievals contain uncertainties and biases, they remain good tools for diagnosing model issues. For example, NASA CERES-MODIS retrieved cloud properties have been extensively validated using a suite of ground-based

observations and retrievals (Dong et al. 2008 and 2016; Minnis et al. 2011b; Xi et al. 2010, 2014). On the other hand, cloud fields retrieved from different satellite observations or using different retrieval techniques give markedly different results (Stubenrauch et al. 2013). Given this caveat about satellite retrievals and uncertainties, the term "bias" used in the findings of Stanfield et al. (2014 and 2015) was used in its simplest form, and represents the differences between the model simulations and the observations.

4.1.2 Cloud Fraction

Figures 2a-d show observed and modeled gridded annual CFs for CERES-MODIS (CM), Cloudsat/CALIPSO (CC), P5, and C5 results, respectively, while Figs. 2e-h show the differences between simulated and observed CFs, such as P5-CM, C5-CM, P5-CC, and C5-CC, respectively. Comparing two observational datasets, the annual global average of CC derived CF is ~12% higher than CM, with much higher values over the Arctic regions. This discrepancy is a result of different sensitivities to clouds between passive and active remote sensing; CC is more sensitive to optically thin clouds and clouds with small coverage areas while CM has a tendency to miss small cumulus clouds and clouds with optical thicknesses less than 0.3 (Chiriaco et al. 2007; Minnis et al. 2008). The CF differences between CM and CC can be reduced to within ~2% if CC-derived CFs (~63%) are limited to clouds with optical depth greater than 0.3 (not shown in this study).
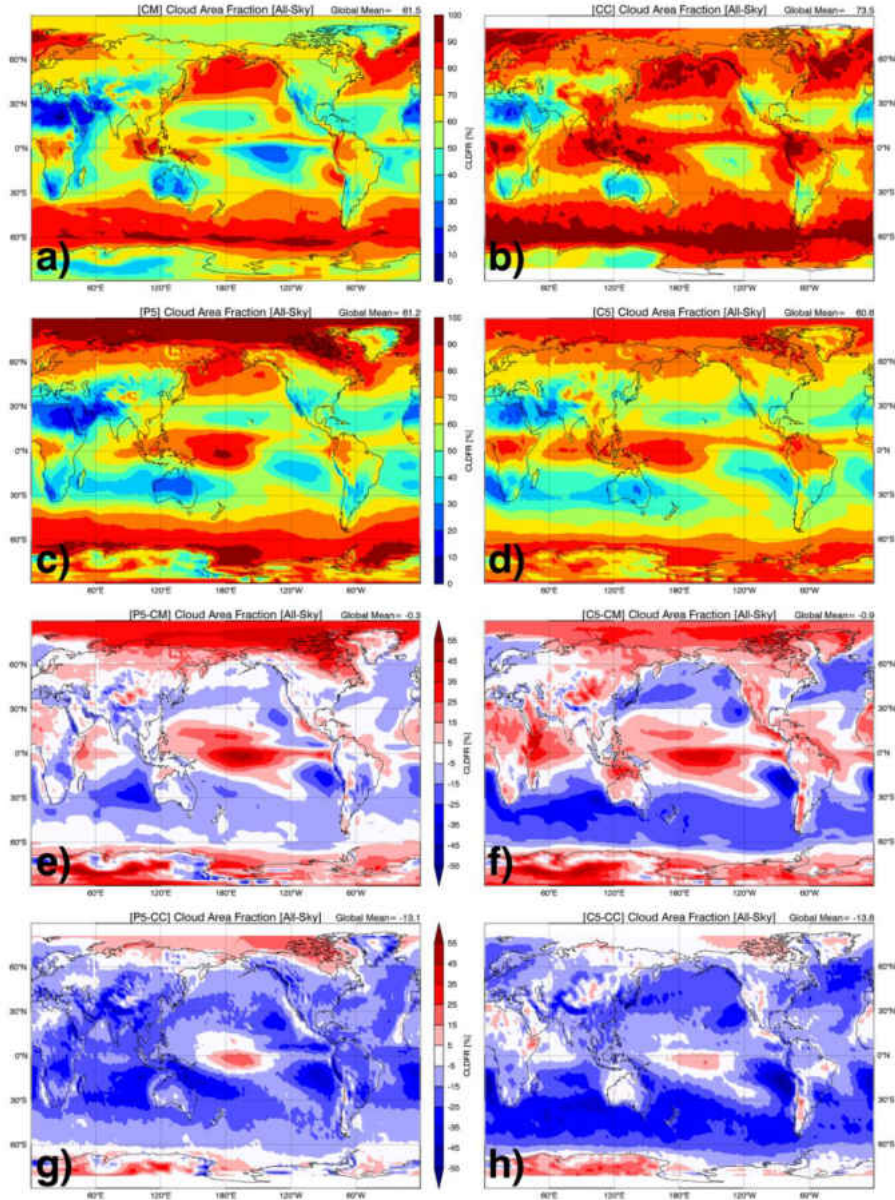
Figure 2. Gridded annual mean CFs derived from (a) NASA CM results, (b) NASA CC observations, and simulated by NASA GISS (c) P5 and (d) C5 GCM simulations, as well as their differences (e) P5-CM, (f) C5-CM, (g) P5-CC and (h) C5-CC, for the period of March 2000.

Although the global averages P5 and C5 simulated CFs agree within 1%, significant differences are evident over some regions, such as the Arctic and SMLs (Figs. 2c and 2d). The P5- and C5-simulated global distributions and mean CFs agree much

better with CM than with CC, suggesting that the GISS GCMs cannot simulate some of the optically thin clouds ($\tau < 0.3$) observed by CC. The C5-simulated CFs are greater than the CM derived CFs over the tropical and polar regions, but lower over the mid-latitudes (Figs. 2a and 2d). The newly simulated CFs from P5, agree much better with the CM CFs, especially over the mid-latitudes, but without significant improvement over the tropical Pacific Ocean (Figs. 2a and 2c). Arctic comparisons are not strongly considered at the time of this study given the known low biases associated with Arctic CM observations (Chiriaco et al. 2007; Minnis et al. 2008), as well as latitudinal limitations of CC observations (Winker 2007). Marine boundary layer (MBL) clouds are dominant over the SML regions as illustrated in Fig. 3d. While large improvements were observed in MBL CFs over the SMLs in Fig. 2, the P5-simulated CFs over regions with a high occurrence of subtropical MBL clouds, such as off the coasts of Peru and California, have only increased moderately.

Figure 3 shows zonally averaged total and low/middle/high CFs derived from observations and simulations. As expected, CC-derived total CFs are higher than the CM and model-simulated CFs over both the tropics and mid-latitudes (60°S-60°N), and agree well with model simulations over the polar regions (60°-90°), while the CM-derived total CFs are ~20% lower than the other three datasets over the polar regions (Fig. 3a). Over the SMLs, the P5-simulated total column CFs agree with CM and CC observations better than the previous C5 results due to the implementation of the new PBL scheme in P5. The changes to the PBL scheme deepen the boundary layer in the extratropics (Yao and Cheng 2012) and result in an increase of low-level CFs (Fig. 3d). Over the tropics, the P5-simulated total column CFs are slightly lower than the previous C5 results, primarily

due to the shallower tropical boundary layer in P5 relative to C5 in tropical regions outside the marine stratocumulus decks. For both high and mid-level CF comparisons, P5, C5, CC, and CM all agree well each other, with the exception of the CM-derived CFs, which are lower than the others, particularly over the Arctic regions (Figs. 3b and 3c).
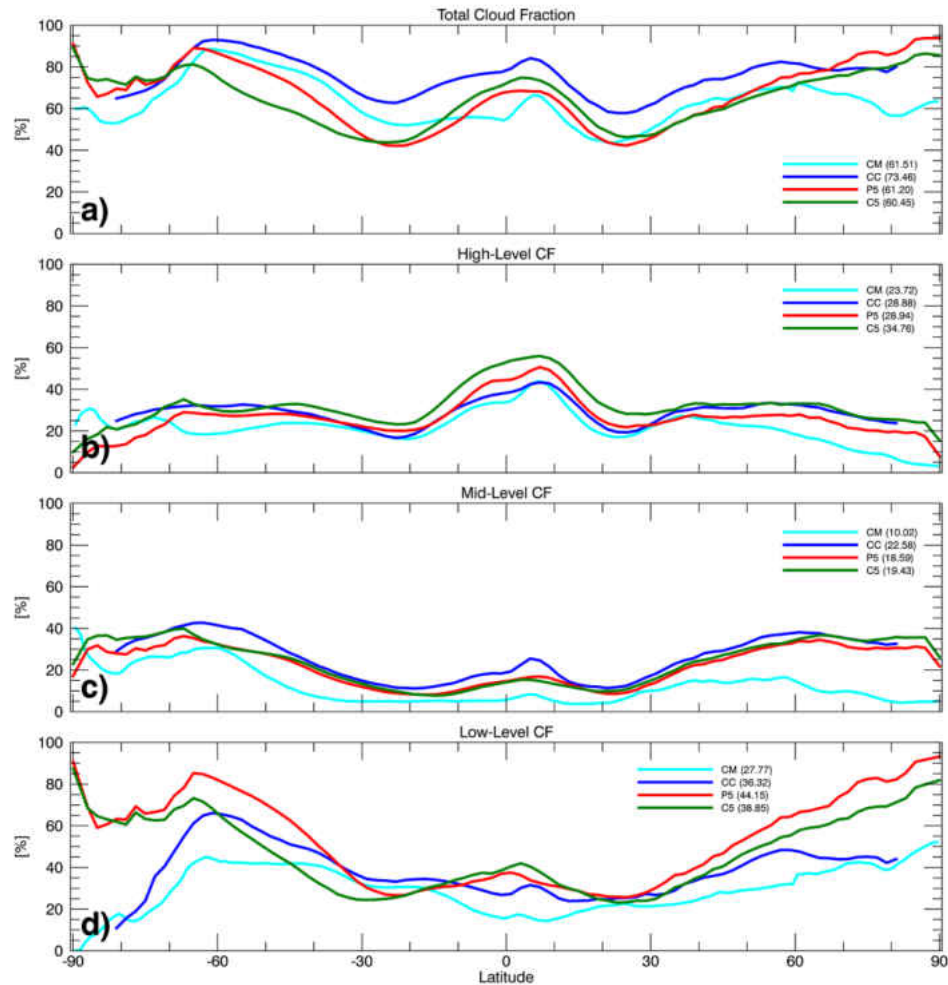
Figure 3. Zonally averaged (a) total CF, (b) high-level (P<440 hPa), (c) middle (440<P<680 hPa), and low (P>680 hPa) CFs from NASA CM and CC observations and NASA GISS P5 and C5 simulations. Values in parenthesis indicate corresponding global means.

4.1.3 Water Path (CWP, LWP, IWP)

Figure 4 describes observed and simulated CWPs while Fig. 5 breaks down CWP by phase and relates these properties to total column CF. The CloudSat (CS) and daytime CM retrieved global CWP distributions and their annual means are similar to each other with some exceptions. For example, the CS-derived CWPs over the tropics are almost doubled those retrieved from CM. Over marine stratus regions, however, the CM values are ~50 g m^{-2} more than the CS values due to the limitation of CS for detecting clouds below 1 km. These discrepancies result in ~16 g m^{-2} more globally averaged CWP retrieved from CS than from CM. Although the overall global CWP distributions from both P5 and C5 are fairly similar to CM and CS, their global mean CWPs are much higher than both CM and CS, primarily due to the over-simulation of CWPs over the tropics. However, the P5-simulated CWPs over the tropics are in general lower than the previous C5 results, bringing results from the new version of the model closer to observations (Fig. 5b). Regionally, large variation is found in magnitude based on surface type and in regions of ascent, such as the ITCZ. This improvement directly reflects the shallower tropical boundary layer in P5. Over the tropics, the decrease in CWP from the C5 to the P5 version is consistent with the decrease observed in total column CF, whereas comparing CWP and total column CF over the SMLs shows the opposite relationship. For example, the MBL CFs simulated by the P5 version of the GCM are about 20% higher than the C5 results, while the P5-simulated CWPs are 25 g m^{-2} less than the C5 results. This small change may be an artifact; The CWP diagnostic in the GCM is for stratiform clouds only. P5 has more frequent shallow convection than C5 in the SMLs

29

(Fig. 7 of Yao and Cheng 2012), causing an apparent decrease since its cloud water is not accounted for in CWP.

To understand the partitioning between ice and water, cloud LWP and IWP comparisons are shown in Figs. 5c and 5d, respectively. Note that the CM results are not shown because portions of the SYN1 LWP are hidden under ice and deep convection clouds, deeming the separation of water path into LWP and IWP unreliable. The P5-simulated LWPs are consistently much lower than those simulated from C5 by roughly 25-50 g m^{-2}, and are close to the CS retrievals, particularly over the SML region. Figure 5d shows that both the P5- and C5-simulated IWPs are roughly 100 - 200 g m^{-2} higher than the CS results over the tropical regions, with a peak at ~5 °N that is several degrees offset from the CS maximum.
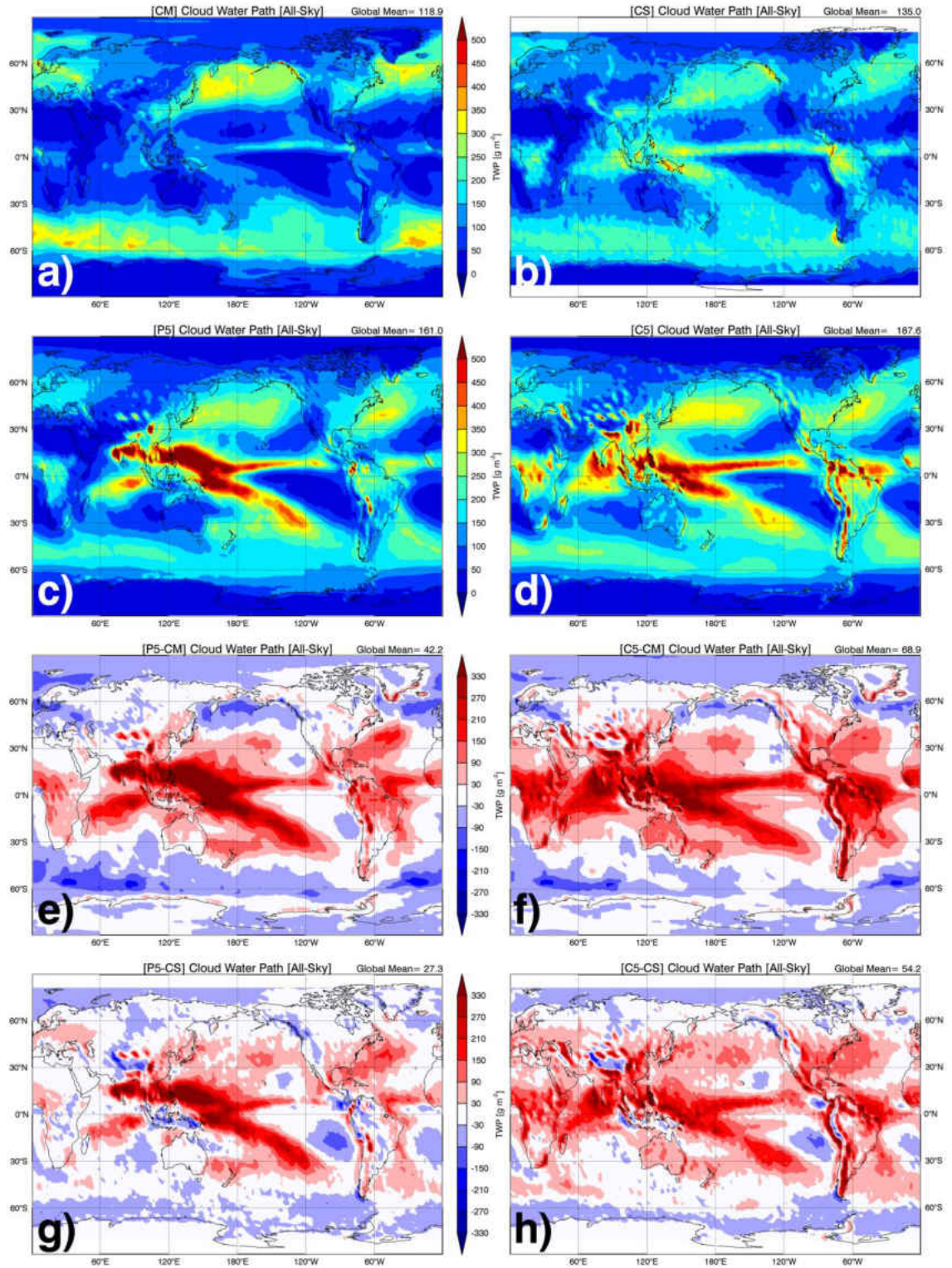
Figure 4. As in Fig. 2, except for CWP.
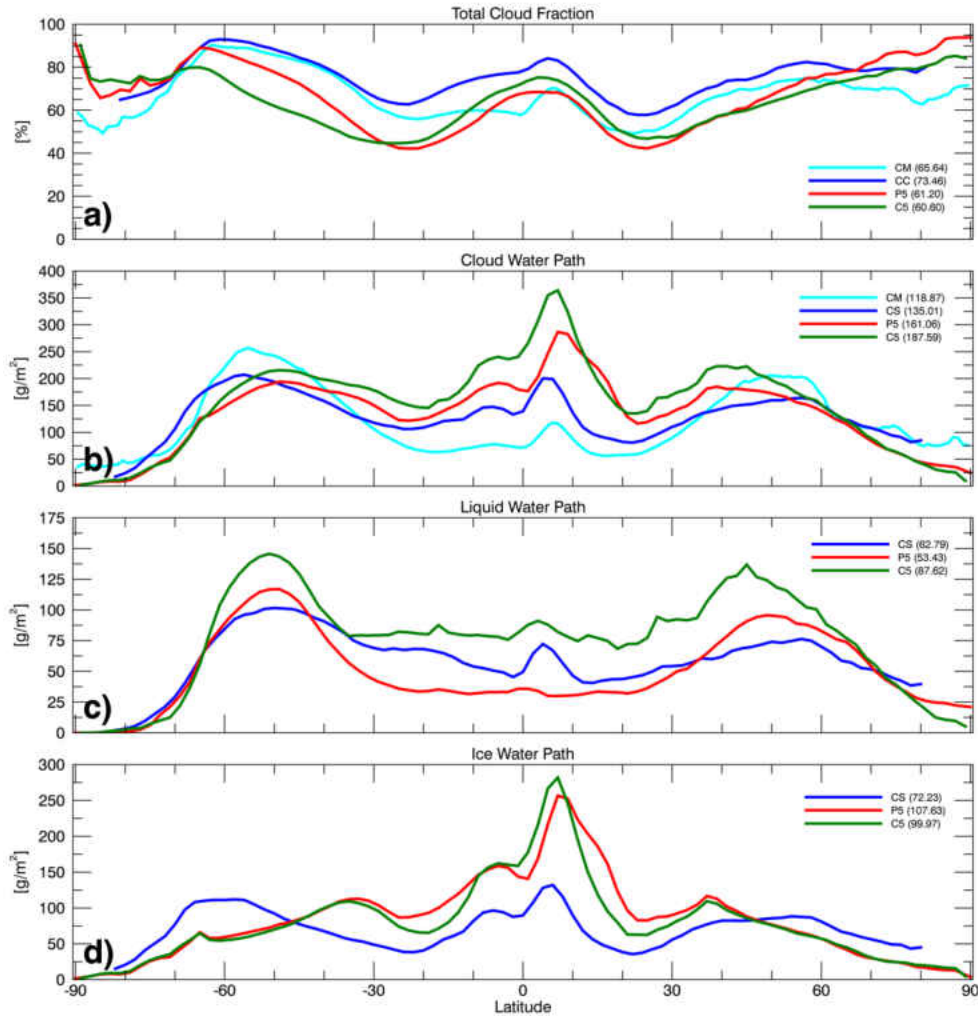
Figure 5. Zonally averaged (a) total CF (daytime only for CM), (b) CWP (daytime only for CM), (c) LWP, and (d) IWP. Values in parenthesis indicate corresponding global means.

4.1.4 Precipitable Water Vapor (PWV) and Relative Humidity (RH)

Figure 6 shows observed and simulated PWV means from AIRS, AMSR-E, P5, and C5, respectively, and the differences between simulated and observed PWV values. The AMSR-E PWV retrievals are slightly higher than the AIRS retrievals over the Indonesia-Papua New Guinea area. Given the limitations of each instrument, this is expected considering AIRS retrieves PWV between 1000 hPa to 300 hPa over ocean, and

850 hPa to 300 hPa over land, but only in scenes with significant clear sky, while AMSR-E is able to perform PWV retrievals from the surface to TOA in virtually all cloud conditions. Of the two, the AMSR-E PWV retrievals are more reliable than AIRS data over the ocean.

The global P5- and C5-simulated PWV patterns match well with the observed patterns, with the maximum occurring in the tropics along the ITCZ. As demonstrated in Figs. 6 and 7, P5-simulated PWV values are higher than both C5 and AIRS results by as much as 11 g m^{-2} over the tropical regions, due to stronger convective rain evaporation occurring in the P5 version of the model (Del Genio et al. 2012). Although the overall C5 global PWV pattern and mean matches well with the AIRS observations (Figs. 6a and 6d), the C5 PWV values less than the AIRS values by as much as 9 g m^{-2} over land (Fig. 6f). These discrepancies have been reduced significantly in the P5 simulations (Fig. 6e). Given that AIRS contains a dry bias resulting from AIRS being unable to perform retrievals during overcast conditions, along with instrument limitations discussed above, the P5 simulations make more physical sense than the C5 results over land. Over the ocean, the C5 simulated PWV values have negative biases of 1 to 5 g m^{-2} globally except for within a small region over the tropical Pacific Ocean, while P5 results agree better with AMSR-E retrievals globally, excluding over the tropical Pacific Ocean. Over the SMLs, the P5 PWV results more closely resemble AMSR-E observations than C5 results, which provides strong support for P5 simulating more MBL clouds than C5 (Figs. 2c and 3d) given the same SST and cloud microphysical schemes in both P5 and C5.
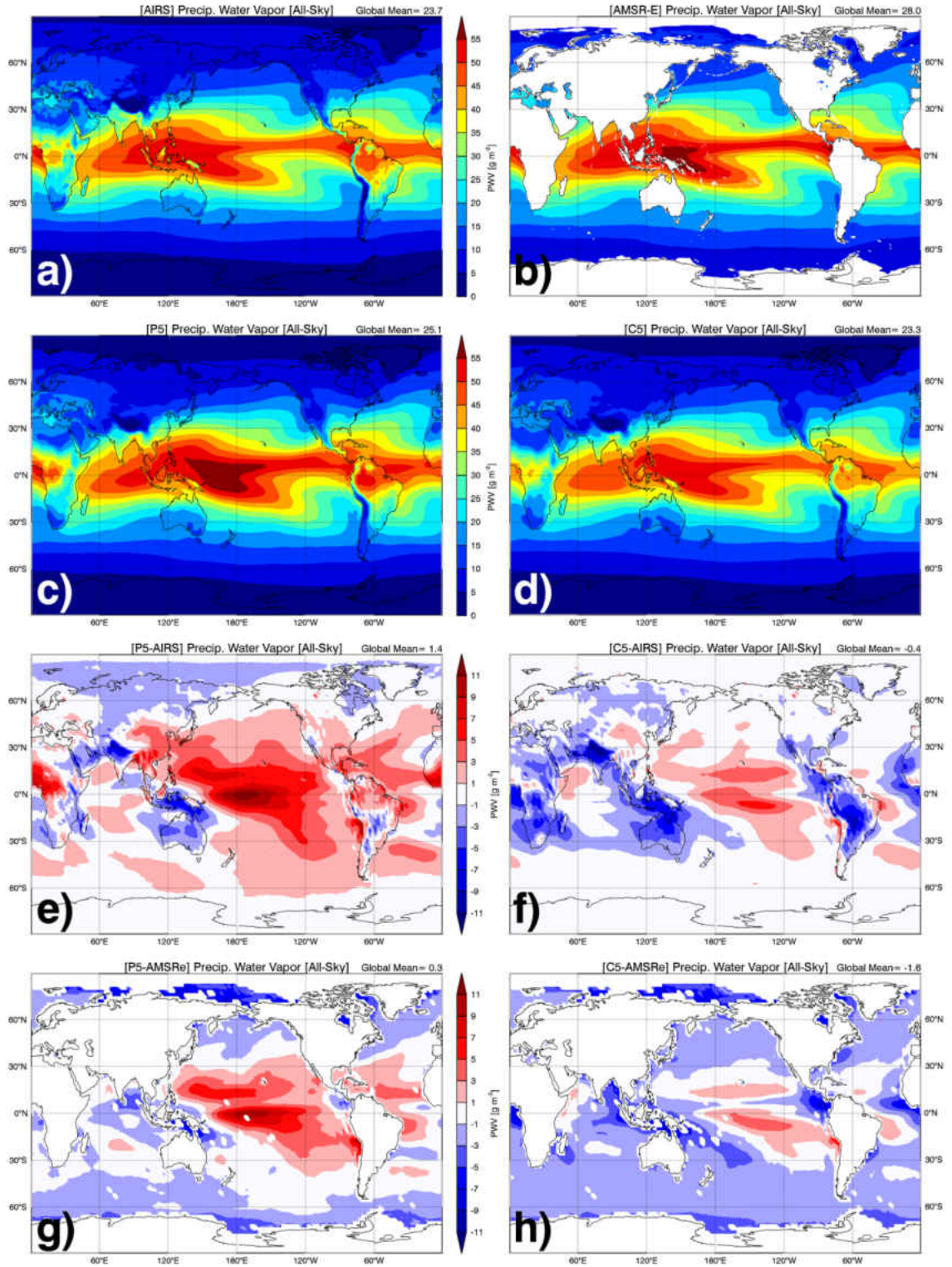
Figure 6. As in Fig. 2, except for PWV derived from AIRS and AMSE-R observations, as well as simulated by NASA GISS P5 and C5.

Zonally averaged PWVs and sea surface temperatures (SSTs) are presented in Fig. 7. It worth noting that surface air temperature over water was used as an estimate for AIRS SST, due to the noise found in its surface skin temperature retrievals. As illustrated in Fig. 7a, P5-simulated PWV values are higher than AIRS retrievals, while the C5 results closely match AIRS retrievals. Differences between P5 and AIRS increase in intensity approaching the equator from the mid-latitudes, on the order of 3 g m^{-2}. This makes physical sense given the dry bias associated with AIRS retrievals. By limiting zonally averaged PWV values to those only over the ocean (Fig. 7b), the comparison shows a close correlation between P5 simulations and AMSR-E retrievals, maintained within 2 g m^{-2}. Figure 7c indicates that the prescribed SSTs used in C5 and P5 simulations are consistent with AMSR-E observations. The model-prescribed SSTs are fairly consistent with those from AIRS, given that surface air temperature over water was used as an estimate of SST. The P5-simulated PWV values over the ocean are close to both the AMSR-E and AIRS results, but higher than the C5 simulations.

For the sake of brevity, extended discussions on RH results are not discussed here. Our general conclusions on RH are as follows. The P5-simulated RHs are greater than the C5 means. For regional comparisons, both the P5 and C5 low-level RH patterns are wetter than the AIRS retrievals over the tropics, slightly more for the P5 simulations compared to C5 results. Over the SML, the P5 and C5 low-level RHs are ~10% higher and lower than the AIRS retrievals, respectively. This finding is consistent with the CF comparison and provides strong support for the increase in the number of low-level clouds simulated by P5 over the SMLs. Over the polar regions, the GCM simulations are drier than the AIRS retrievals.

35
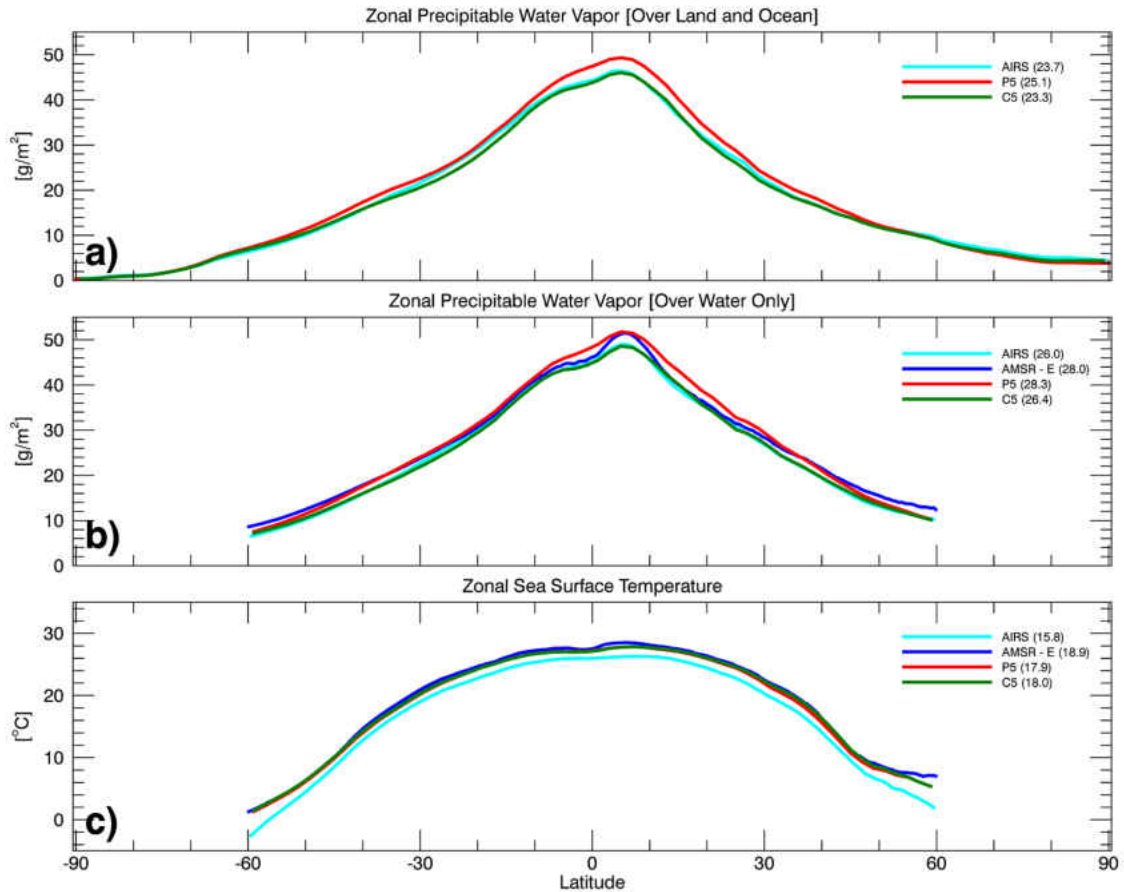
Figure 7. Latitudinally averaged PWV over (a) both land and ocean and (b) over ocean only, and SST. Note that AMSR-E has results only over ocean. Values in parenthesis indicate corresponding global mean.

4.1.5 Quantitative Estimation of Improvement in CFs and Cloud Properties over the SMLs

To quantitatively estimate the improvements in modeled CFs, scatterplots between CM/CC observed and P5/C5 simulated CFs globally and over the SMLs are shown in Fig. 8. Within these scatterplots, each point/dot represents the annual average at a grid point within the region of interest, be it globally or restricted to the SMLs. Global comparisons of P5/C5 simulations to CM (Fig. 8a) and CC (Fig. 8b) both show an improvement in the P5-simulated total column CF. Root mean square error (RMSE)

values have decreased slightly, while linear regressions of the data more closely resemble a one-to-one relationship with the observations. Within the SML focus region, parameterization changes in the P5 model, particularly changes to the boundary layer turbulence parameterization, have roughly halved RMSE values between the model runs when compared with both CM (Fig. 8c) and CC observed total column CFs (Fig. 8d).
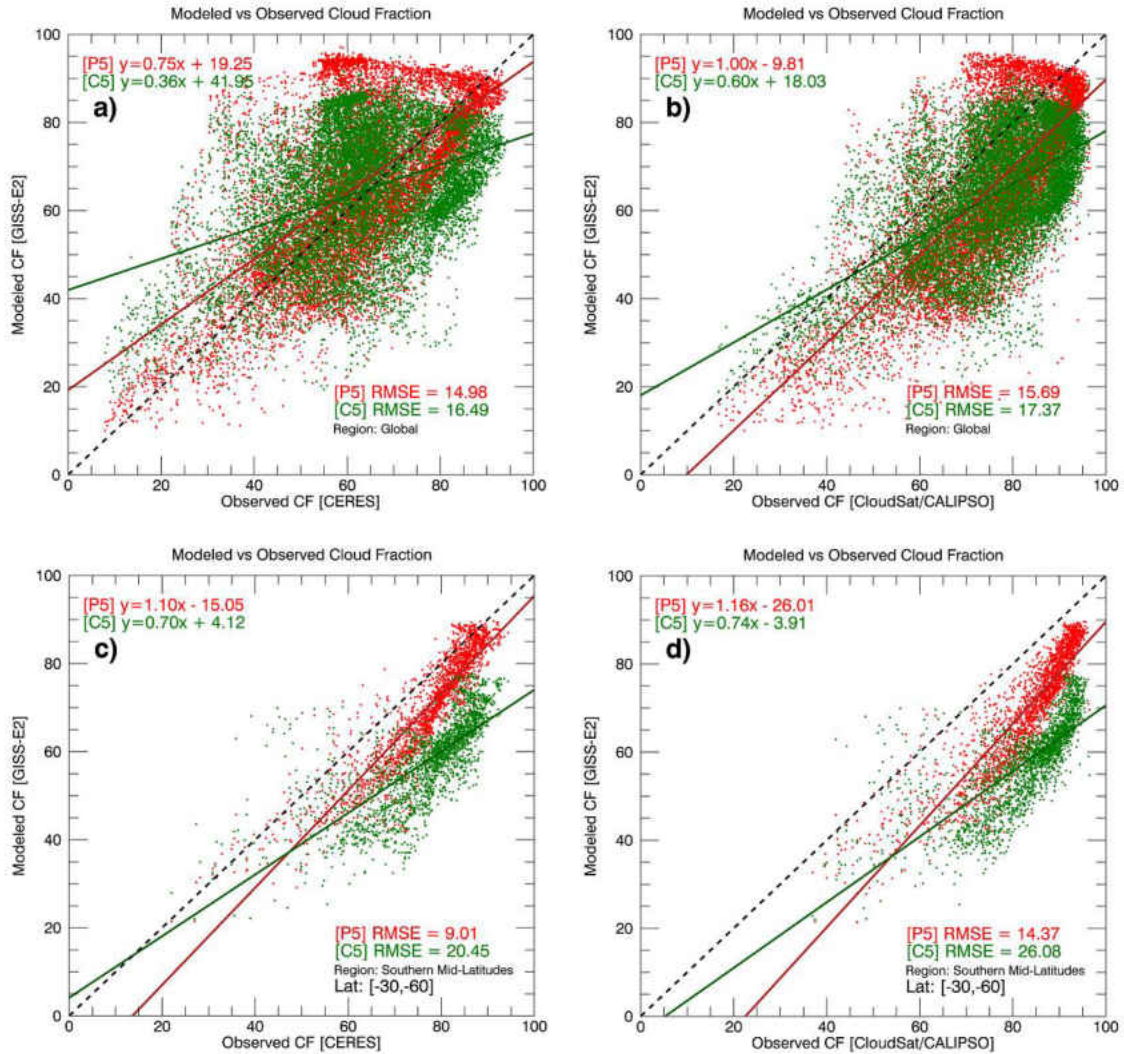
Figure 8. Scatterplots and associated linear regressions and RMSE of simulated and observed total column cloud fraction both globally (a,b) and restricted within the SMLs (c,d); comparing the models with CERES (left column) and CloudSat/CALPISO (right column) observations, respectively.

4.2 Update to Stanfield et al. (2014)

Studies have shown that high magnitudes of upper-level ice water content have been an ongoing concern in the NASA GISS ModelE GCM. Recently, Elsaessor et al. (2017) modified convective outflow particle size distributions (PSDs) and ice particle fall speeds in the NASA GISS ModelE convective cloud ice parameterization using data gathered from four field campaigns: the NASA African Monsoon Multidisciplinary Analysis (NAMMA), NASA Tropical Composition, Cloud and Climate Coupling (TC4), DOE ARM-NASA Midlatitude Continental Convective Clouds Experiment (MC3E), and DOE ARM Small Particles in Cirrus (SPARTICUS). With these new modifications to the NASA GISS ModelE GCM, the opportunity has arisen to analyze three different versions of the GISS GCM (the frozen CMIP5 version [C5], a post-CMIP5 version with modifications to cumulus and boundary layer turbulence parameterizations [P5], and the most recent version of the GCM which builds on the post-CMIP5 version with further modifications to the convective cloud ice parameterization [E5]).

This section will examine how each set of modifications has impacted the different versions of the GISS GCM and will compare these models with available 2C-ICE ice cloud properties retrieved from CC and to CM SYN1 cloud properties. Liquid water cloud comparisons were performed, but have been omitted for brevity as they were found to closely match the ice water analysis.

4.2.1 Methodology

This section details the methods used to convert heights provided in 2C-ICE and 2B-CWC-RVOD observations into pressure, and the methods employed to convert model given mass fractions into mass amounts.

4.2.1.1 2C-ICE Height to Pressure Conversions

2C-ICE vertical satellite products are provided on set height scales while model results are based on set pressures. This study uses CCCM observations to convert the heights given in the 2C-ICE vertical satellite product, as the CCCM product measurements are on set height intervals but provide corresponding pressures to said heights. Unfortunately, the height scales used in the CCCM product do not match directly with the height scales used in 2C-ICE. As such, unweighted linear interpolation is preformed to estimate the pressure at which 2C-ICE and 2B-CWC-RVOD measurements are valid. Given the logarithmic scaling nature of the atmosphere, using unweighted linear interpolation will knowingly introduce bias, however, this introduced bias is minimal and estimated to be less than 25 hPa in converted pressure.

4.2.1.2 Mass Fraction Conversions

Ice and liquid water contents in the NASA GISS GCM are provided as mass fractions while satellite products provide these variables as measurements of mass. In order to convert these mass fractions into mass, we perform a conversion at the monthly level by multiplying mass fractions by the local air density in kg m^{-3} and a conversion

factor of 10^6 mg kg^{-1}. For this calculation, air density is calculated using the ideal gas equation of state in Equation 1,

$$pressure = (\rho_{air}) * (R_{specfic}) * (T_a), \qquad (1)$$

where ρ_{air} is the density of air in Pascals, R$_{specific}$ is 287.058 J/T/Kg, and T$_a$ is the temperature of air in degrees Kelvin.

4.2.2 Ice Water Path (IWP) / Ice Water Content (IWC)

In order to best examine the evolution of the NASA GISS GCM and to analyze and evaluate the different versions of GCM simulations against available satellite observations, it is prudent to begin with examining how recent changes to convective outflow PSDs and ice particle fall speeds have impacted the amount of ice in the atmosphere. To reach this goal, we first examine the overall amount of ice in the atmosphere by way of ice water path, the vertical integration of available ice water content (IWC), and then examine IWCs across multiple levels to investigate at what levels these IWC changes occur.

4.2.2.1 Ice Water Path (IWP)

Average annual IWPs are shown in Fig. 9, given in units of grams per square meter, for NASA CERES SYN1 passive satellite observations, 2C-ICE active satellite observations, and for the C5, P5, and E5 versions of the GCM. Zonal averages of annual IWP are provided in Fig. 10 to further aid IWP discussions. Global means, standard deviations, and correlations and root-mean-square deviations of the GCM simulations in comparison with 2C-ICE observations are provided in Table 3.

40

Annual Ice Water Path
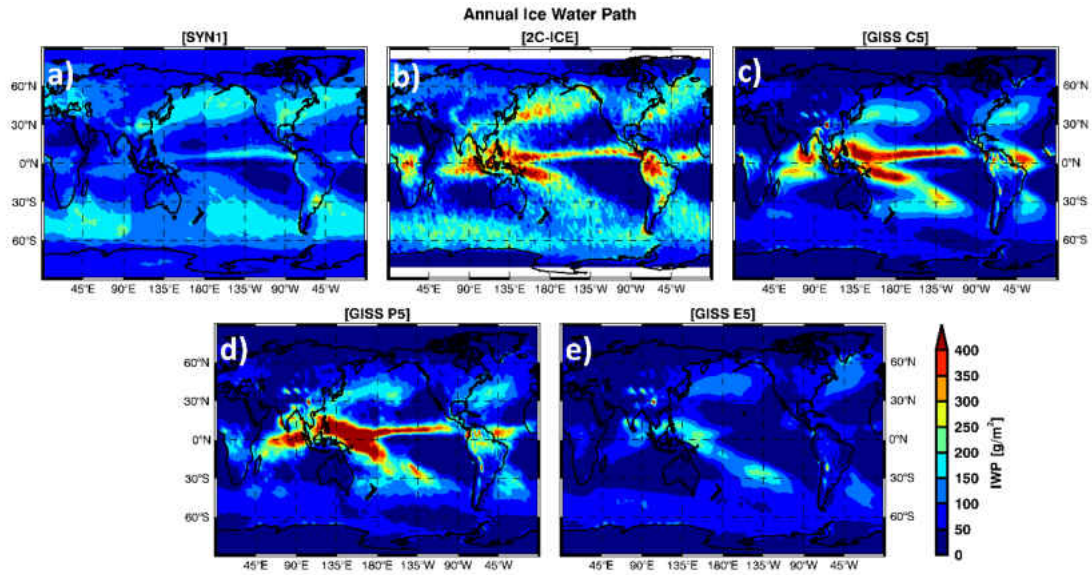
Figure 9. Annually averaged IWPs, given in units of grams per square meter, retrieved from (a) SYN1 and (b) 2C-ICE and simulated by the (c) C5, (d) P5, and (e) E5 versions of the NASA GISS GCM.
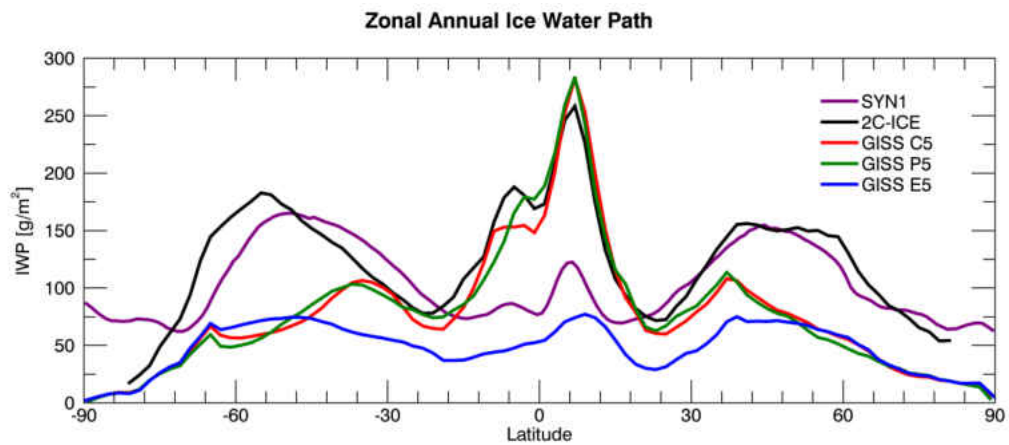
Figure 10. Zonally averaged IWPs, given in units of grams per square meter, for (purple) SYN1 passive satellite observations, (black) 2C-ICE active satellite observations, and for the (red) C5, (green) P5, and (blue) E5 versions of the NASA GISS GCM.

Table 3. Annual IWP weighted means, standard deviations, and correlation and root-mean-square deviation (RMSE) in relation to 2C-ICE satellite observations on a global scale.

Dataset	Global Mean [g m^{-2}]	Std. Dev. [g m^{-2}]	Corr. [2C-ICE]	RMSD [2C-ICE]
SYN1	107.7	42.8	-	-
2C-ICE	132.4	86.0	-	-
GISS C5	98.1	85.8	0.65	82.8
GISS P5	99.5	91.5	0.66	83.6
GISS E5	54.0	39.9	0.66	98.2

As shown in Figs. 9 and 10, SYN1 passively and 2C-ICE actively retrieved IWPs agree moderately well in the mid-latitudes and in the Arctic, however, large discrepancies arise in the tropics where SYN1 IWPs are less than half as much as 2C-ICE IWPs. Unfortunately, the SYN1 data used in this study includes the retrievals during both day and night and has well-known biases in retrieving IWP at night. SYN1 results are also heavily dependent on geostationary satellite retrievals and is prone to biases at boundaries where the source of geostationary data changes. This can be seen directly by examining SYN1 IWPs along longitudes 90°E and 180° in Fig. 9a, where sudden artificial cutoffs in IWP support the hypothesis that the dataset is prone to biases from geostationary satellite influences as these demark boundaries where different geostationary satellites are used to fill in satellite overpass gaps. As such, this study focuses on comparing the GISS GCM simulated IWPs with 2C-ICE retrievals, as these are believed to be more accurate estimates of true atmospheric IWC. C5 and P5 simulated IWPs agree well with 2C-ICE retrievals over the tropics (±20°), but all three versions of the GCM are biased low over the mid-latitudes given that 2C-ICE retrieves all IWC content while the GCM reports only stratiform IWC content.

IWPs in the C5 and P5 versions of the GISS GCM match well with 2C-ICE retrieved IWPs over the tropics, but undersimulate IWPs outside of the Tropics by generally by ~100 to 150 g m^{-2}. Direct comparisons (not shown here) between C5 and P5 GCM simulations and 2C-ICE retrievals show that both the C5 and P5 simulations tend to oversimulate/undersimulate IWPs over the ocean/land within the Tropics, respectively. While zonally averaged IWPs in C5 and P5 suggest minimal changes between these two simulations, changes within the P5 simulation have led to a regional increase of IWPs over the western Pacific and the area around Indonesia, and slightly decreased IWPs over the Eastern Pacific ITCZ. These two regions are of particular interest in this study and as such will be discussed more thoroughly throughout this study as the following: (1) the Eastern Pacific Northern ITCZ (EP-ITCZ), and (2) Indonesia and the Western Pacific (INDO-WP).

Recent changes to ice particle distributions and ice particle fall speeds in the E5 version of the GCM have resulted in strong decreases in IWP globally in comparison to 2C-ICE retrievals and previous versions of the GCM. E5 simulated IWPs are lower than SYN1 retrievals which have a muddled pattern and strength due to night retrieval issues. Correlations between the 2C-ICE and the three versions of the GCM are very close, between 0.65 and 0.66, while root-mean-square deviations (RMSD) have slightly increased with each iteration of the GCM, from 82.8 (C5) to 98.2 g m^{-2} (E5). Given the increase in ice particle fall speeds, it's possible that fall speeds are too high causing over-sedimentation of ice in the model. Further investigation is warranted, however, given the caveat that 2C-ICE retrieves all ice content while the model reports stratiform IWC.

As mentioned prior, two regions are of particular interest in this study in regard to how these areas have changed with each modification to the NASA GISS GCM: (1) the Eastern Pacific Northern ITCZ (EP-ITCZ), and (2) Indonesia and the Western Pacific (INDO-WP). Probability density functions (PDFs) and scatterplots of IWPs retrieved from 2C-ICE against those from SYN1 and the C5, P5, and E5 versions of the GCM over the EP-ITCZ (Fig. 11) and the INDO-WP (Fig. 12) regions. Values of the cumulative distribution function (CDF) associated with the final bin are provided in parenthesis in Figures 11a and 12a next to the associated data. Statistics of regional weighted means, standard deviations, and correlations and RMSDs in reference to 2C-ICE retrieved IWPs over these two focused regions are listed in Table 4.

Over the EP-ITCZ region, the pattern of SYN1 retrieved IWPs agree reasonably well with 2C-ICE retrievals, however, the regional mean IWP for SYN1 (113.7 g m^{-2}) is much lower than the mean IWP retrieved by 2C-ICE (151.7 g m^{-2}). SYN1 retrieved IWPs are more centered in the lower bins while 2C-ICE retrievals have a broader and more even distribution (Figs. 11a&b). The C5 and P5 versions of the GCM simulate much more ice water compared to 2C-ICE (Figs. 11c&d), with regional means of 213.8 and 191.0 g m^{-2} and correlations of 0.88 and 0.89, respectively. The newest version of the GCM, E5, simulates much less ice water within the EP-ITCZ region (27.3 g m^{-2}) with a much lower correlation (0.47) and higher RMSD (155.9 g m^{-2}) compared to 2C-ICE retrievals.

Table 4. Statistics of retrieved and simulated IWPs over the two selected regions: EP-ITCZ and INDO-WP Statistics presented include regional means and standard deviations given in g m^{-2}, as well correlations and RMSDs in comparison with 2C-ICE retrievals

Region 1 – Eastern Pacific Northern ITCZ [EP-ITCZ]				
Dataset	Regional Mean [g m^{-2}]	Std. Dev. [g m^{-2}]	Corr. [2C-ICE]	RMSD [2C-ICE]
SYN1	113.7	47.7	-	-
2C-ICE	151.7	102.9	-	-
GISS C5	213.8	139.1	0.88	93.2
GISS P5	191.0	146.3	0.89	82.0
GISS E5	27.3	22.8	0.47	155.9
Region 2 – Indonesia and Western Pacific [INDO-WP]				
Dataset	Regional Mean [g m^{-2}]	Std. Dev. [g m^{-2}]	Corr. [2C-ICE]	RMSD [2C-ICE]
SYN1	85.9	23.5	-	-
2C-ICE	243.9	123.2	-	-
GISS C5	225.1	146.6	0.62	120.7
GISS P5	258.6	188.4	0.61	150.1
GISS E5	88.9	64.2	0.59	183.7

Over the INDO-WP region, SYN1 retrieved IWPs are much lower than 2C-ICE (85.9 vs. 243.9 g m^{-2}) as this region is located within the boundaries of where SYN1 retrievals suddenly decreased, presumably due to geostationary satellite influences. Regional mean IWPs simulated by C5 and P5 (225.1 and 258.6 g m^{-2}, respectively) agree very well with 2C-ICE retrievals. The regional standard deviation in the P5 simulation (188.4 g m^{-2}), however, is much larger than both its predecessor (C5, 146.6 g m^{-2}) and 2C-ICE (123.2 g m^{-2}), potentially due to P5 having higher frequencies in the larger bins of ice water (Fig. 12a). Again, E5 simulated IWPs are much lower than its predecessors and 2C-ICE retrievals.
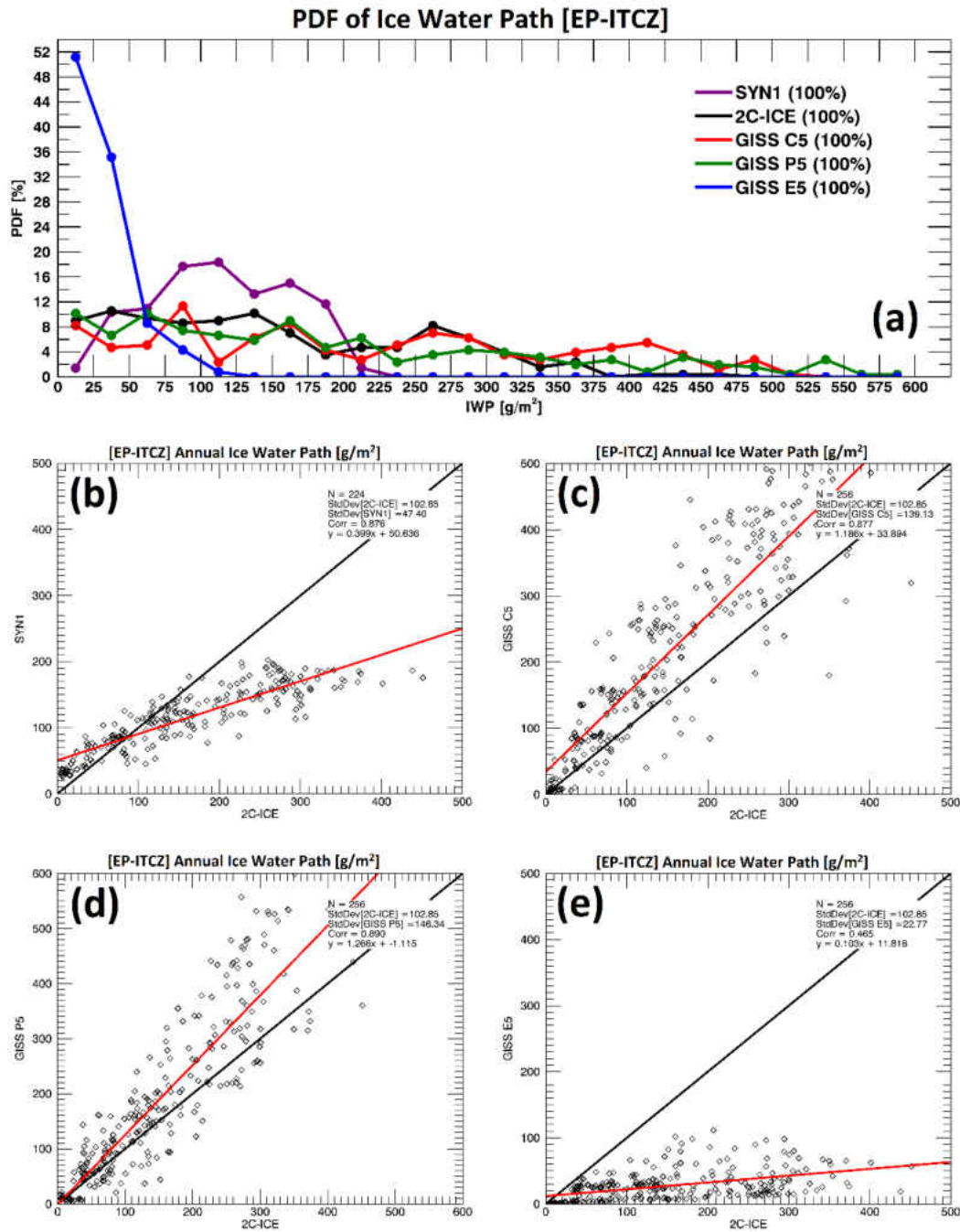
Figure 11. (a) PDFs of IWPs retrieved from (purple) SYN1 and (black) 2C-ICE, and simulated by the (red) C5, (green) P5, and (blue) E5 within the EP-ITCZ region, and scatterplots of IWPs retrieved from 2C-ICE vs. IWPs from (b) SYN1, (c) C5, (d) P5, and the (e) E5.
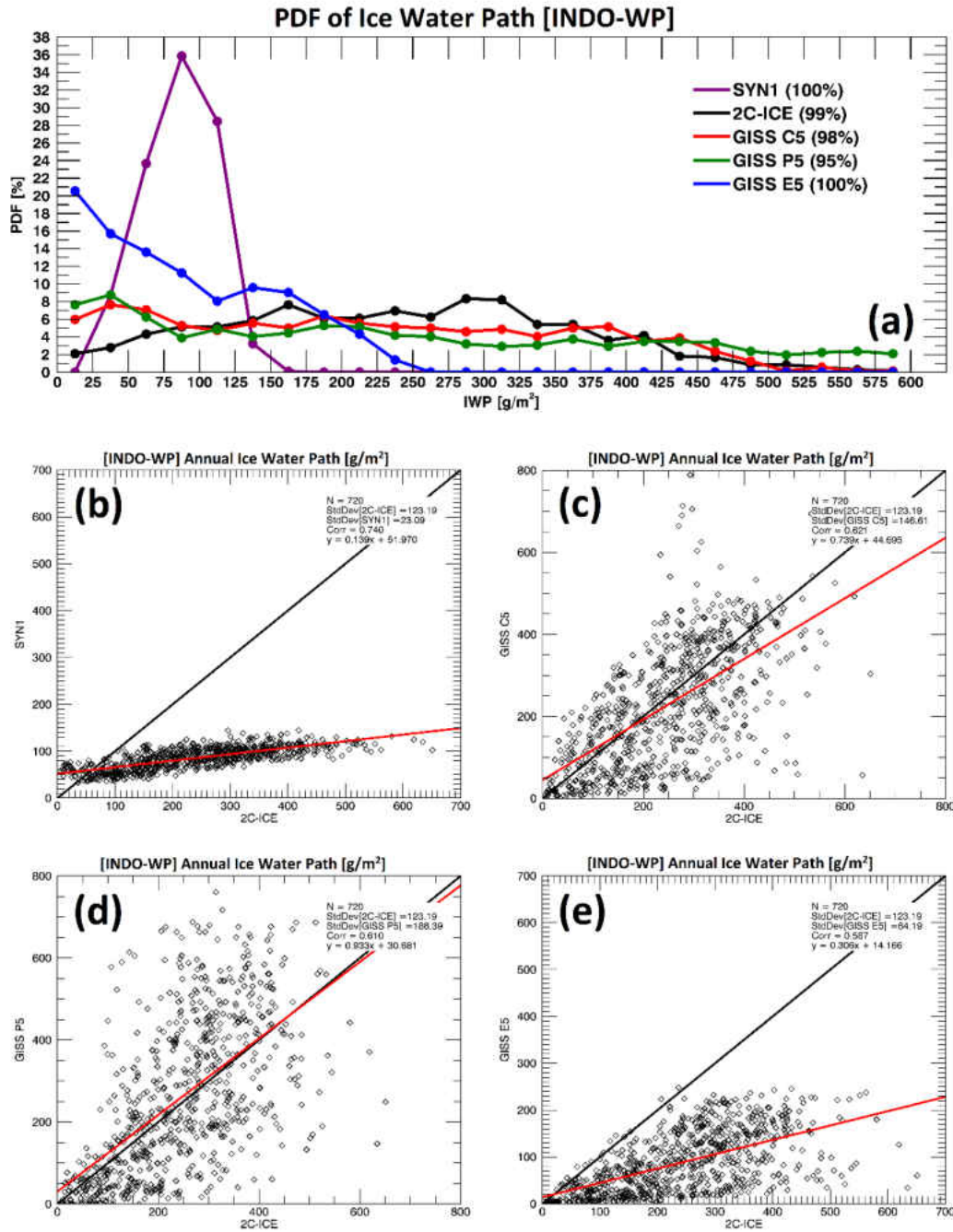
Figure 12. As in Fig. 11 except for over INDO-WP. [g/m^2]

4.3.2.2 Ice Water Content (IWC)

Having examined the total amounts of ice water simulated by the different versions of the NASA GISS GCM and how this amount changes with each iteration of the GCM, it is imperative to then examine at what levels in the atmosphere these changes occur and to ensure that this is simply not a case of biases counterbalanced by one another.

Figure 13 shows annual averages of zonal IWCs retrieved from 2C-ICE, simulated by three versions of the NASA GISS GCM (C5, P5, E5) and the MERRA2 reanalyses. The MERRA2 reanalysis is included in all IWC comparisons because the reanalysis will be important to later discussions of vertical motion as the only 'semi-observational' source for comparison. Horizontal IWC slices at 100, 210, and 300 hPa are shown in Figure 15, while IWC slices at 500, 600, and 850 hPa are shown in Figure 14. Averaged vertical profiles of IWC are split into three regions based on latitude: the tropics (±30°), the mid-latitudes (between ±30°-60°), and the poles (between ±60°-90°) as shown in Figure 16. From previous IWP discussions, it is known that the C5 and P5 simulations, in general, simulate more/less ice water over the ocean/land within the Tropics while undersimulating IWPs outside of the Tropics.

Comparing IWC in the lower portion of the atmosphere, it is shown that all three versions of the NASA GISS GCM (C5, P5, and E5) undersimulate IWC in the poles and the midlatitudes at 600 and 800 hPa in comparison with 2C-ICE retrievals. MERRA2 simulates even less IWC than all three versions of the GCM (Fig. 13, 14, & 16c). Comparing the C5, P5, and E5 at these two levels shows minor differences in magnitude and spatial pattern, with E5 IWC slightly higher than IWCs in both C5 and P5. It is

hypothesized that the increase in lower level IWC in E5 is a result of increased ice particle fall speeds in the E5 simulation. Around 500 hPa, the GCM simulated IWCs are closer to those retrieved from 2C-ICE in the midlatitudes, but still remain much less in the Tropics (Fig. 13, 14, 16b&c).

At 300 hPa, the C5 and P5 simulate much more IWC globally than is retrieved by 2C-ICE (Fig. 15), while the E5 simulation continues to simulate less IWC in the Tropics and slightly more IWC in the midlatitudes in comparison with 2C-ICE (Figs. 16a&b). C5 and P5 continue to simulate much more IWC than 2C-ICE at the 215 hPa level and above in the tropics (Fig. 16a). Near 215 hPa, the E5 GCM simulation begins to match 2C-ICE retrievals and continues through the upper-most portions of the atmosphere (Figs. 15 & 16a).
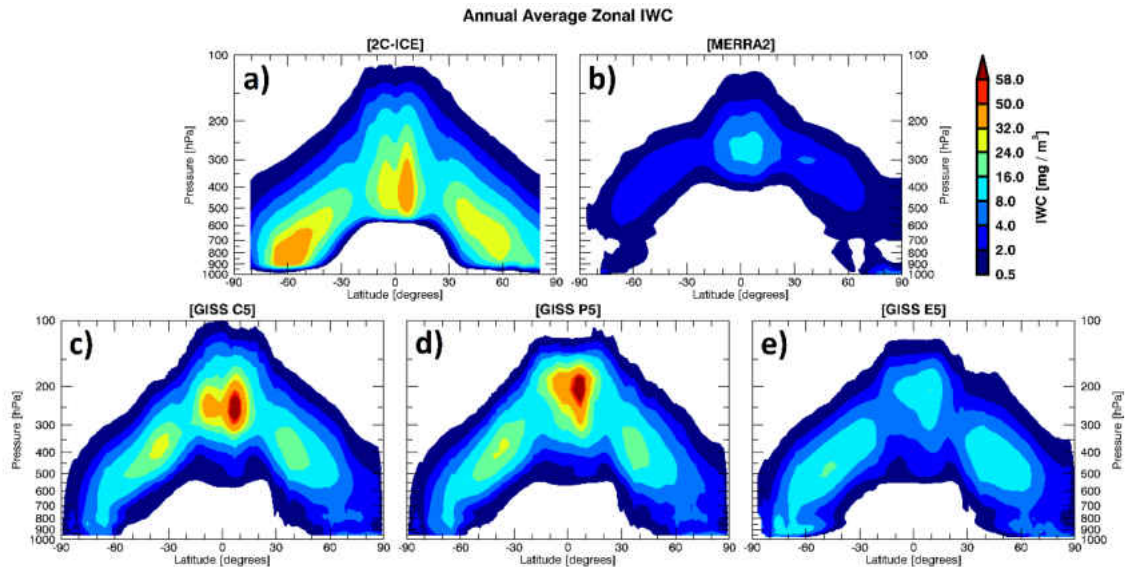
Figure 13. Annually averaged zonal IWC for (a) gridded 2C-ICE retrievals, (b) the MERRA2 reanalysis, and the (c) C5, (d) P5, and (e) E5 NASA GISS GCM simulations.

When examining the vertical distribution more closely in Figures 13 and 16, an interesting pattern emerges. IWCs retrieved from 2C-ICE peak low in the atmosphere and gradually decreases with height, which is consistent to the findings in Deng and Mace (2015) using DOE ARM radar-lidar observations over three ARM surface sites. In contrast, the GCM simulated IWCs increase with height and reach the maximum values at upper levels. The GCM simulated IWCs in all three versions peak at nearly the same pressure level in the midlatitudes (Figs. 16b), however, this is not the case when analyzing the simulated IWCs in the Polar Regions and in the Tropics. MERRA-2 IWCs are much lower in comparison with retrievals from 2C-ICE and IWC simulated from the three versions of the GCM at all levels globally.

IWC profiles within the two regions of interest in general match previous tropical IWC comparisons, with all versions of the GCM peaking higher in the atmosphere than in 2C-ICE. A key difference is found when comparing the latest E5 GCM simulation in these two focus regions where the E5 simulated IWCs increase at a lower rate within the EP-ITCZ compared to INDO-WP, which may be a result of better MJO-like simulation in the updated E5 version of the GCM.
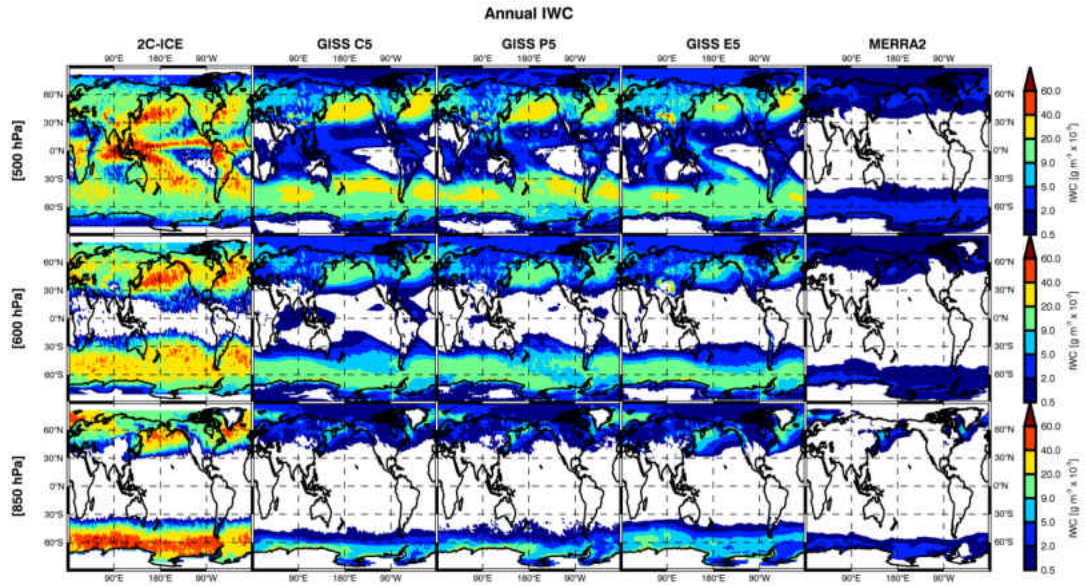
Figure 14. Vertical layers of annually averaged global IWC at (top row) 500, (middle row) 600, (bottom row) 850 hPa for (1st column) 2C-ICE retrievals, (2nd column) the MERRA2 reanalysis, and the (3rd column) C5, (4th column) P5, and (5th column) E5 GCM simulations.
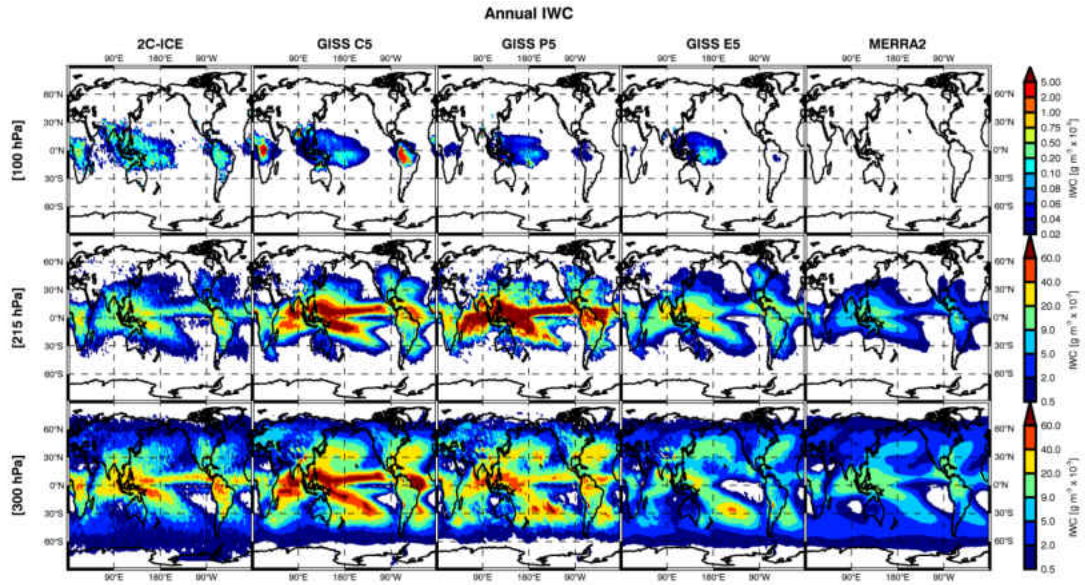
Figure 15. Vertical layers of annually averaged global IWC at (top row) 100, (middle row) 200, (bottom row) 300 hPa for (1st column) 2C-ICE retrievals, (2nd column) the MERRA2 reanalysis, and the (3rd column) C5, (4th column) P5, and (5th column) E5 GCM simulations.
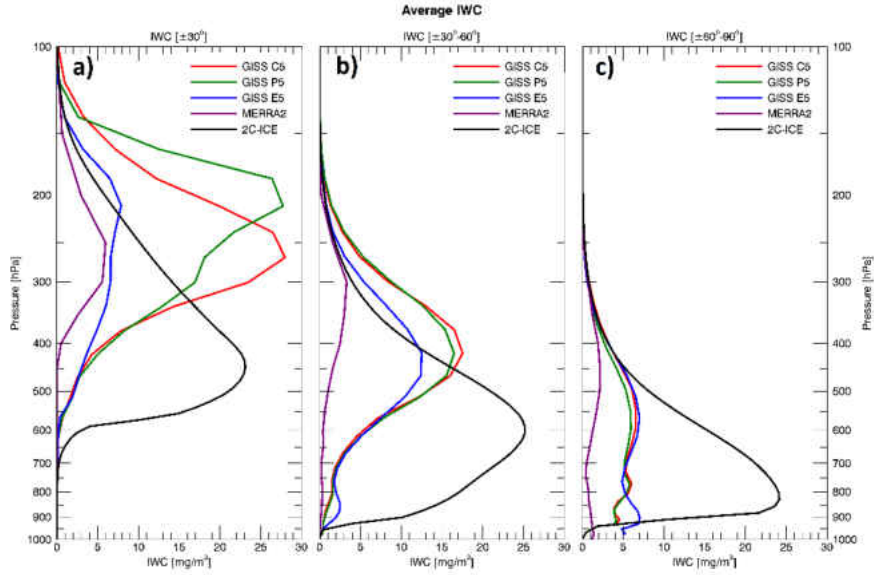
Figure 16. Three regional IWC profiles, defined by latitude, (a) the tropics (±30°), (b) the mid-latitudes (between ±30°-60°), and (c) the poles (between ±60°-90°) of (black) 2C-ICE retrievals, (purple) the MERRA2 reanalysis, and (red) the C5, (green) P5, and (blue) E5 GCM simulations.
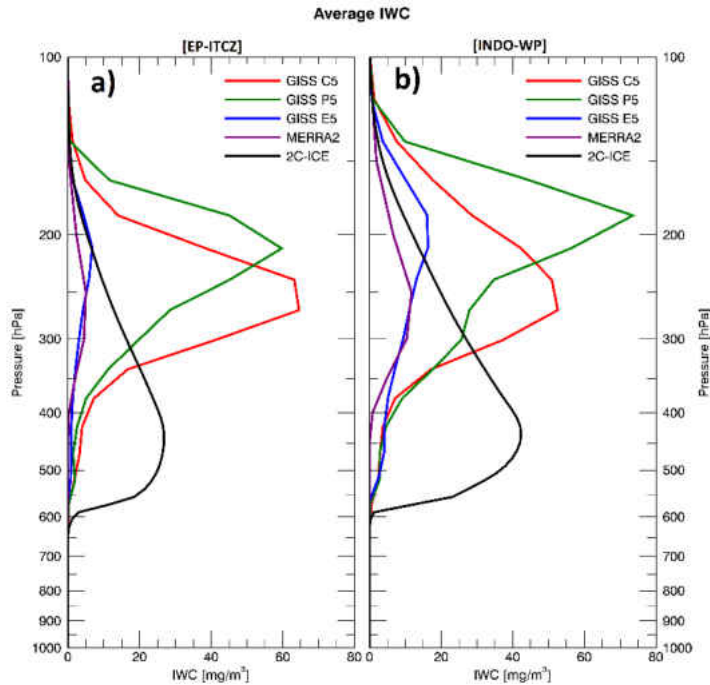
Figure 17. IWC profiles of (black) 2C-ICE retrievals, (purple) the MERRA2 reanalysis, and (red) the C5, (green) P5, and (blue) E5 GCM simulations over the two selected regions of focus: the (a) EP-ITCZ and the (b) INDO-WP.

4.2.3 Vertical Motion (ω)

Given the significant IWC differences in the upper levels of the atmosphere between 2C-ICE retrievals and model simulations, it is imperative to analyze vertical motion at different levels within the three versions of the GCM and observations. Unfortunately, observations of vertical motion on a global scale are scarce, thus the MERRA2 reanalysis is used in this study as a 'semi-observational' dataset. However, it should be noted that vertical motion comparisons with the MERRA2 reanalysis may not be best given the lack of IWC in the reanalysis. Averaged profiles of vertical motion are also classified into three categories based on latitude: the tropics (±30°), the mid-latitudes (between ±30°-60°), and the poles (between ±60°-90°) as shown in Figure 18. Horizontal slices of vertical motion in the MERRA2 reanalysis, and in the C5, P5, and E5 simulations at 500, 600, and 850 hPa are shown in Figure 19, while vertical motion slices at 100, 210, and 300 hPa are shown in Figure 20.

Large-scale intermodal comparisons of vertical motion in the C5, P5, and E5 GCM simulations, as well as comparisons with vertical motion in the MERRA2 reanalysis is challenging given that each source (not shown here) is highly dependent on region and tends to have offsetting biases at larger scales. As such, vertical profile comparisons show little differences, within 5 hPa per day, between each model simulation and the MERRA2 reanalysis (Fig. 18).

Profiles of vertical motion over each focus region are provided in Figure 21. Over the EP-ITCZ, MERRA2 and the C5 and P5 simulations show roughly the same vertical strength in the lower portion of the atmosphere (~800 to 1000 hPa, Fig. 21a.). Above ~800 hPa, the strength of vertical motion in MERRA2 and the P5 simulation both

53

decrease compared to the C5 simulation. Interestingly, the C5 and P5 simulations show an increase in vertical motion strength between 500 and 300 hPa. All profiles within the INDO-WP region show a similar pattern; a steady increase in upward vertical motion strength from the surface up to 500 hPa, and then a gradual decrease in strength above 500 hPa (Fig. 21b).

As mentioned previously in the regional IWC discussions, IWC in the E5 simulation increases at a lower rate over the EP-ITCZ compared to the INDO-WP focus area. Of particular interest is that within the EP-ITCZ, vertical motion simulated in the E5 version of the GCM changes sign at 700 hPa from upward to downward motion (Fig. 21a). It is hypothesized that this weakening and overall change in vertical motion is due to increased atmospheric loading as a result of increased ice particle fall speeds and smaller particle distributions as more albeit smaller particles are now falling out at increased speeds. What makes this particularly interesting is that this effect is not observed to this magnitude within the INDO-WP where the E5 simulates the strongest upward vertical motion of three GCM versions. Closer inter-model inspection of vertical motion comparisons in the GCMs (not shown) suggest that changes in the E5 simulation have resulted in stronger/weaker upward motion over the ocean/land in the INDO-WP region in comparison with its C5 and P5 predecessors.
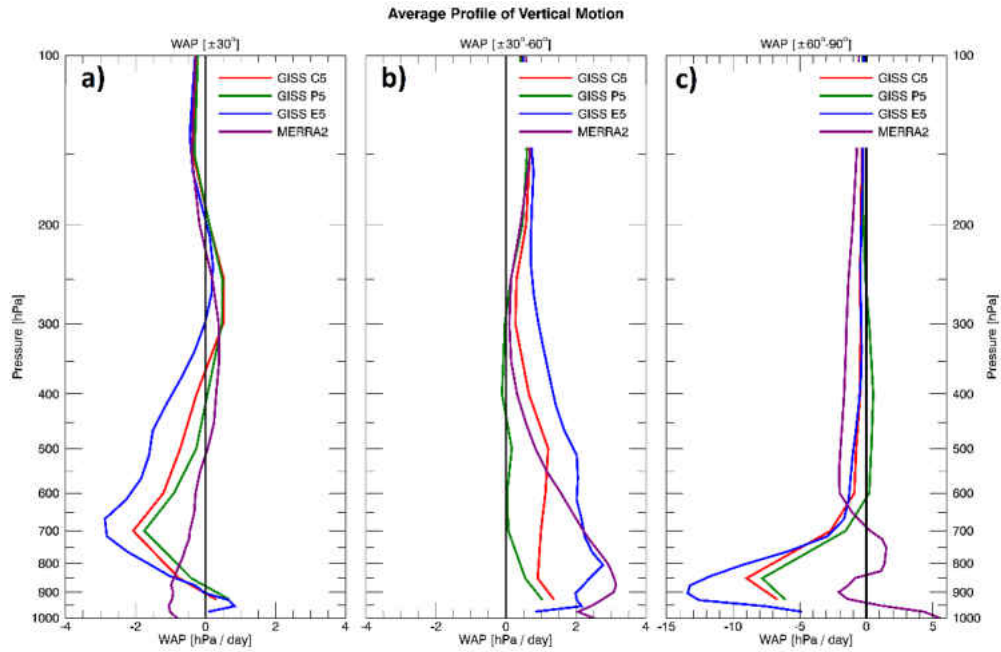
Figure 18. Three regional annual vertical motion profiles, defined by latitude, (a) the tropics (±30°), (b) the mid-latitudes (between ±30°-60°), and (c) the poles (between ±60°-90°) of (black) 2C-ICE observations, (purple) the MERRA2 reanalysis, and (red) the C5, (green) P5, and (blue) E5 GCM simulations.
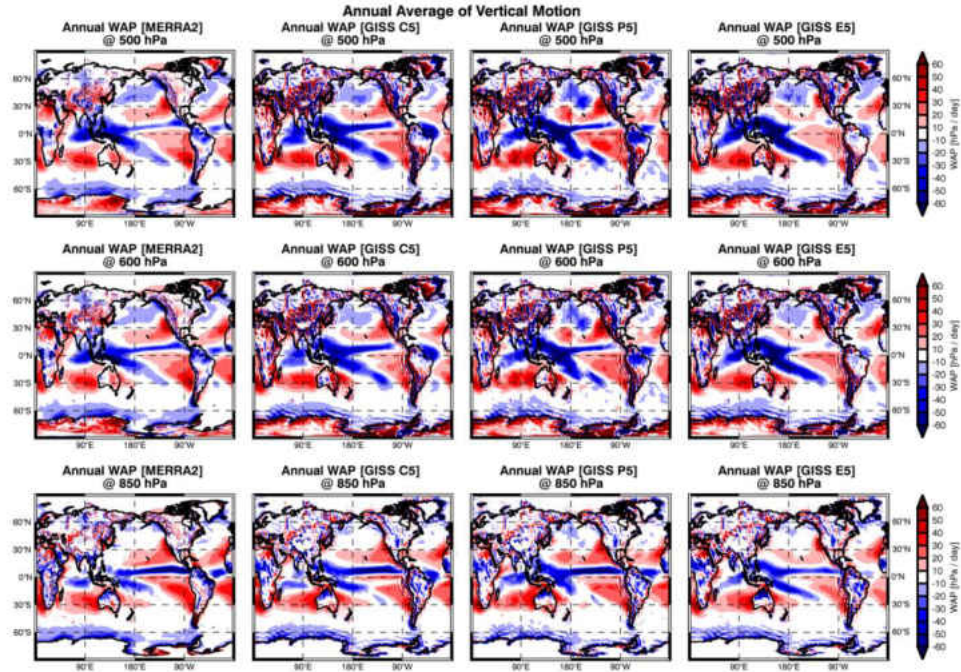
Figure 19. Vertical layers of annually averaged global vertical motion at (top row) 500, (middle row) 600, (bottom row) 850 hPa for (1st column) the MERRA2 reanalysis, and the (2nd column) C5, (3rd column) P5, and (4th column) E5 GCM simulations.
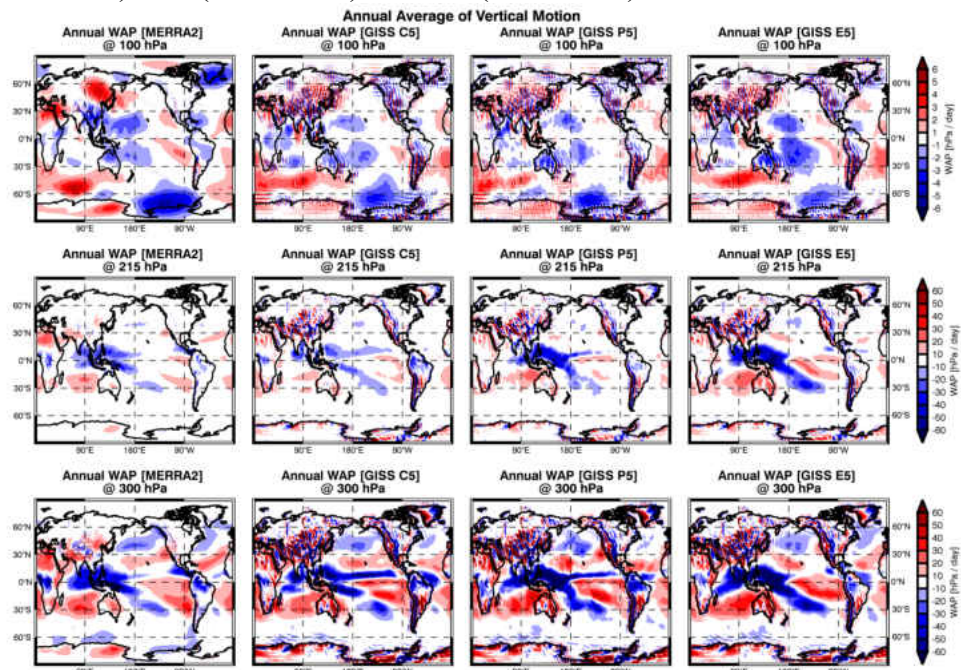
Figure 20. Vertical layers of annually averaged global vertical motion at (top row) 100, (middle row) 215, (bottom row) 300 hPa for (1st column) the MERRA2 reanalysis, and the (2nd column) C5, (3rd column) P5, and (4th column) E5 GCM simulations.

56
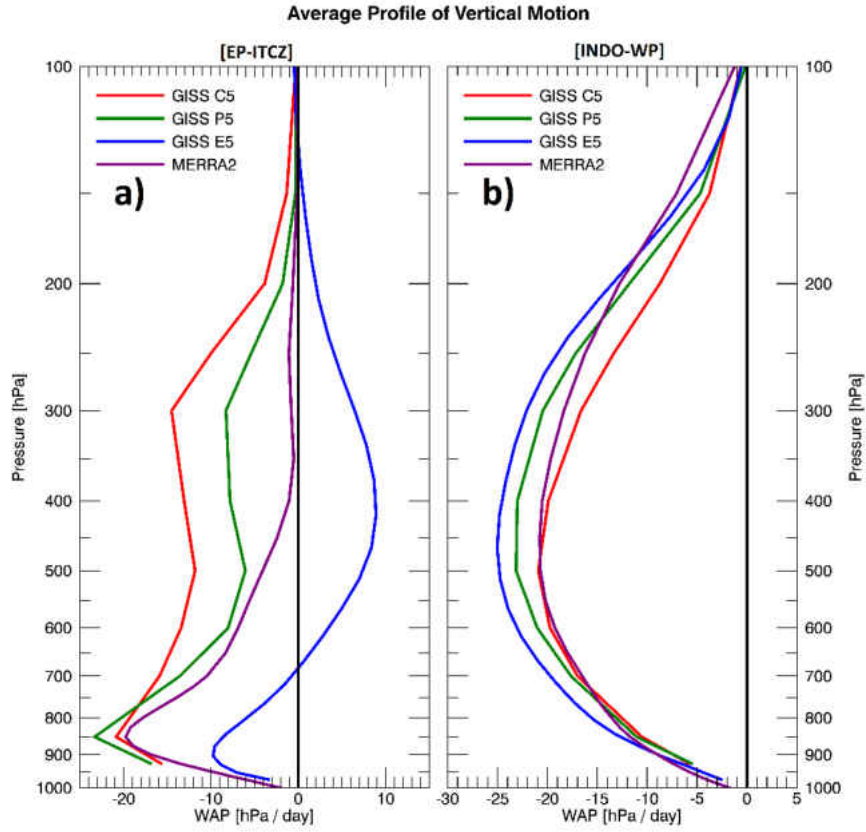
Figure 21. Annual vertical motion profiles of (purple) the MERRA2 reanalysis, and (red) the C5, (green) P5, and (blue) E5 GCM simulations in the two defined regions of interest, the (a) EP-ITCZ, and the (b) INDO-WP.

4.2.4 Total Column Cloud Fraction and Vertical Cloud Profiles

In order to reach radiative balance, the NASA GISS ModelE GCM tunes the minimum relative humidity at which clouds are formed. Previously in Chapter IV, E5 simulated IWC was found to decrease in the E5 version of the GCM. Liquid water content (LWC) was also compared (not shown here) but is not included for brevity as results were similar to the IWC analysis. With the widespread decreases in ice and liquid water contents of the recent NASA GISS E5 simulation, it is imperative to examine how clouds will be affected in order to maintain global radiative balance. Annual total column cloud fraction (CF) of SYN1 passive satellite observations, CCCM active satellite observations, and the C5, and E5 versions of the GISS GCM are shown in Figure 22. Unfortunately, CFs for the current P5 simulation were not available at the time of this study, however, a fairly similar (if not identical) version of the P5 simulation provided was examined in Stanfield et al. (2014) and will be discussed briefly in this section. Zonally averaged annual total column cloud fraction is provided in Figure 23. Global means, standard deviations, and correlations and root-mean-square deviations of the C5 and E5 GCM simulations in comparison with SYN1 retrievals and CCCM active satellite retrievals of total column cloud fractions are listed in Table 5.

As expected when comparing total column cloud fractions derived from passive and active satellite observations, CCCM active cloud fraction observations are higher than SYN1 at almost every point globally, with a global average total column cloud fraction of 75.9% compared to 60.6% observed in SYN1. CFs simulated in the C5 GCM agree well with SYN1 on globally (61.4% global average CF) due to offsetting regional biases. In detail, the C5 GCM simulates cloud frequencies higher than SYN1

observations within the tropics and outside ±60° of latitude, even higher than CCCM observations outside ±70° of latitude, while undersimulating cloud frequency in the midlatitudes. In Stanfield et al. (2014), it was found that changes to the planetary boundary layer parameterization in a P5 version of the NASA GISS GCM resulted in increased total column cloud fraction within the southern midlatitudes (SMLs), specifically by increasing low-level cloud frequency by ~20%. Recent changes in the E5 version of the GCM has decreased CF globally, bringing modeled CFs closer to the C5 simulation over the SMLs and lower than C5 in the tropics and in the Antarctic (Fig. 23) with a global average cloud fraction of 54.3%. While the E5 simulation has the lowest global mean cloud fraction, the latest version of the GCM correlates better than its C5 predecessor with SYN1, 0.54 ← 0.38, and CCCM, 0.67 ← 0.57, CFs, respectively.

Given the tuning method used in the GISS ModelE, an equivalent alteration in vertical E5 simulated cloud structure is expected to counterbalance the noted decreases globally in E5 simulated IWC, LWC, and total column CF. Vertical annually averaged CF profiles for CCCM observations and the C5 and E5 GCM simulations are provided in Figure 24, split into three regions based on latitude: the tropics, midlatitudes, and polar regions. Both the C5 and E5 GCM simulations simulate lower CFs on average across all levels in the tropics and the midlatitudes while still maintain roughly the same vertical pattern as found in CCCM observations (Fig. 24a&b). With the polar regions, the vertical CF patter in the C5 simulation matches well the CCCM above 800 hPa, however, below 800 hPa the C5 model simulates a decrease in CF while CFs in CCCM observations show an increase and peak in low level CF (Fig. 24c). The E5 simulation within the polar regions does not follow the patterns found in C5 and CCCM, and instead peaks at the

surface and shows a steady decrease in CF vertically. Comparing the C5 and E5 simulations, it is found that CFs in the E5 simulation peak at a lower altitude compared to its C5 predecessor. Given that CFs are lower in the E5 simulation, and may potentially be less optically thick given the decreases observed in IWC and LWC, this lowering of cloud altitude could increase outgoing longwave radiation from higher cloud top temperatures and would help to counterbalance potential reduced reflected shortwave radiative from having lower clouds frequencies and decreased optical depths.
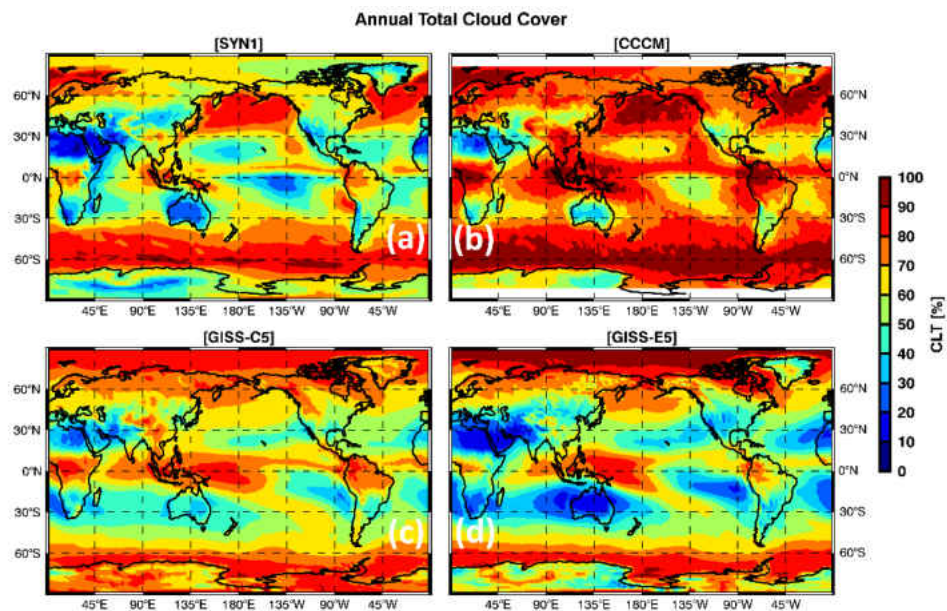
Figure 22. Annually averaged total column cloud fractions for (a) SYN1 passive satellite observations, (b) CCCM active satellite observations, and the (c) C5, and (d) E5 GISS GCM simulations.

Zonal Annual Total Column Cloud Fraction
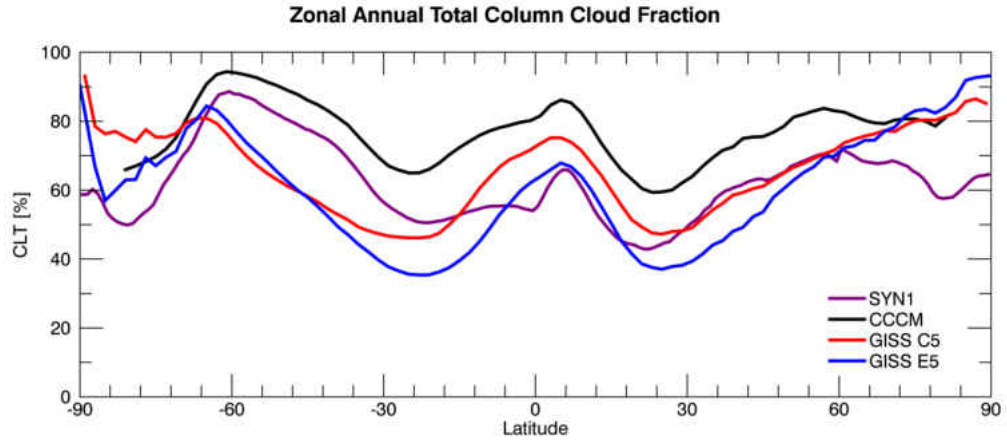
Figure 23. Annually averaged zonal total column cloud fractions for (purple) SYN1 passive satellite observations, (black) CCCM active satellite observations, and the (red) C5, and (blue) E5 GISS GCM simulations.

Table 5. Annual total column cloud fraction weighted means, standard deviations, and correlation and root-mean-square deviation (RMSE) in relation to 2C-ICE satellite observations on a global scale.

Dataset	Global Mean [%]	Std. Dev. [%]	Corr. [SYN1]	RMSD [SYN1]	Corr. [CCCM]	RMSD [CCCM]
SYN1	60.6	16.0	-	-	-	-
CCCM	75.9	13.7	-	-	-	-
GISS C5	61.4	14.5	0.38	17.4	0.57	18.2
GISS E5	54.3	19.9	0.54	17.6	0.67	23.3
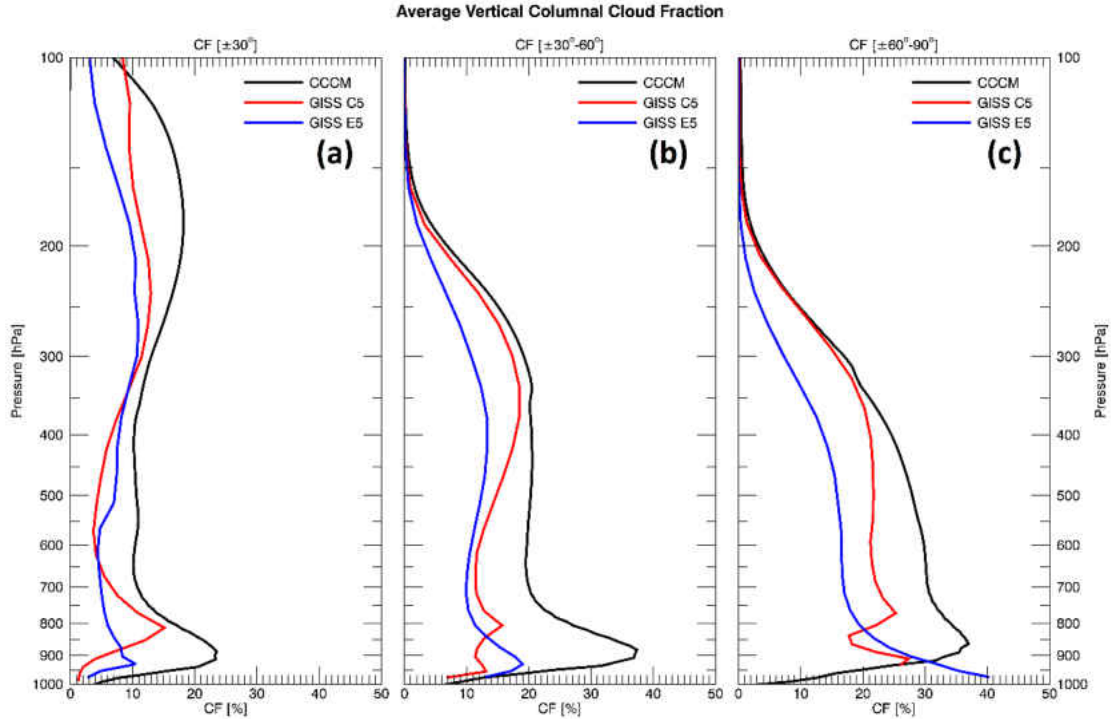
Figure 24. Three regional annually averaged CF profiles, defined by latitude, (a) the tropics (±30°), (b) the mid-latitudes (between ±30°-60°), and (c) the poles (between ±60°-90°) of (black) CCCM satellite observations and (red) the C5 and (blue) E5 GCM simulations.

Statistics of regional weighted means, standard deviations, and correlations and RMSDs in comparison with SYN1 and CCCM observations based on the EP-ITCZ and the INDO-WP regions are listed in Table 6. E5 simulated total column CFs in both focus regions, the EP-ITCZ and the INDO-WP, have decreased in comparison with its C5 predecessor, bringing E5 simulated CFs (EP-ITCZ, 59.2%; INDO-WP, 61.9%) more in line with SYN1 total column CF (EP-ITCZ, 55.0%; INDO-WP, 57.2%) in terms of regional averages. While changes to the E5 GCM have decreased E5 simulated CFs compared to its C5 predecessor in both the EP-ITCZ and the INDO-WP, the E5 is found to correlate better with SYN1 (0.50 → 0.66) and CCCM (0.66 → 0.69) in the EP-ITCZ, while performing slightly worse in the INDO-WP compared to SYN1 (0.63 → 0.61) and

CCCM (0.75 → 0.73) observations. Vertical CFs in both EP-ITCZ and INDO-WP regions agree with previous tropical CF comparisons in that E5 simulates clouds lower in the atmosphere while simulating fewer clouds than CCCM observations (not shown here).

Table 6. Statistics detailing total column cloud fraction found in the EP-ITCZ and INDO-WP regions. Statistics presented include regional means and standard deviations given in g m^{-2}, as well correlations and RMSDs in comparison with SYN1 passive satellite observations and CCCM active satellite observations.

Region 1 – Eastern Pacific Northern ITCZ [EP-ITCZ]						
Dataset	Mean [%]	Std. Dev. [%]	Corr. [SYN1]	RMSD [SYN1]	Corr. [CCCM]	RMSD [CCCM]
SYN1	55.0	11.5	-	-	-	-
2C-ICE	78.7	7.6	-	-	-	-
GISS C5	68.1	5.4	0.50	14.2	0.66	12.0
GISS E5	59.2	7.0	0.66	8.7	0.69	20.3
Region 2 – Indonesia and Western Pacific [INDO-WP]						
Dataset	Mean [%]	Std. Dev. [%]	Corr. [SYN1]	RMSD [SYN1]	Corr. [CCCM]	RMSD [CCCM]
SYN1	57.2	12.2	-	-	-	-
2C-ICE	83.7	9.4	-	-	-	-
GISS C5	70.5	10.7	0.63	14.9	0.75	15.0
GISS E5	61.9	20.8	0.61	16.6	0.73	26.7

4.2.5 Precipitable Water Vapor

Average annual PWVs are shown in Figure 25, given in units of grams per square meter, of AMSR-E satellite observations and for the C5, P5, and E5 versions of the GCM. Zonal averages of annual PWV are provided in Figure 26. Global means, standard deviations, and correlations and root-mean-square deviations of the GCM simulations in comparison with AMSR-E observations are provided in Table 7.

On a global scale, the new changes implemented in the E5 simulation brings the global mean PWV in the model to perfect agreement with ASMR-E observations at 28.0 g m^{-2}. On a regional scale, however, it is shown that the E5-simulated PWV is much higher than AMSR-E observations and both of its predecessors (C5 and P5) within the tropics (Fig. 26). Outside of the tropics, E5-simulated PWVs are lower than AMSR-E observations but remain higher than both C5 and P5. Despite these regional differences, all three versions of the GISS GCM maintain a near perfect correlation (0.99) with AMSR-E observations.

Table 7. Annual PWV weighted means, standard deviations, and correlation and root-mean-square deviation (RMSE) in relation to TRMM observations on a global scale.

Dataset	Global Mean [g m^{-2}]	Std. Dev. [g m^{-2}]	Corr. [TRMM]	RMSD [TRMM]
AMSR-E	28.0	14.1	-	-
GISS C5	22.9	14.2	0.99	2.9
GISS P5	24.4	15.2	0.99	2.4
GISS E5	28.0	17.6	0.99	4.8
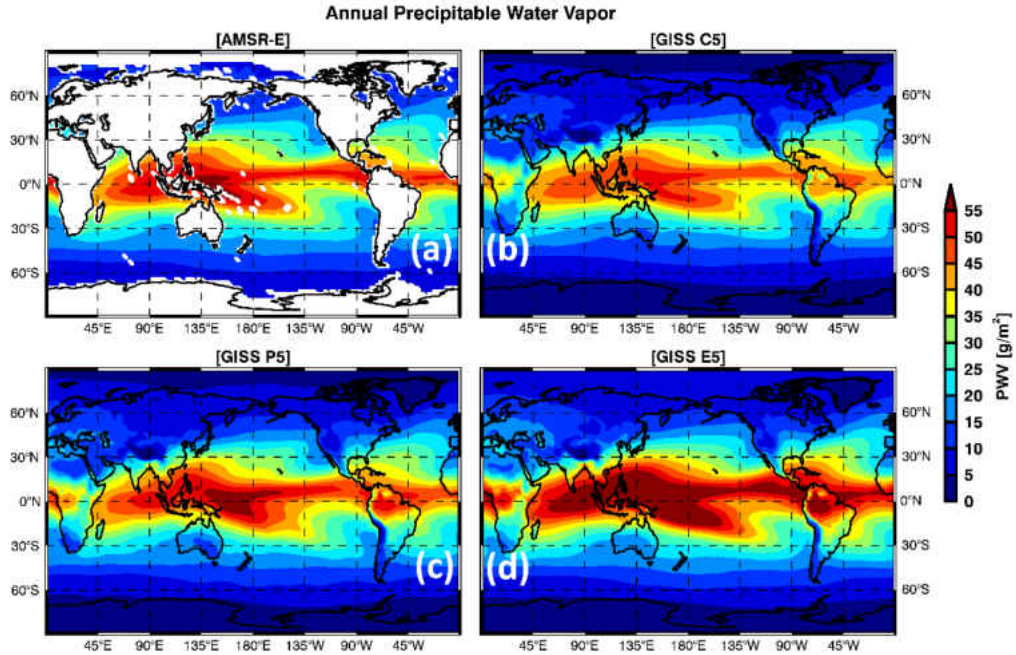
Figure 25. Annually averaged PWV, given in units of g m^{-2}, for (a) AMSR-E observations, and for the (c) C5, (d) P5, and (e) E5 versions of the NASA GISS GCM.
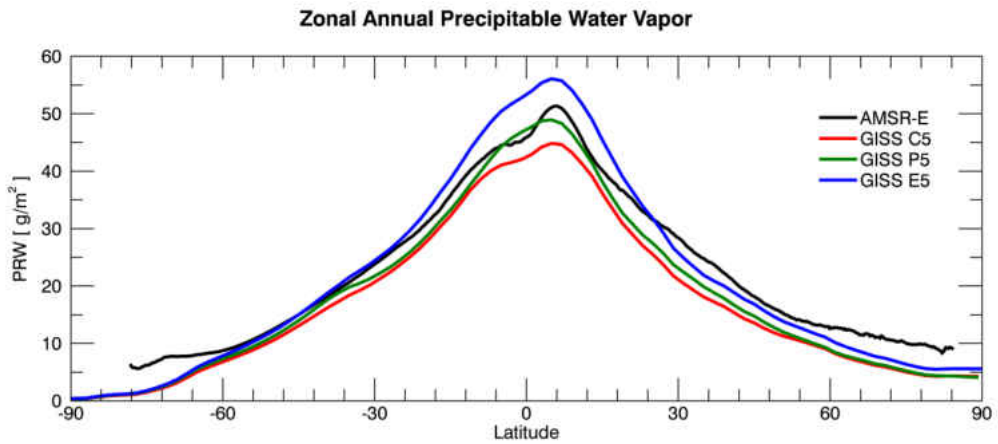
Figure 26. Zonal annually averaged PWV, given in units of g m^{-2}, for (black) AMSR-E observations, and for the (red) C5, (green) P5, and (blue) E5 versions of the NASA GISS GCM.

4.3 Summary of Cloud Properties

In Stanfield et al. (2014), NASA GISS CMIP5 (C5) and Post-CMIP5 (P5) simulated cloud fractions and cloud properties were assessed utilizing satellite retrievals from CERES-MODIS, CloudSat/CALIPSO, AIRS, and AMSR-E, with a particular focus on the southern mid-latitudes (SMLs). Based on multiyear comparisons of P5 and C5 versions of the GISS E2 GCM against observations, the following conclusions were made:

1) While GISS P5 and C5 global mean total column Cloud Fractions (CFs) remain within 1% of each other, the P5 total column CFs have better regional agreement with CERES-MODIS (CM) and CloudSat/CALIPSO (CC) retrieved CFs compared to its C5 predecessor. Changes to the PBL scheme implemented in the GISS P5 GCM have resulted in improved total column CFs, particularly in the SMLs where low-level CFs have increased by nearly 20% in relation to C5 simulations. Over the tropics, the P5-simulated total column CFs are slightly lower than the C5 results, primarily due to the boundary layer changes as well.

2) Although the overall global distributions of CWP from both P5 and C5 are fairly similar to CM and CS results, their global mean CWPs are higher than both CM and CS, primarily due to the over-simulation of CWPs within the tropics. P5-simulated CWPs over the tropics are however much lower than C5 results, bringing the simulation closer to observations. This improvement directly reflects the shallower boundary layer in the P5 simulation. Over the tropics, the decrease in CWP from the C5 to the P5 version of the model is

66

consistent with the decrease observed in total column CF, whereas comparing CWP and total column CF over the SMLs shows the opposite relationship, most likely an artifact due to a shift from stratiform cloud to shallow convection, whose condensate is not accounted for in the CWP diagnostic.

3) Precipitable water vapor comparisons show an increase in P5 simulated PWV compared to the C5 simulation, due to stronger convective rain evaporation in the P5 version of the GISS-E2. Compared to AIRS, the P5 results predominantly show a small positive bias throughout the model. This result is reasonable given the dry bias associated with AIRS retrieval limitations in vertical range and for overcast conditions. Although the global AIRS and C5 PWV patterns and means are very close to each other, the C5 simulated PWV values are much lower than the AIRS retrievals over land. These discrepancies are reduced significantly in P5 simulations. Over the ocean, the P5 results agree better with AMSR-E retrievals globally, particularly over the SMLs.

4) The P5 simulated RHs are greater than the C5 means. For regional comparisons, both the P5 and C5 low-level RH patterns are wetter than the AIRS retrievals over the tropics, slightly more so for the P5 simulation compared to C5 results. Over the SMLs, the P5 and C5 low-level RHs are ~10% higher and lower than the AIRS retrievals, respectively. This finding is consistent with the CF comparison and provides strong support for the increase in the number of low-level clouds simulated by P5 over the SMLs. Over the Polar Regions, the GCM simulations are drier than the AIRS retrievals.

5) Spatial variability analyses using Taylor diagrams indicate overall better correlations and small standard deviations in PWV and RH comparisons between P5/C5 simulations and AMSR-E/AIRS observations. For CF and CWP/LWP/IWP comparisons, the P5 and C5 simulations have moderate correlations (~0.5 - 0.8), but large standard deviations (1 - 2σ) compared to CC results, while having low correlations (0.2 - 0.6) and standard deviations (~1σ) compared to CM observations. Although some improvements have been made to the P5 simulation on a global scale, large improvements have been found within the SML region, where correlations have increased while bias and RMSE have significantly decreased compared to the C5 simulation.

Overall, the changes implemented in the GISS P5 GCM, especially the changes in boundary layer depth, have shown a significant improvement in model-simulated clouds and cloud properties. GISS GCM simulations are generating more clouds within the SMLs, and are beginning to produce more marine stratocumulus clouds as well. Water path and PWV measurements continue to show improvement, particularly over the SMLs. At the time of Stanfield et al. (2014), available observations contained relatively large uncertainties over the polar regions. A more recent study, Dong et al. (2016), compared new CERES Edition 4 CFs and cloud properties over the ARM NSA site with ARM NSA observations and retrievals (Dong et al., 2016).

Recently, an improved parameterization of convective cloud ice was developed by Elsaesser et al. (2017) which incorporates new particle size distributions for convective outflow and a new ice particle fall speed formulation. This study has examined how fields of ice water path (IWP), ice water content (IWC), vertical motion,

cloud fraction (CF), and precipitable water vapor (PWV) changed in three iterations of the NASA GISS ModelE GCM.

1) Recent changes to the E5 GCM have decreased IWCs at all levels globally compared to its previous versions and 2C-ICE retrievals. The GCM simulated IWCs increase with height, peaking in the upper portions of the atmosphere, while 2C-ICE retrievals peak in the lower levels of the atmosphere and decrease with height, effectively opposite of each other. EP-ITCZ and INDO-WP comparisons show that E5 simulated IWCs decrease faster with height in the EP-ITCZ region.

2) Regional biases make large-scale comparisons unreliable and uninteresting. Vertical motion within the newest E5 simulation is greatly weakened with increasing height in the EP-ITCZ focus region potentially due to atmospheric loading from enhanced ice particle fall speeds. Comparatively, E5 simulated upward motion in the INDO-WP is stronger than in both its predecessors. Changes in the E5 simulation have resulted in stronger/weaker upward motion over the ocean/land in the INDO-WP region in comparison with its C5 and P5 predecessors.

3) Previous studies have shown that changes to the PBL parameterization increased CFs within the P5 simulation compared to the previous C5 model. New changes in the E5 simulation have decreased cloud fractions globally compared to P5 while maintaining the same overall spatial pattern. Vertical CF profiles peak lower in the E5 simulation, which will potentially increase outgoing longwave radiation due to higher cloud top temperatures to

counterbalance the decrease in reflected shortwave associated with lower CFs and lower optical depth associated with decreased IWC and LWC in the E5 simulation.

4) On a global-scale, E5-simulated PWVs have an excellent agreement with AMSR-E retrievals. Regionally, the E5 version GCM simulates much higher than both AMSR-E and its predecessors (C5, P5). Correlations with AMSR-E remain very high (0.99) despite regional differences.

CHAPTER V

RADIATION PROPERTIES

This chapter details the analysis of radiative properties discussed in Stanfield et al. (2015), and speculates on the impacts of recently changed cloud parameterizations might have on the radiation budget in the NASA GISS ModelE E5 simulation.

5.1 Stanfield et al. (2015) – NASA GISS CMIP5 vs Post-CMIP5 Radiative Analysis

Stanfield et al. (2015) focused on how the modified cloud properties in the P5 simulation impact the TOA radiation budget and cloud radiative effects. Specifically, Stanfield et al. (2015) compared the P5- and C5-simulated clear-sky and all-sky Outgoing Longwave (LW) Radiation (OLR) and albedos at TOA, as well as their cloud radiative effects (CREs) with CERES-EBAF (CE) results. While the GCM simulated global TOA radiation budget agrees well with CE results, it is necessary to assess the regional changes to the radiation budget associated with the two new schemes in the P5 simulation, particularly over the SMLs and the tropics.

5.1.1 Methodology: Calculations of Cloud Radiative Effect (CRE)

CREs in this study are calculated using the standard methods found in previous studies (Ramanathan et al. 1989; Dong and Mace 2003; Dong et al. 2006 and 2010). As in previous studies, SW and LW CREs at TOA are calculated as the difference between the net TOA fluxes, downwelling minus upwelling, of measurements during all-sky conditions minus clear-sky conditions, as shown in Equations 2 and 3. Net CRE is calculated by summing both SW and LW CREs. Positive values of CRE indicate a

radiative energy gain due to the presence of clouds, a warming effect, while negative values denote a radiative energy loss due to the presence of clouds, a cooling effect.

$$CRE_{SW}(TOA) = \left(SW^{\downarrow} - SW_{all}^{\uparrow}\right) - \left(SW^{\downarrow} - SW_{clear}^{\uparrow}\right),$$

$$= SW_{clear}^{\uparrow} - SW_{all}^{\uparrow} = SW^{\downarrow}(R_{clear} - R_{all}), \tag{2}$$

$$CRE_{LW}(TOA) = \left(LW_{all}^{\downarrow} - LW_{all}^{\uparrow}\right) - \left(LW_{clear}^{\downarrow} - LW_{clear}^{\uparrow}\right),$$

$$= LW_{clear}^{\uparrow} - LW_{all}^{\uparrow}, \tag{3}$$

where $SW_{clear}^{\uparrow}$ and $SW_{all}^{\uparrow}$ represent clear-sky and all-sky reflected shortwave fluxes at TOA, R_{clear} and R_{all} represent clear-sky and all-sky albedos at TOA, and $LW_{clear}^{\uparrow}$ and $LW_{all}^{\uparrow}$ represent clear-sky and all-sky OLRs, respectively.

5.1.1 Outgoing Longwave Radiation (OLR)

Zonal averages of clear-sky OLR for CERES-EBAF (CE), P5, and C5 are shown in Fig. 27a. Overall global patterns of clear-sky OLR appear to be fairly well represented in both the P5 and C5 simulations. It is global OLR analysis showed that both the P5 and C5 simulations appear to underestimate the CE observed clear-sky OLR globally by ~4 and ~8 W m^{-2}, respectively (not shown here). This discrepancy is in part due to the known clear-sky OLR dry bias when comparing GCM simulations to observations.
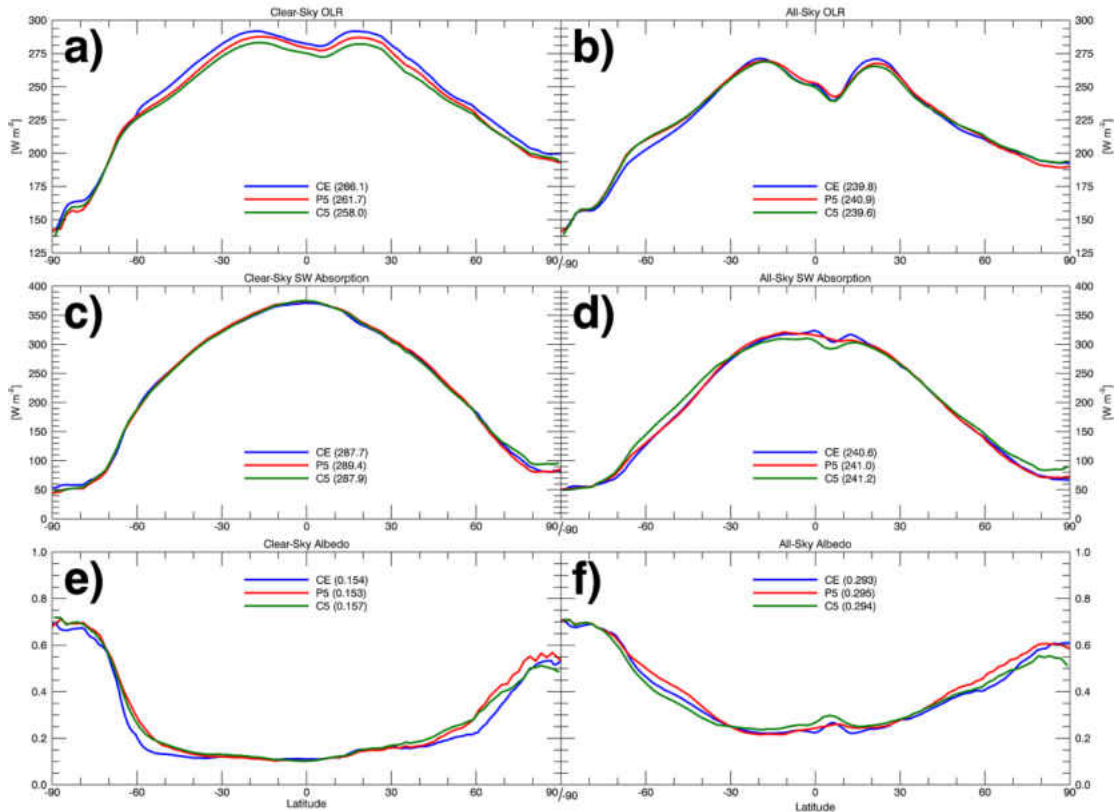
Figure 27. Zonally averaged clear-sky and all-sky (a,b) OLR, (c,d) SW Absorption, and (e,f) albedo for CE (blue), P5 (red), and C5 (green).

The dry bias occurs due to the differing methods used between the GCMs and observations to interpret OLR for clear-sky scenes. To derive the clear-sky OLR, the CERES science team identifies the cloudiness of scenes from MODIS observations using CERES cloud mask algorithms. This results in clear-sky OLR results under truly clear-sky conditions. GCMs, however, are capable of removing the cloud contamination within a scene to calculate clear-sky OLR for clear conditions. As discussed in Sohn et al. (2006), while the clouds are technically removed, the dynamic and thermodynamic conditions that made it favorable to form clouds are still present. More specifically, the modeled hypothetical clear-sky humidity in cloudy regions is wetter than the cloud-free regions identified by the CERES cloud mask. Sohn and Bennartz (2008) found that the

redistribution of water vapor associated with convection results in a significant contribution to LW CRE through the upper tropospheric moistening in the tropics, whereas columnar water vapor variation dominates OLR over the mid-latitudes. Therefore, the CERES observed clear-sky OLR for a scene may be higher than modeled clear-sky OLR, simply on the basis that it is calculated from selected cloud-free pixels, which likely represents drier atmospheric conditions for a given location.

Kato et al. (2013) examined the impact of the dry bias globally, and found a mean difference of -1.25 W m^{-2} between a cloud removed modeled atmosphere and observed clear-sky data. Based on this result, the dry bias can only explain a portion of the clear-sky OLR bias found in this study. Comparisons of clear-sky OLR in Fig. 27a show that observed clear-sky OLRs are slightly higher than both the P5 and C5 results over the mid-latitudes and tropical regions. Sohn and Bennartz (2008) compared AMSR-E derived all-sky PWVs using threshold liquid water paths ranging from 5 to 30 g m^{-2} and found that on average the difference between all-sky and clear-sky PWVs is approximately 2 mm or 2 g m^{-2}. This result was consistent with our findings in Stanfield et al. (Fig. 7; 2014), where the AIRS PWV, which is known to be dry biased due to the lack of retrievals in overcast conditions, is ~2 mm lower than those retrieved from AMSR-E and simulated by P5 over the oceans. It should also be noted that P5 employs a new cumulus parameterization scheme. This scheme modifies convection within the model, making convection generally shallower with less water vapor being detrained into the upper troposphere and more in mid-troposphere. This effect would increase OLR within the P5 simulation, as was observed in Stanfield et al. (Fig. 27). It is hypothesized that PWV

cannot solely explain the differences observed in clear-sky OLR, warranting further study to explore these biases in clear-sky OLR.

For all-sky OLR comparisons, while the P5- and C5-simulated global distributions of OLR are fairly similar to CERES observations and their global means are within ~1 W m^{-2}, large differences exist regionally between the model simulations and the observations (not shown here). These regional differences can be partially explained by our all-sky PWV comparisons from Chapter IV (Fig. 6). For example, the large negative biases of all-sky OLR around the central Pacific (~Equator, 180 °E) and positive biases over Indonesia-Australia have strong negative correlations with their corresponding PWV comparisons from Chapter IV (Figs. 6e and 6f). Regional biases of all-sky OLR also agree well with the total column CF comparisons presented in Fig. 2. More specifically, regions with a strong positive bias in total column CF correspond well with lower all-sky OLR due to the lower LW emission of colder cloud-top temperatures. On the other hand, regions with a strong negative bias in total column CF correspond well with higher values of all-sky OLR due to the higher emission associated with warmer surface temperatures. No significant differences in all-sky OLR are found over the SMLs, where P5-simulated low-level CF has increased by ~20%, as discussed in Chapter IV. It is expected that these low-level clouds have only a minor impact on all-sky OLR due to the small difference between low-level cloud-top temperatures and sea surface temperatures.

Comparing zonally averaged OLR in Fig. 27b, the P5-simulated all-sky OLRs agree well with the CE observations, which is consistent with the good agreement found between P5 and AMSR-E zonally averaged PWV in Chapter IV (Fig. 7b). However,

examining biases in all-sky OLR on a regional scale shows that this result is due to offsetting biases within the GCMs.

5.1.2 Albedo

Zonal averages of clear-sky and all-sky albedos are presented in Figs. 27e and 27f, respectively. The modeled global mean clear-sky albedos agree with CE observations to within 0.01. When comparing the regional differences in clear-sky albedo between the model simulations and CE observations (Figs. 27e and 27f), all results agree well with each other within ±50° latitude. Outside of ±50° latitudes, both P5 and C5 have positive biases which can be seen zonally (Fig. 27e). These biases are potentially due to the differences in clear-sky surface albedo between the observations and those used in the GISS models. This is particularly true closer to the poles where clear-sky albedo is heavily influenced by sea ice albedo, which can be affected by the age of the ice, the presence of snow on the ice, or the formation of melt ponds. While zonal patterns of clear-sky albedo (Fig. 27e) show disagreement outside ±50° latitude, zonal patterns of clear-sky SW absorption show agreement across nearly all latitudes, as shown in Figure 27c.

While a quick comparison of global mean all-sky albedos suggests a good agreement between the models and observations, large biases are found regionally between the models and CE observations (Figs. 27d, 27e). The regional bias patterns in both the P5 and C5 simulations are similar to those in their total column CF comparisons (Figs. 2e and 2f). For example, the P5-simulated total column CF over the SMLs has increased ~20% compared to the previous C5 simulation (Figs. 2a and 3). This increase

in CF has resulted in increased all-sky albedos and decreased shortwave (SW) absorption at TOA in the P5 simulation over the SMLs. P5-simulated all-sky albedos have improved in regions with a known high frequency of MBL clouds, such as off the western coast of North and South America, due to the increase in CF from the newly implemented PBL scheme.

5.1.3 Cloud Radiative Effects (CREs)

LW CREs are shown in Figure 28. The overall global patterns of simulated LW CREs from both P5 and C5 agree fairly well with CE observations. Clouds have a warming effect on the TOA LW radiation budget with a global average of 26.3 W m^{-2} based on CE observations, while P5 and C5 averages are -5.5 W m^{-2} and -7.9 W m^{-2} lower than the observation, respectively. Global means of LW CRE, all-sky and clear-sky OLRs suggest that clear-sky OLR is the main contributor of biases in LW CRE, however, regional analysis suggest a more complicated relationship. Considering the potential dry bias, comparing PWV (Fig. 6) with LW CRE (Fig. 28) suggests a strong correlation between PWV and LW CRE. However, the cloud contribution to LW CRE cannot be ignored. For example, the LW CREs, excluding the polar regions, have strong correlations with CFs shown in Fig. 2. The LW CRE differences also mimic the patterns of their corresponding CF differences (P5-CM and C5-CM in Figs. 2e and 2f of Part I, where CM denotes CERES-MODIS). Therefore, it can be concluded that clouds and PWV both play major roles in calculating LW CRE (Sohn et al. 2006 and 2008, Dong et al. 2006).
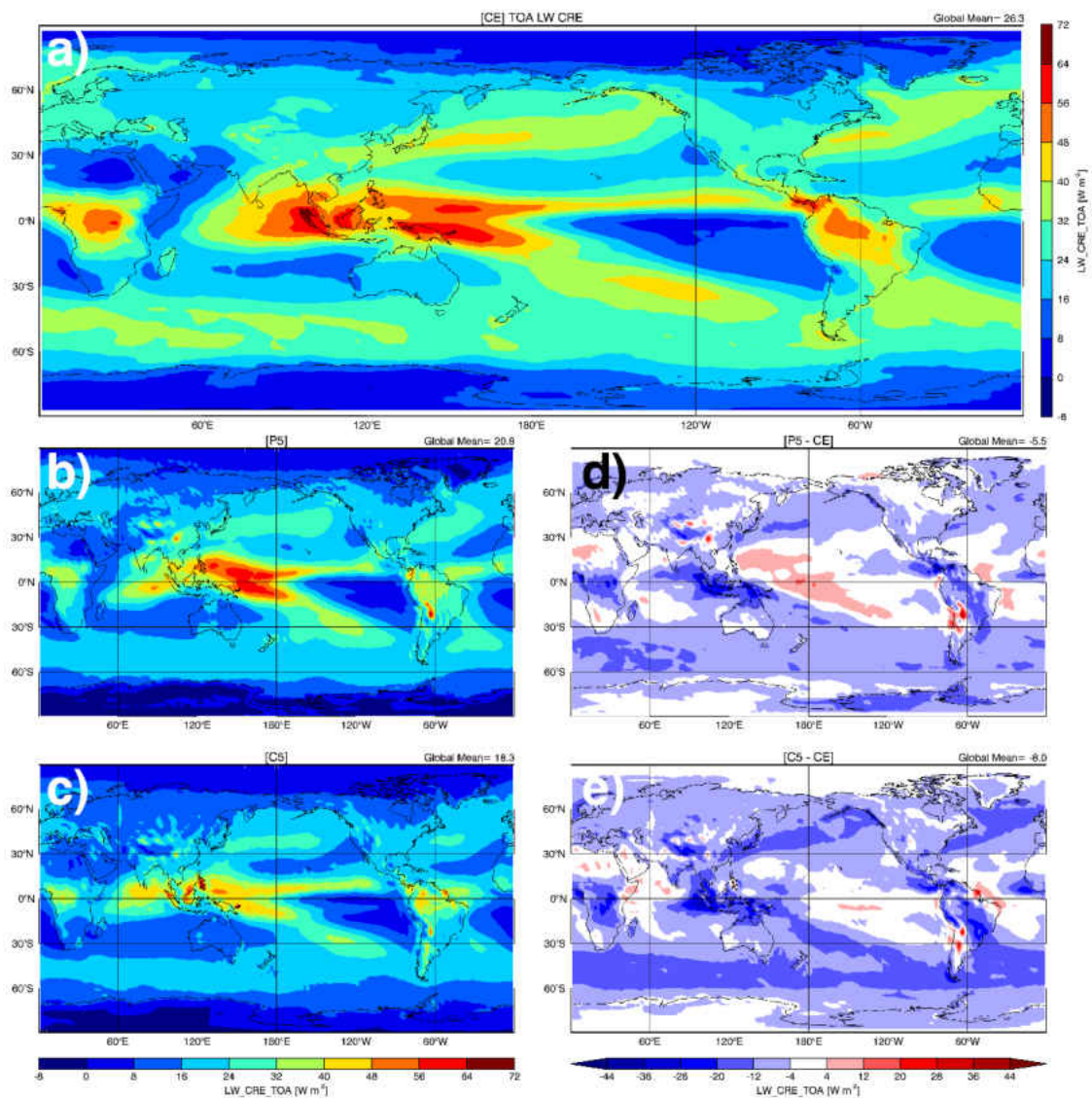
Figure 28. Gridded annual mean clear-sky outgoing longwave radiation (OLR) cloud radiative effect (CRE) at top-of-atmosphere (TOA) derived from (a) NASA CERES-EBAF (CE) results, and simulated by NASA GISS (b) Post-CMIP5 (P5) and (c) CMIP5 (C5) simulations, as well as their differences (d) P5-CE and (e) C5-CE, for the period of March 2000 through December 2005.

For SW CRE (Fig. 29), PWV does not play as important of a role as clouds (Dong et al. 2006). In contrast to the warming effect on the TOA LW radiation budget, clouds have a strong cooling effect on the TOA SW radiation budget, particularly low-level clouds, with a global average of -47.2 W m^{-2} based on CE observations. Although both

78

the P5 and C5 global averages agree with the observation within ~1 W m^{-2}, large differences occur regionally. The global distributions of P5-CE and C5-CE SW CREs have demonstrated that the C5-simulated SW CREs tend to have larger regional differences than the P5 simulation when compared to the CE observations. For instance, as discussed in Chapter IV, the MBL CFs simulated by P5 have increased by ~20% compared to the C5 simulations over the SMLs. This increase brings the P5-simulated MBL clouds over the SMLs much closer to CM observations (Fig. 2e), which results in a much better agreement in SW CRE between the P5 simulation and CE observations over the SMLs. On the opposite side, large positive biases exist in C5 simulations due to large negative biases in C5-simulated MBL clouds over the SMLs (Fig. 2f). The SW and LW CREs over the polar regions should be used with caution given the highly reflective snow-ice surfaces common in these regions, where surface albedos are close to, if not higher than, cloud albedos (Dong et al. 2010).
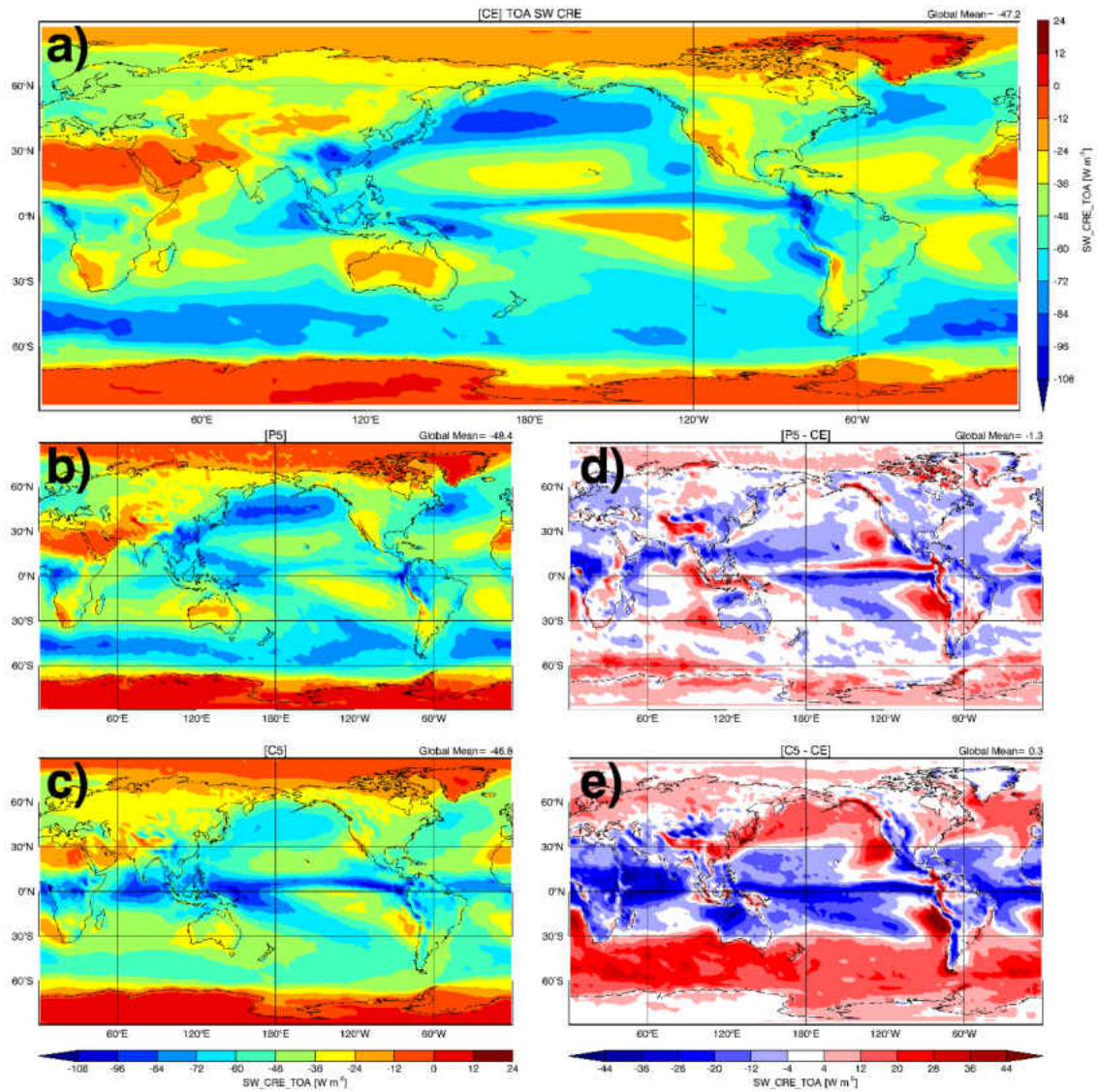
Figure 29. As in Fig. 28, except for SW CRE.

Net CRE, shown in Fig. 30, is defined as the sum of LW and SW CREs and tends to be dominated by the SW cooling effect. The globally averaged net CREs are −20.9 W m^{-2}, −27.7 W m^{-2}, and −28.5 W m^{-2} from CE, P5 and C5, respectively, indicating a net cooling effect of clouds on the TOA radiation budget. On a global mean basis, differences in global net CRE appear to be derived from biases in LW CRE. Examining LW, SW, and net CREs on a regional basis again suggests a more complicated

relationship. For example, regions with a high frequency of marine boundary layer (MBL) clouds are typically associated with large-scale atmospheric downwelling motion (Dong et al. 2014), such as off the western coast of the United States or South America. Here, both P5 and C5 tend to overestimate net CRE because the oversimulation of SW CRE outweighs the undersimulation of LW CRE. Over the SMLs, the P5-simulated SW CREs are closer to the CE observations due to the increase of MBL clouds within the P5 simulation, however, LW CRF is underestimated which results in an undersimulation of net CRE over the SMLs.
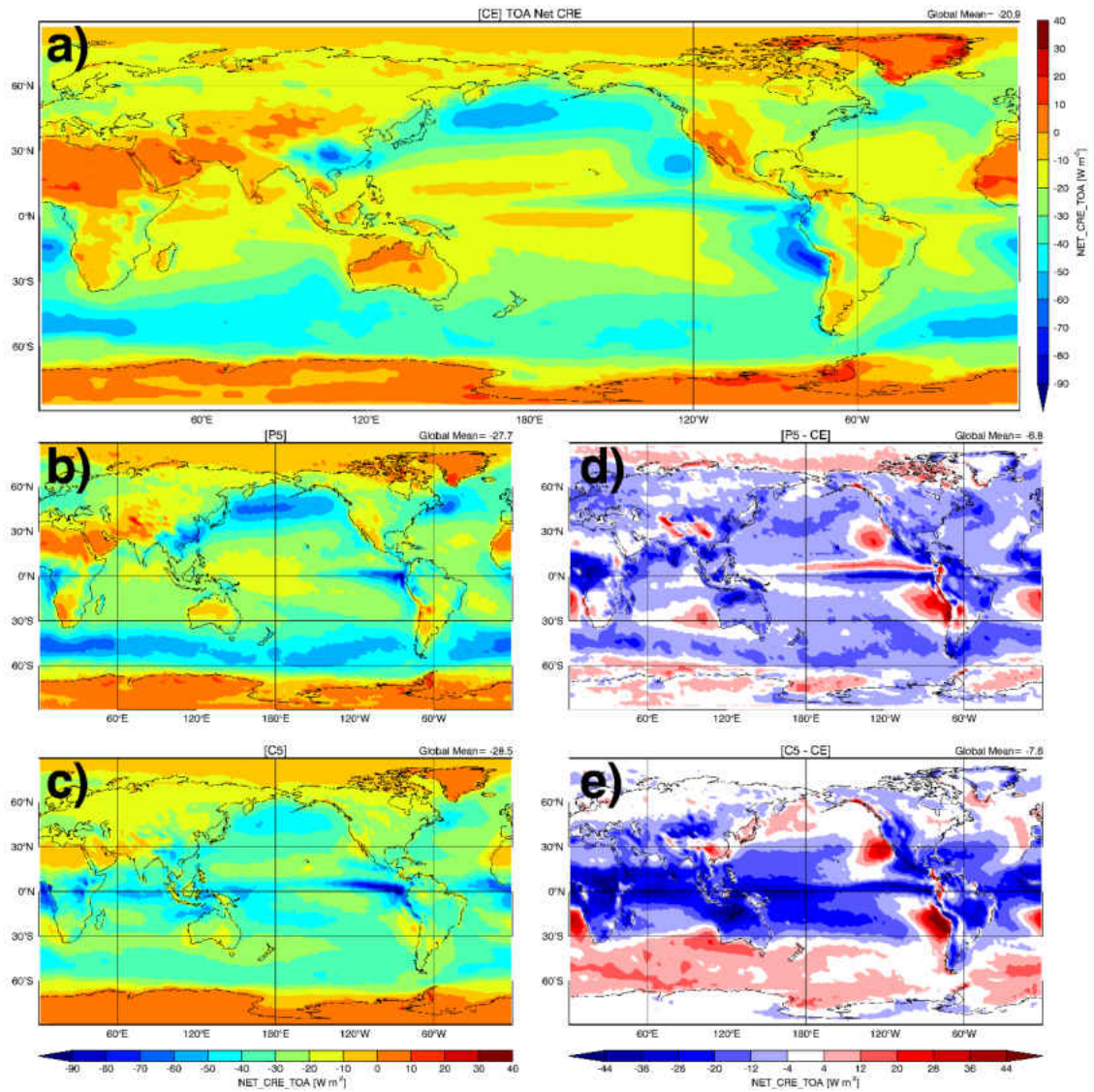
Figure 30. As in Fig. 28, except for NET CRE.

To investigate the impact of cloud fraction (CF) and cloud water path (CWP) on CREs, we plot the zonal means of LW, SW, and net CREs, as well as CF and CWP from Stanfield et al. (2014) in Figure 31. The focus of this section will be shifted away from the SMLs, and will instead be focused more on the tropics. Over the tropics, the P5 and C5-simulated CFs agree well with CM observations, while their CWPs are much higher than CM. The clear-sky OLR is primarily determined by surface temperature, sea-surface

temperature (SST), and atmospheric PWV, while determinations of all-sky OLR are largely affected by cloud-top temperatures, particularly in overcast conditions or in the presence of opaque clouds. In the tropics, this is in part due to the high number of deep convective clouds which have cold cloud-top temperatures (~220 K, Dong et al. 2008). Therefore, the LW CREs ($OLR_{clear} - OLR_{all}$) associated with these clouds should be large and predominately determined by CFs, not CWP, given that most deep convective clouds are optically thick clouds (Dong et al. 2008). Given the good agreement in CF comparison and ignoring the differences in clear-sky OLR between P5/C5 and CM/CE, the LW CREs from these three datasets should be close to each other over the tropics. The much higher CWPs found in P5 and C5 simulations, however, do have an impact on their TOA SW albedos, resulting in a much stronger cooling effect on the TOA SW radiation budget, with more obvious effects in the C5 simulation. Net CRE zonal variations (Figure 31e) essentially follow the variations of their corresponding SW CREs with slight modifications based on their corresponding LW CREs.
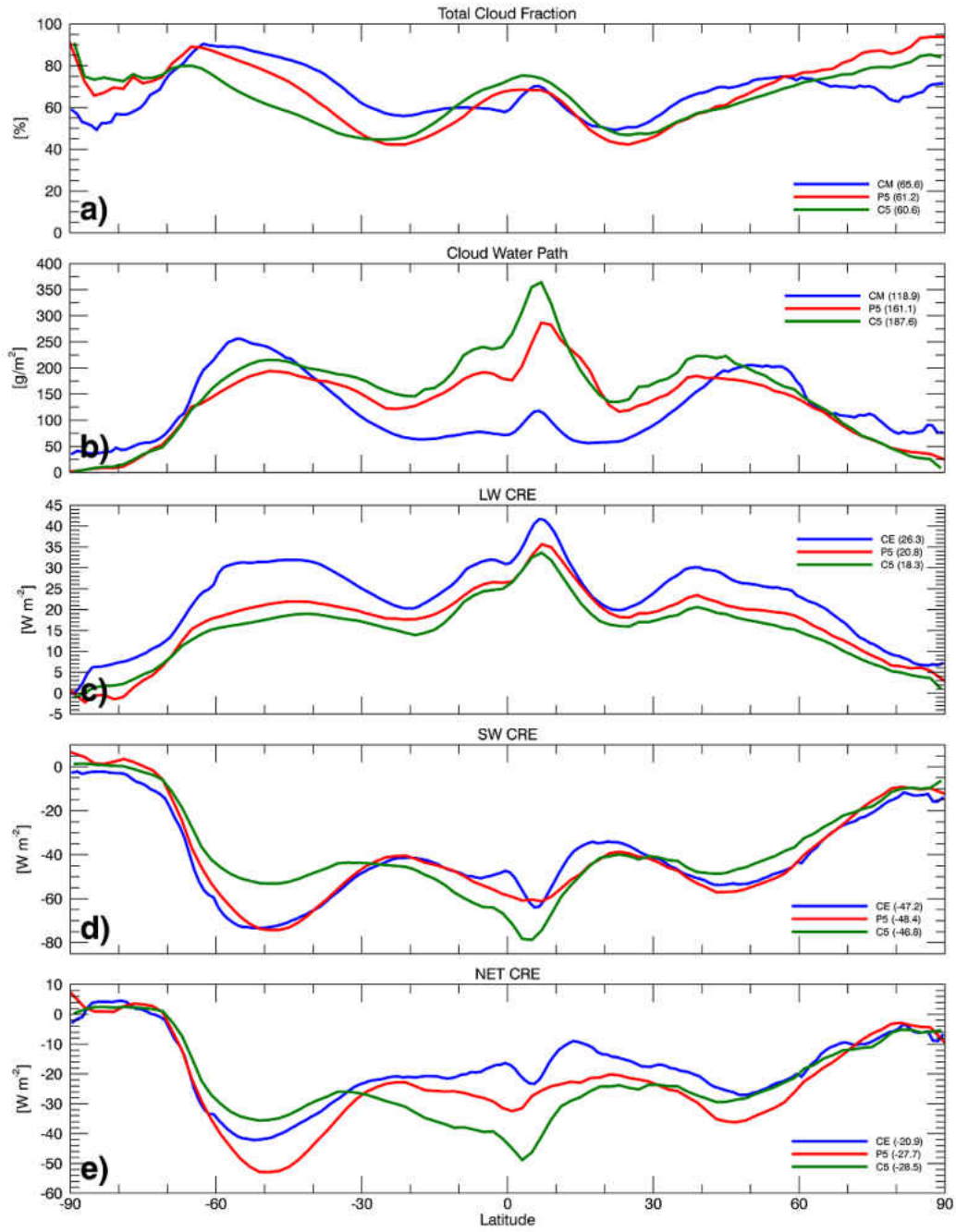
Figure 31. Zonally averaged (a) cloud fraction, (b) cloud water path, (c) LW, (d) SW, and
(e) NET CREs for CE (blue), P5 (red), and C5 (green).

5.1.4 Regional Analysis over Downwelling (DW) / Upwelling (UW) Regimes and the SMLs

It has been shown in previous studies (e.g., Su et al. 2013) that model biases can be highly dependent on their dynamic regimes. For example, vertical pressure velocity (ω) at 500 hPa has been widely used as a proxy to examine model errors in regions of large-scale upwelling (UW, $\omega < 0$) and downwelling (DW, $\omega > 0$) motion (Bony and Dufresne 2005). To define these regimes, simulated fields of ω at or near 500 hPa, over the oceans, are shown in hPa per day for the P5 and C5 simulations in Fig. 32. Although their global patterns are similar to each other, the P5 results tend to be slightly stronger and more wide-spread than its C5 counterpart over both the UW and DW regimes. For this study, we analyze the cloud and radiative properties over regions of strong monthly-averaged large-scale UW motion ($\omega < -25$ hPa per day) and DW motion ($\omega > 25$ hPa per day) within the tropics and subtropics ($\pm 40°$ latitude, Dolinar et al. 2014).
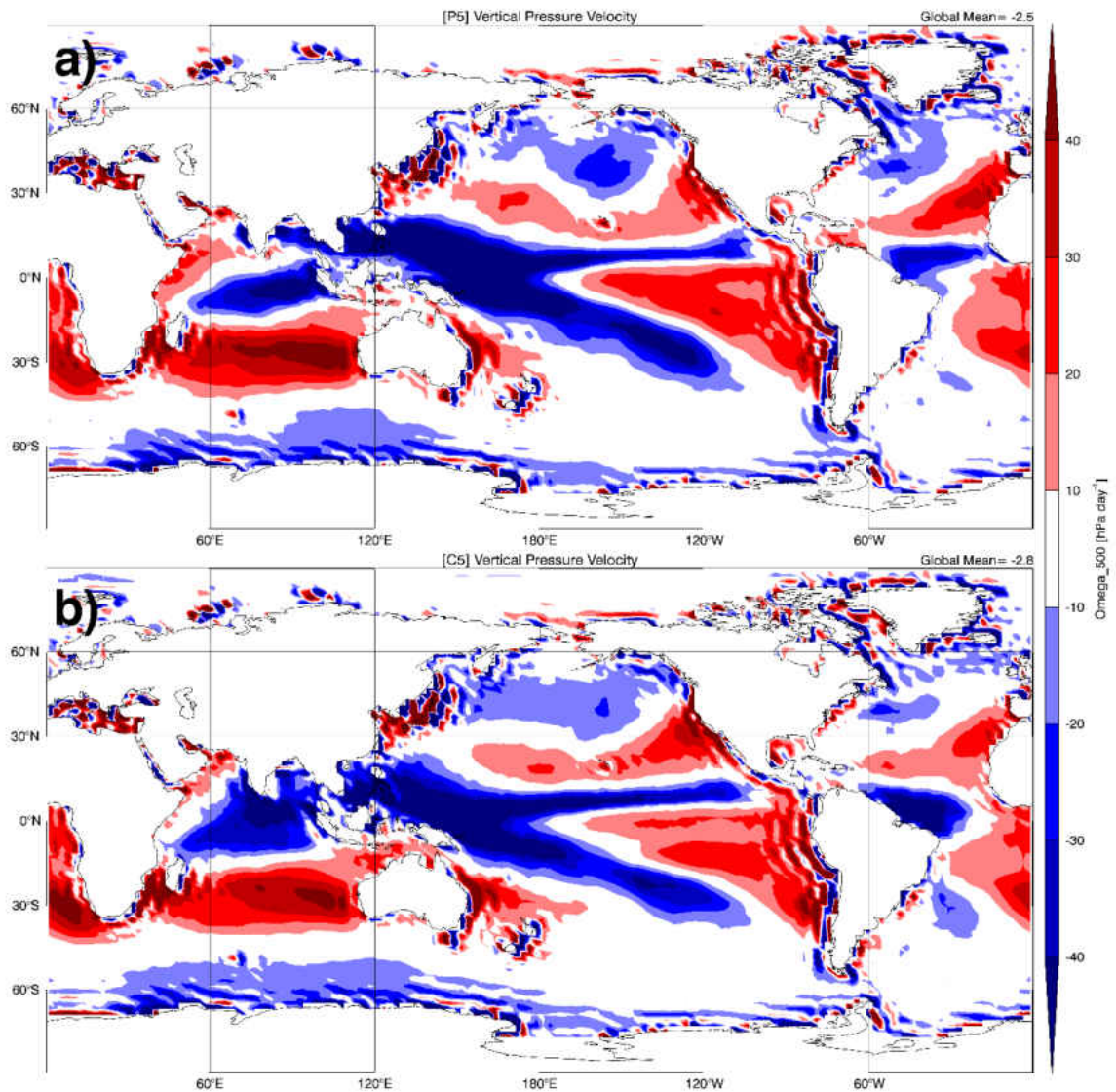
Figure 32. Global maps of averaged vertical pressure velocity (ω) in hPa per day, taken at the layer closest to 500 hPa, for the P5 (top panel) and C5 (bottom panel) simulation. Negative values indicate regions of upwelling motion, while positive values indicated regions of downwelling motion. In this study, regions of strong atmospheric upwelling (ω < −25 hPa per day at 500 hPa) and downwelling (ω > 25 hPa per day at 500 hPa) have been selected to explore the regional differences between model simulations and observations.

Having defined both UW and DW regimes, we compared the P5- and C5-simulated total column CFs, CWPs, and all-sky albedos over these two regimes with CERES-MODIS SYN1 and CERES-EBAF observations (CM and CE). Compared to the CM observed CFs, the P5-simulated CFs outperform the previous C5 results in both UW (Fig. 33a) and DW (Fig. 33b) regimes, having higher spatial correlations and lower mean differences. Figs. 33a and 33b show that both P5 and C5 oversimulate CF in regions of large-scale upwelling motion while undersimulating CF in regions of downwelling motion. P5- and C5-simulated CWPs are shown to be biased roughly 2 to 4 times greater than CM observations within the defined UW regime, resulting in a low spatial correlation, large mean deviation, and large RMSE. In comparison, the changes made to the new P5 parameterizations serve to further increase this bias. Within the DW regime, both P5- and C5-simulated results agree reasonably well with the CM observations, showing moderate correlations (0.67 and 0.53) and small RMSEs (~43 g m^{-2} and 55 g m^{-2}). The P5 simulation shows improved spatial correlation and decreased RMSE compared to its C5 counterpart in CWP over the DW regime. All-sky albedo comparisons across both UW and DW regimes are similar to our previous CF comparisons. More specifically, the P5-simulated all-sky albedos show slight improvement within the UW regime (Fig. 33e) while showing significant improvement within the DW regime, where the correlation to CE observations increased from 0.40 to 0.78 (Fig. 33f).
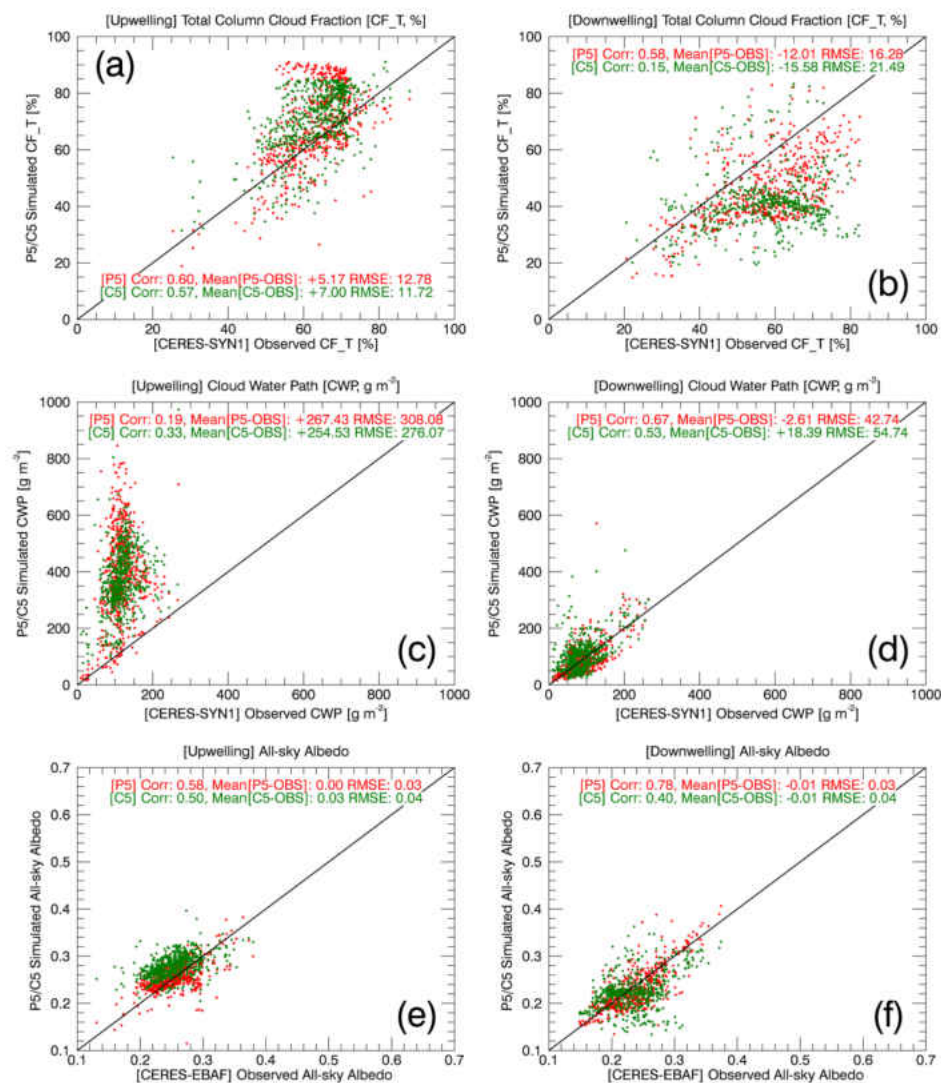
Figure 33. Scatterplots of P5/C5 simulated total column cloud fraction (a,b), cloud water path (c,d), and TOA all-sky albedo (e,f) against CERES observations over defined regions of strong large-scale upwelling (left column) and downwelling (right column) vertical motion. The black line represents a perfect 1:1 correlation. Values of spatial correlation, mean difference between each model simulation and the observations, and RMSE are presented within each figure.

In summation, although the all-sky albedos simulated by both P5 and C5 are close to the CE observations within the UW regime, both the P5 and C5 simulations moderately overestimate total column CF while drastically oversimulating CWP. Within the DW regime, both the P5- and C5-simulated all-sky albedos and CWPs agree well with the CERES observations, however, their simulated total column CFs are lower (~14%) than the observations. Although the differences in all-sky albedo between the P5/C5 simulations and CERES observations in both regimes are small, they are not well correlated with the corresponding CF and CWP comparisons. All-sky albedos depend primarily on both CF and CWP. As such all-sky albedo comparisons are expected to be consistent, or complementary, with CF and CWP comparisons, such as lower/higher CF and larger/smaller CWP, respectively. However, all-sky albedo comparisons within the UW regime do not make sense, physically, when the agreement found in all-sky albedo (Figure 33e) is a result of similar biases in both CF (Figure 33a) and CWP (Figure 33c). Further study within the defined DW regime has revealed that while total column CF is ~14% lower than the CERES observations, the good agreements found in all-sky albedo and CWP comparisons can be explained from an increase in highly reflective low-level CF (pressure > 660 hPa, ~10%), and decreases in mid- (660 hPa < pressure < 440 hPa, ~1%) and high-level CFs (pressure < 440 hPa, ~6%) (multi-level CFs not shown here).

High-level CF (pressure < 440 hPa), PWV, and all-sky OLR comparisons over the UW and DW regimes are shown in Figure 34. Both the P5- and C5-simulated PWVs have an excellent agreement with the AMSR-E observations, with nearly perfect correlations over both regimes. An increase of ~ 2 g m^{-2} is noted in the P5 simulation when compared to C5, which matches the ~ 2 g m^{-2} increase in global mean PWV shown

in Stanfield et al. (2014). This increase in P5-simulated PWV is predominately due to the increase in rain evaporation from the new cumulus parameterization. All-sky OLR biases agree well with the high-level CF comparisons. For example, both the P5- and C5- simulated upper-level CFs are ~11% higher than CERES observations, while both the P5- and C5-simulated all-sky OLRs are ~2.5 W m^{-2} lower than observations within the UW regime due to high-level cloud tops having a much colder temperature than the sea surface. This argument is also true within the DW regime, where the C5-simulated high-level CF is 9.25% higher and all-sky OLR is 1.76 W m^{-2} lower than the CERES observations. P5 shows particularly good agreement in simulated high-level CF and all-sky OLR when compared with CERES observations within the defined DW regime. In general, the P5 simulation shows more improvement within the DW regime, where mean biases and RMSEs have decreased moderately compared to previous C5 results.
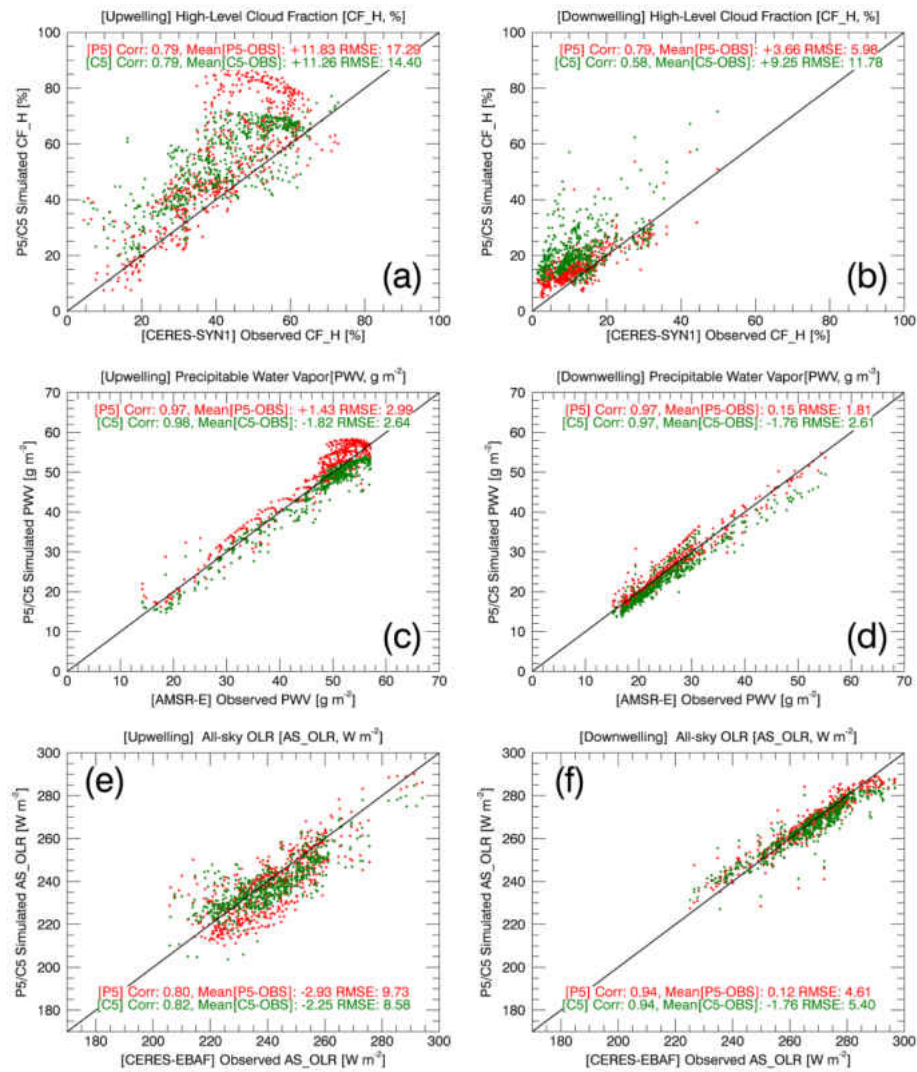
Figure 34. As in Figure 33, except for high-level cloud fraction (a,b, pressure < 440 hPa), precipitable water vapor (c,d), and all-sky OLR (e,f).

In Stanfield et al. (2014), a quantitative comparison was performed to assess the improvement in the P5-simulated CF and cloud properties over the SMLs. To further investigate the impact of these improved cloud properties on the TOA radiation budget, we again focus on the SMLs using the data presented in Figure 35. Through this comprehensive analysis, it is our hope that the modeling community may benefit from the

modified planetary boundary layer (PBL) scheme implemented within the new GISS-E2 P5 GCM simulation, as many of the GCMs undersimulate MBL clouds over the SMLs when compared to the CERES observations (Dolinar et al. 2014).

As discussed in Stanfield et al. (2014) and presented here in Figure 35, the P5-simulated total column CF increased ~12% over the SMLs compared to its C5 predecessor (Figure 35a), largely as a result of the newly modified PBL scheme and the associated ~18% increase in low-level MBL clouds (Figure 35b). This increase in total column CF from enhanced MBL clouds has out-performed the underestimation of CWP in the SMLs (Fig. 35c), resulting in a ~6% increase in all-sky albedo compared to the previous C5 simulation (Fig. 35e). While it does not make physical sense to have higher albedo with lower CF and CWP compared to the observations, this result may be partially explained by the ~20% increase in P5-simulated MBL clouds. Note that comparisons of MBL CF should be used with caution as passive satellites often cannot observe low-level clouds if there is an optically thick cloud layer above it. PWV and all-sky OLR comparisons (Figs. 35e&f) are similar to those in the defined DW regime, with slight improvements found in the P5 simulation. Minimal changes are observed in all-sky OLR fields over the SMLs (Fig. 35f), as there is no significant difference between MBL cloud-top temperature and SST. Based on the results presented here and findings of Stanfield et al. (2015), the largest improvements are found in the P5-simulated all-sky SW absorption, albedo, and SW CRE fields in response to the increase in MBL CF.
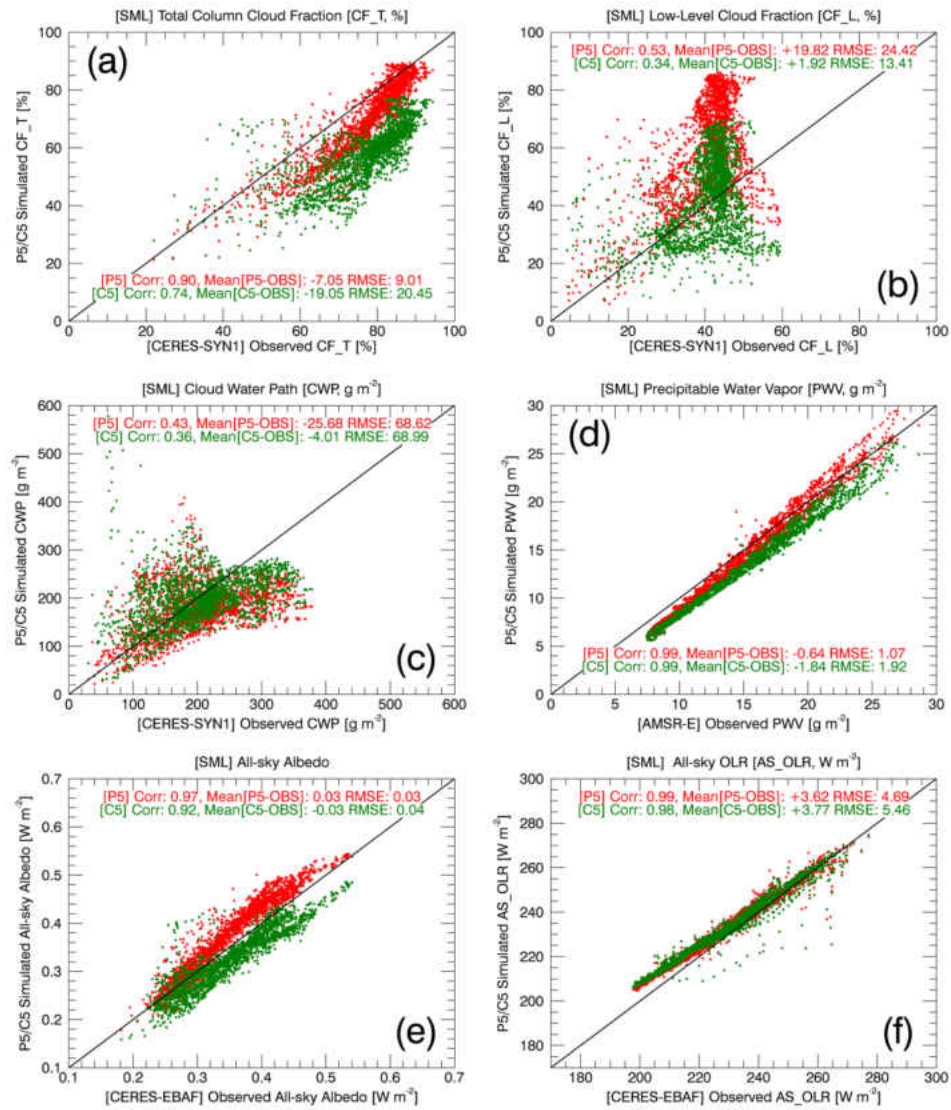
Figure 35. Scatterplots of total column cloud fraction CF (a), low-level cloud fraction (b, pressure > 660 hPa), cloud water path CWP (c), precipitable water vapor PWV (d), all-sky albedo (e), and all-sky OLR (f) over the SMLs (30° S < latitude < 60° S).

5.2 Update to Stanfield et al. (2015)

Radiative products in the E5 GCM simulation were not provided at the time of this study. As such, insights into radiative fields simulated by the E5 version of the GCM are left to speculation. Vertical CF results in Chapter IV have shown a decrease in average cloud height within the E5 GCM model which will heavily influence both SW and LW fluxes. It is hypothesized that these changes bring the model back into global radiative balance, as IWC, LWC, and CFs decrease globally, on average, in the E5 simulation compared to previous C5 and P5 simulations. Future work should include examination into both TOA and surface radiative fields.

5.3 Summary of Radiation Properties

NASA GISS CMIP5 (C5) and Post-CMIP5 (P5) simulated TOA radiation budgets and Cloud Radiative Effects (CREs) were assessed utilizing the observed CERES EBAF (CE) radiation products, with a particular focus on large-scale atmospheric upwelling and downwelling regimes, the southern mid-latitudes, and marine stratocumulus regions. Based on multiyear comparisons of the P5 and C5 versions of the GISS E2 GCM against the CE observations, the following conclusions have been made:

1) Overall, the P5- and C5-simulated global patterns of clear-sky outgoing longwave radiation (OLR) match well with CE observations. Global averages of the P5- and C5-simulated clear-sky OLRs are ~4 and ~8 W m^{-2}, respectively, lower than the CE observation (266.1 W m^{-2}). These biases are partially due to the dry bias issue of comparing simulated clear-sky OLRs with observations, however this cannot explain the full bias found. Regional

analysis of the biases in all-sky OLR revealed strong correlations to both PWV and total column CF. Further study has revealed that LW CREs also have strong correlations with PWV and total column CFs, thus it is concluded that clouds and PWV play major roles in calculating LW CRE.

2) Global means of clear-sky and all-sky albedo were found to be nearly identical between all three datasets. On a regional scale, however, large biases are found in all-sky albedo. As discussed in Part I, the MBL cloud fractions over the SMLs increased ~20% in the P5 simulation compared to its C5 predecessor, due to the implementation of the new PBL scheme. This increase in MBL CF over the SMLs has resulted in increased all-sky albedo and decreased SW absorption at TOA in the P5 simulation.

3) Analyses of spatial variability using the Taylor diagram showed large improvements in correlations of simulated SW and Net CRE, with an insignificant sacrifice in variability. LW CRE correlations between the models and CE observations remained static; however, improvements were found in the LW CRE variability. P5/C5 correlation and variability comparisons continue to show good agreement with CE observations for all other variables, which is expected given the already high agreement found when comparing previous model simulations with CE observations.

4) To explore the regional differences between the model simulations and the observations, we define regions of large-scale vertical ascent/descent using vertical pressure velocity (ω) as a proxy. Regimes of strong atmospheric upwelling (UW, $\omega < -25$ hPa per day) and downwelling (DW, $\omega > 25$ hPa per

day) are identified. Although the differences in all-sky albedo between the P5/C5 simulations and CERES observations in both regimes are small, they are not well correlated with the CF and CWP comparisons. PWV amounts simulated by both P5 and C5 have an excellent agreement with the AMSR-E observations, with nearly perfect pattern correlations over UW and DW regimes. All-sky OLR biases agree well with high-level CF comparisons. In general, the P5 simulation shows more improvement within the DW regime, where mean biases and RMSEs have decreased moderately compared to previous C5 results.

Overall, minimal changes were observed between the P5 and C5 simulations when looking at various fields during clear-sky scenes. With the adjustments to turbulence (Yao and Cheng 2012) and moist convection (Del Genio et al. 2012), large changes, however, are observed regionally during all-sky scenes. These changes come predominately in the form of improvements compared to CE observations, with particular attention to the SMLs. A second quantitative comparison over the SMLs was performed and has validated the improvements found in Stanfield et al. (2014). Changes to low-level and total column CFs and cloud properties, resulting from changes to the P5 PBL parameterization, have shown great improvement across almost all radiative variables presented in Chapter V of this study. The strongest improvements in the SMLs have been found in SW fields during all-sky conditions, where increased CF in the P5 simulation has led to increased reflected shortwave flux and a higher albedo.

Vertical CF results in Chapter IV have shown a decrease in average cloud height within the E5 GCM model which will heavily influence both SW and LW fluxes. It is

hypothesized that these changes bring the model back into global radiative balance, as IWC, LWC, and CFs decrease globally, on average, in the E5 simulation compared to previous C5 and P5 simulations.

CHAPTER VI

NORTH PACIFIC ITCZ PRECIPITATION

This chapter details the precipitation analysis discussed in Stanfield et al. (2016), and examines how new modifications in the NASA GISS ModelE GCM have impacted precipitation fields in the model.

6.1 Stanfield et al. (2016) – Precipitation Analysis of 29 CMIP5 AMIP GCM Simulations

The goal of Stanfield et al. (2016) was to provide an accurate assessment of regional precipitation simulated by the AMIP (Atmosphere Model Intercomparison Project) GCM experiment under the Earth System Grid Federation (ESGF) Program for Climate Model Diagnosis and Intercomparison (PCMDI; Taylor et al. 2012). AMIP simulation runs use prescribed sea-surface temperatures, which eliminate potential biases caused by the coupled ocean models of the GCMs. Precipitation from 29 GCM AMIP simulations (Table 8) were thoroughly compared with GPCP (Adler et al. 2003) and TRMM (Huffman and Bolvin 2011) precipitation products, as well as with their linked CMIP5 historical ocean-coupled runs. In this study, an algorithm has been developed to define the North Pacific ITCZ through several metrics with the intent of quantifying magnitude-, location-, and width-based biases within the GCMs. The ITCZ is a major feature component of the global circulation, and serves as a good metric for testing the GCMs. These metrics are quantitatively examined using the observations as the ground truth.

Table 8. Summary of the 29 GCMs used in Stanfield et al. (2016), along with their spatial resolution (longitude × latitude). Models across from each other (horizontally) are considered to be linked when comparing historical and AMIP simulated precipitation.

#	AMIP Model	Resolution	Linked Historical Model
1	ACCESS 1-0	1.875 x 1.25	ACCESS1-0
2	ACCESS 1-3	1.875 x 1.25	ACCESS1-3
3	BCC-CSM1-1	2.8125 x 2.8125	BCC-CSM1-1
4	BCC-CSM1-1-m	1.25 x 1.25	BCC-CSM1-1-m
5	BNU-ESM	2.8125 x 2.8125	BNU-ESM
6	CCSM4	1.25 x 0.9375	CCSM4
7	CESM1-CAM5	1.25 x 0.9375	CESM1-CAM5
8	CMCC-CM	0.75 x 0.75	CMCC-CM
9	CNRM-CM5	1.4 x 1.4	CNRM-CM5
10	CSIRO-Mk3-6-0	1.875 x 1.875	CSIRO-Mk3-6-0
11	CanAM4	2.8125 x 2.8125	CanCM4
12	FGOALS-g2	2.815 x 3	FGOALS-g2
13	FGOALS-s2	2.815 x 1.666	FGOALS-g2
14	GFDL-AM3	2.5 x 2	GFDL-CM3
15	GFDL-HIRAM-C180	0.625 x 0.5	-
16	GFDL-HIRAM-C360	0.3125 x 0.25	-
17	GISS-E2-R	2.5 x 2	-
18	HadGEM2-A	1.875 x 1.25	-
19	INM-CM4	2 x 1.5	-
20	IPSL-CM5A-LR	3.75 x 1.875	IPSL-CM5A-LR
21	IPSL-CM5A-MR	2.5 x 1.25	-
22	IPSL-CM5B-LR	3.75 x 1.875	IPSL-CM5B-LR
23	MIROC5	1.4 x 1.4	MIROC5
24	MPI-ESM-LR	1.875 x 1.875	MPI-ESM-LR
25	MPI-ESM-MR	1.875 x 1.875	-
26	MRI-AGCM3-2H	0.5625 x 0.5625	-
27	MRI-AGCM3-2S	0.1875 x 0.1875	-
28	MRI-AGCM3	1.125 x 1.125	MRI-CGCM3
29	NorESM1-M	2.5 x 1.8947	NorESM1-M

6.1.1 Methodology

This section details the selection of the area of focus (AOF) in Stanfield et al. (2016) and provides an in-depth discussion on how the algorithm developed in Stanfield et al. (2016) defines the ITCZ and thus pulls various metrics on the ITCZ based on this definition.

6.1.1.1 Defining the Area of Focus (AOF) for the ITCZ

In the IPCC AR5, it was concluded that the GCMs in CMIP5 contain systematic errors in the tropics (IPCC AR5 Ch.9; Flato et al. 2013). To examine these systematic errors, modeled area-weighted mean precipitation is compared within the tropics and subtropics (±40° latitude) with GPCP and TRMM results. Figure 36 shows that all 29 of the GCM simulations examined in this study oversimulate precipitation compared to both GPCP and TRMM precipitation products between ±40° of latitude both annually and seasonally. The annual mean precipitation from the GCM ensemble is ~13% greater than both GPCP and TRMM results (~3 mm/day), with the GCMs ranging from 3.11 mm/day (IPSL-CM5A) to 3.73 mm/day (INM-CM4). No strong seasonal variation is observed.

Comparisons of annual mean precipitation between the GPCP, TRMM, and the GCM ensemble over ±40° latitude for the 6-yr study period are shown in Fig. 37. This comparison shows that the ensemble mean precipitation of GCMs is higher than both GPCP and TRMM observations, particularly in large-scale ascent regions, such as the North Pacific ITCZ.
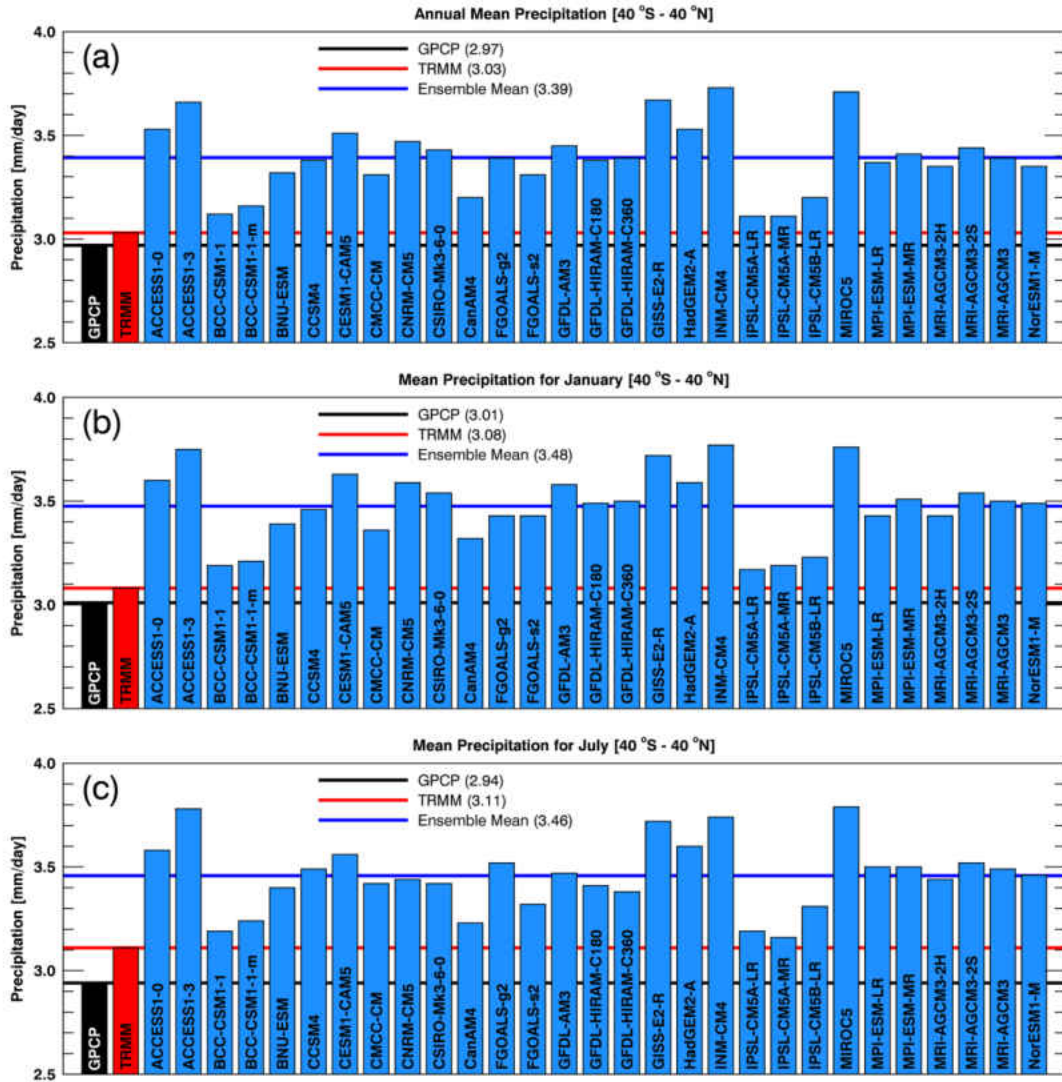
Figure 36. Comparisons of area-weighted mean precipitation (a) annually, in (b) January, and in (C) July between GPCP (black) and TRMM (red) observations and 29 GCM simulations used in this study over tropical and sub-tropical regions (±40° latitude). The black/red lines each represent the mean of GPCP/TRMM observations, respectively, while the blue line represents the GCM ensemble mean. All results are calculated over the full study period, January 2000 to December 2005.

101
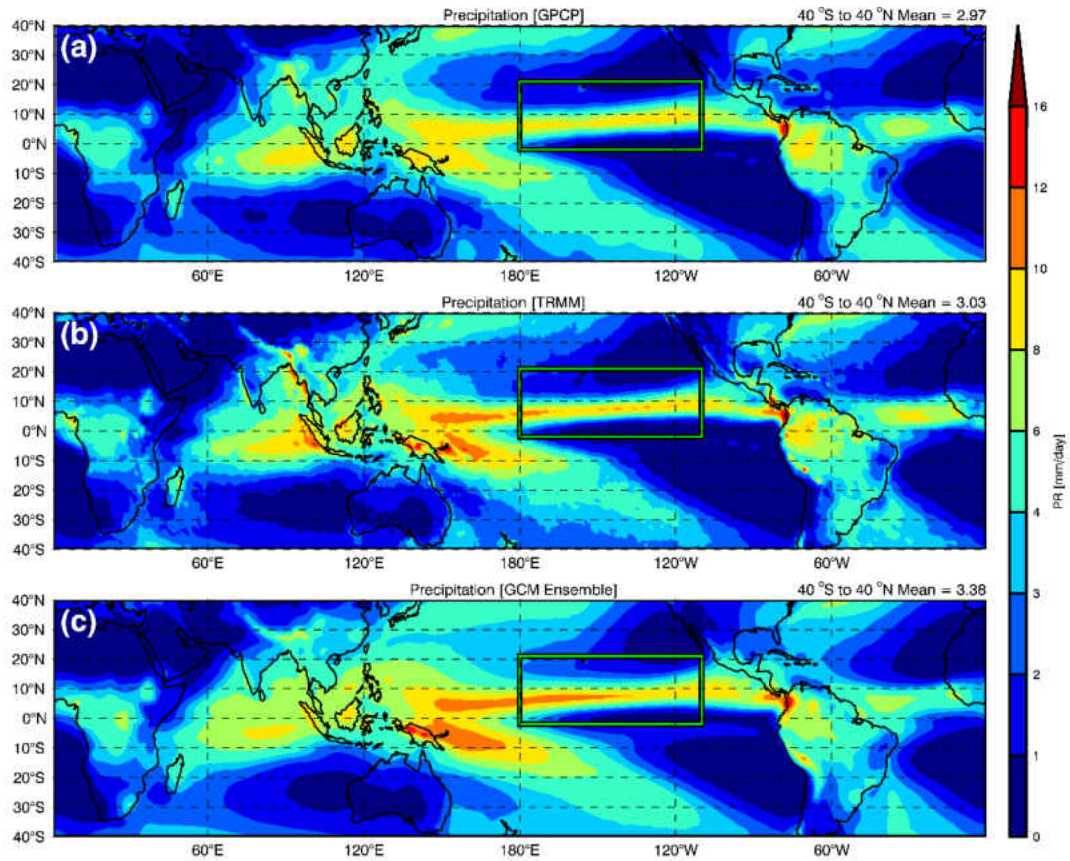
Figure 37. Annually averaged regional mean precipitation over ±40° latitudes from (a) GPCP and (b) TRMM observations and (c) the GCM Ensemble mean during the 6-yr study period. The annual area-weighted means for each dataset are shown on the upper right corner of the image. The green box in each image represents the Area Of Focus (AOF): 2° S to 21° N and 180° W to 110° W, defined in this study.

To make proper comparisons between the GCM simulations and observations, an area of focus (AOF) has been defined by the boundaries 2° S to 21° N and 180° W to 110° W in this study. The selected AOF covers the full breadth of the ITCZ across all seasons as demonstrated using GPCP and TRMM observations in Fig. 38. With the AOF defined by these boundaries, we cover most of the precipitation simulated by the GCMs while also limiting exposure to exterior regional biases. These biases include spurious precipitation cells that occur north of the Pacific ITCZ in some GCMs which are strong

enough to potentially distract the algorithm from properly identifying the ITCZ as well as potential land effects found outside of the eastern and western edges of the AOF.
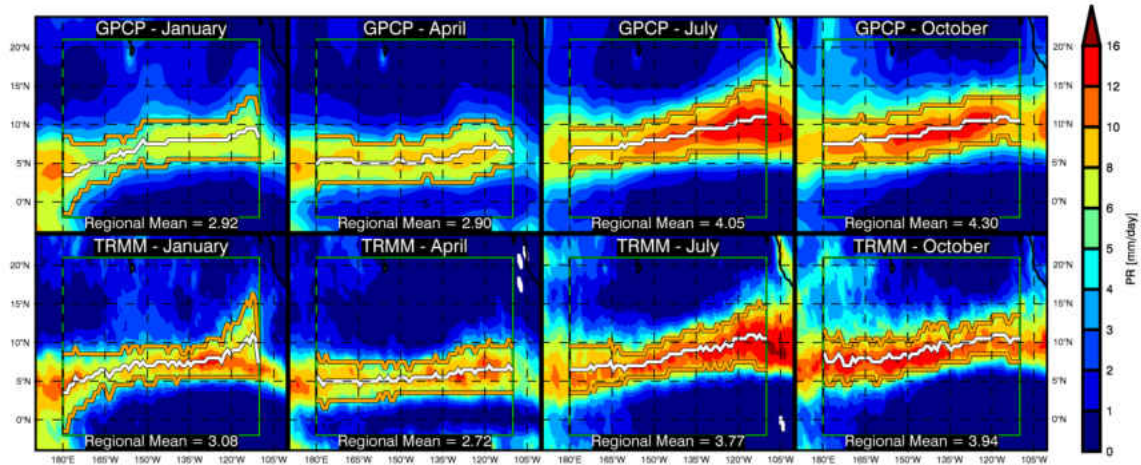
Figure 38. Seasonal precipitation in the Pacific ITCZ from GPCP and TRMM observations. The green box in each image represents the AOF (2° S to 21° N and 180° W to 110° W) defined in this study. The regional mean represents the average amount of seasonal precipitation within the AOF for the respective month during the 6-yr study period.

6.1.1.2 Regridding of Precipitation and Sensitivity Study

Given the varying resolutions of the GCMs and the GPCP and TRMM data products, all precipitation fields were interpolated to a standardized grid during comparisons to equally and objectively compare the performance of each GCM. A sensitivity test was performed to examine the connection between the sizing of the standardized grid and derived ITCZ metrics based on the chosen grid. It was concluded that standardized 1° × 1° (latitude × longitude) grid was sufficient. To minimize bias due to smoothing, all observational fields have been interpolated twice; once from their native

resolution to the spatial resolution of each GCM grid, and then a second time to convert back to the standardized 1° × 1° (latitude × longitude) grid during comparisons.

6.1.1.3 Defining the ITCZ and ITCZ Metrics

In this study, an algorithm has been developed to analyze and compare the ITCZ simulated by each of the GCMs with collocated observations. The algorithm first outlines the boundaries of the ITCZ, and a variety of metrics are pulled based on these boundaries. An example of output from the algorithm is provided in Figure 39 using monthly averaged precipitation in January simulated by the Australian ACCESS 1-3 GCM. In detail, the algorithm first attempts to identify the upper and lower boundaries of the ITCZ band (orange lines in Fig. 39) across each degree of longitude within the AOF by identifying the longest continuous stretch of precipitation above a set monthly precipitation rate threshold. The monthly thresholds defined in this study vary by month (4 mm/day from January to April, 6 mm/day from May to December). These thresholds were chosen based on our monthly analysis of TRMM and GPCP observations in the ITCZ. As demonstrated in Figure 39, these thresholds can be used to clearly identify the boundaries of the ITCZ.
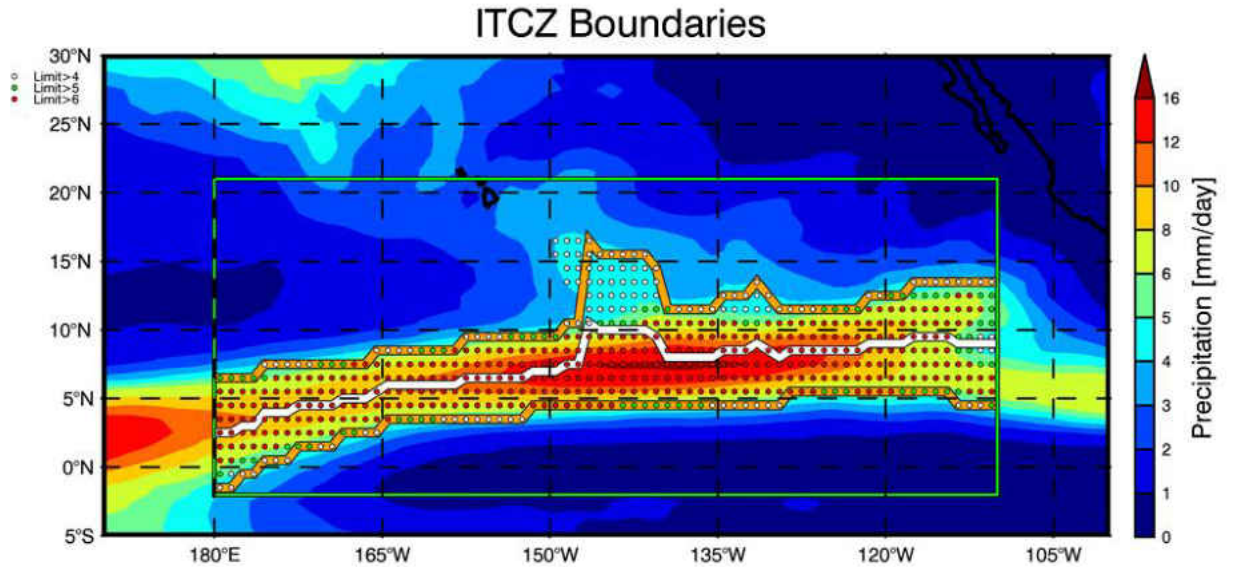
Figure 39. A visual example defining Intertropical Convergence Zone (ITCZ) boundaries within the AOF using monthly data from the Australian Access1-3 GCM in January. The green box is the AOF defined in this study, the orange lines represent the upper and lower boundaries of the ITCZ using the method described, and the white line represents the derived centerline based on upper and lower boundaries. White, green, and red dots indicate a gridded precipitation rate greater than 4, 5, and 6 millimeters per day, respectively.

After defining the upper and lower boundaries, a centerline (white line in Fig. 39) is derived as the midpoint between the upper and lower boundaries at each degree of longitude. When no values were found above the precipitation threshold for a given longitude, the algorithm will either interpolate between the nearest two known points of the ITCZ centerline or extrapolate outward by finding the average slope of the nearest 10 points. The width of the ITCZ, here after referred to as width of the band, is defined as the latitude of the upper ITCZ boundary minus the latitude of the lower ITCZ boundary. When all simulated precipitation rates across a set degree of longitude are below the monthly thresholds, a value of zero is given for the width of the ITCZ at that longitude.

All metrics and comparisons in this study are calculated and shown against both collocated GPCP and TRMM observations. The only exception to this is in the centerline

105

comparisons, where it was found that the centerlines derived from GPCP and TRMM observations predominately deviated by less than 1° of latitude. Therefore, centerline comparisons are conducted by comparing the GCM derived centerlines against the average of the GPCP and TRMM derived centerlines.

To examine the magnitude of simulated precipitation along the ITCZ, we first calculate the average of all points of precipitation within ±4° latitude of the observed centerline for each GCM. These values are then compared to the average magnitude of precipitation observed from both GPCP and TRMM, which are both calculated as the average of all points of precipitation within ±4° latitude of the averaged observed centerline from each observation. The use of four degrees of latitude was chosen during analysis because using this range covered the full visible width of the observed ITCZ each month.

The overall precipitation bias found between the Pacific ITCZ simulated by each GCM and the ITCZ observed by GPCP and TRMM can generally be expressed as a combination of three partitions. These three partitions are shown in Fig. 40 using idealized distributions of precipitation across a set longitudinal line: positional/locational biases, magnitude/intensity biases, and biases in the width of the simulated ITCZ. The algorithm developed in this study is designed to quantitatively estimate the strengths of these biases. These biases can be attributed to the physical parameterizations and dynamic schemes in different GCMs.

Comparisons have been made between CMIP and AMIP simulations using identical parameterizations in each GCM. It should be noted that while precipitation is a diagnostic property within the GCMs, precipitation has a feedback on the large-scale

state, making it difficult to separate the contributions of dynamic schemes and physical parameterizations to precipitation biases.
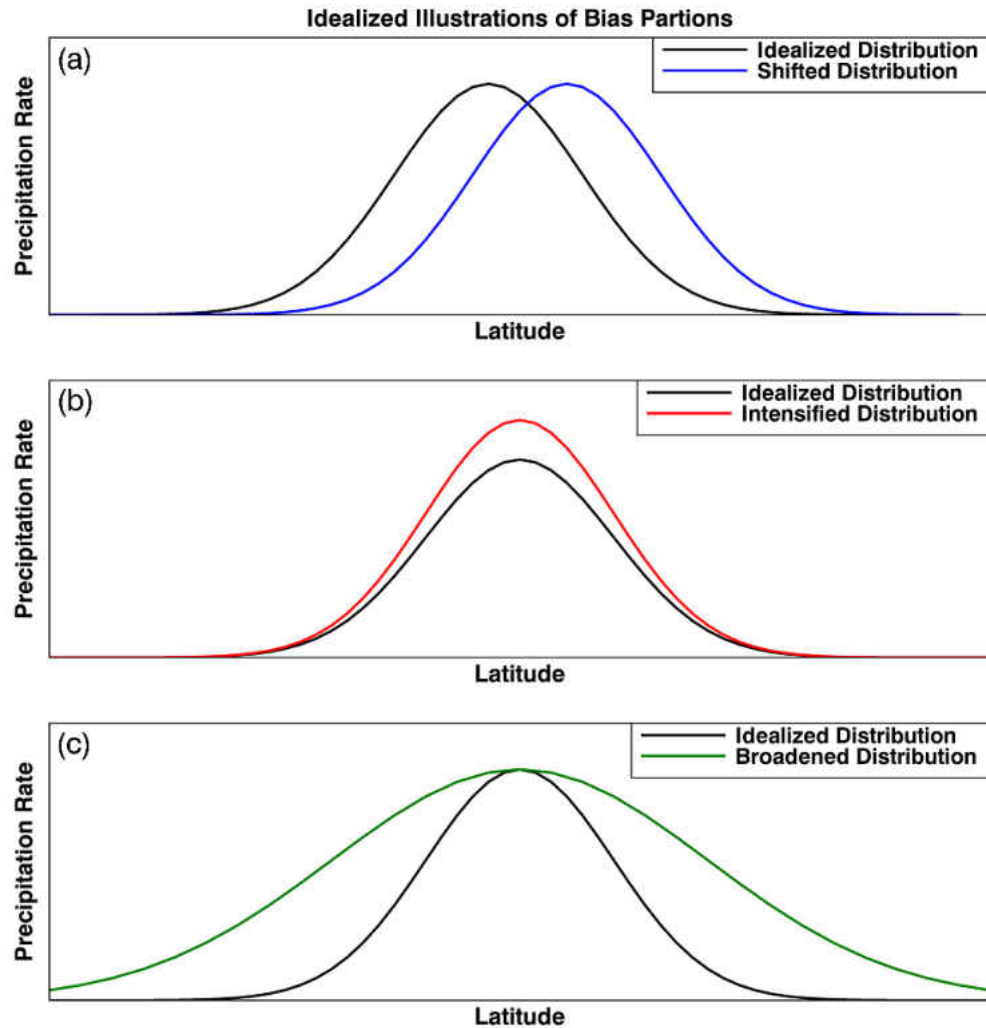
Figure 40. Three idealized examples of potential biases found when comparing GCM simulated (blue, red, or green) and observed (black) precipitation in the ITCZ: (a) location bias shown by a shift northward in the simulated ITCZ, (b) magnitude bias shown as an intensification of precipitation in the simulated ITCZ, and (c) width bias shown as a broadening of the simulated ITCZ, when compared to the observed ITCZ.

The methods used to examine and compare the simulated ITCZs in this study were chosen in an attempt to provide the most balanced and fair comparison between all CMIP5 GCMs. When developing the algorithm used in this study, three difficulties had to be overcome to provide a fair comparison: (1) Missing precipitation, (2) non-Gaussian distributions, and (3) spurious cells North of the ITCZ. For example, a few of the models severely undersimulated precipitation in the ITCZ, thus the west-east precipitation field was not continuous across the AOF. In these circumstances, the centerline of the ITCZ had to be estimated using interpolation or extrapolation based on the known centerline locations. While the observations showed a Gaussian-like distribution across a longitudinal line, many of the GCMs exhibited northerly skewed distributions of precipitation. An attempt was made to use an e-folding technique to identify the boundaries of the ITCZ, however, this attempt was unsuccessful because it could not treat all of the GCMs equally and fairly due to the non-Gaussian distributions of precipitation in many of the GCMs. These skewed distributions also limited our ability to use maximum precipitation as a centerline identifier. Many of the GCMs also showed large patches of high precipitation rates North of the ITCZ, which made it difficult to use a percentage-based system to identify the ITCZ boundaries. Therefore, we have chosen the threshold-based method to derive ITCZ metrics.

6.1.1.4 Description of Barplot Presentation

All barplots shown in Figs. 41 through 43 follow the same overall design. Each month is color coded as shown in the legends. The horizontal black line in each of these figures represents a perfect match with the baseline metric when comparing with the modeled

results. The observations are used as a baseline in Figs. 41 through 43, while CMIP results are used as the baseline in Fig. 44. Monthly values for each of the metrics presented are vertically stacked for each GCM, indicating that monthly values of each metric should be measured as the height of each respective bar for that month only. More specifically, the length of each bar should be compared to the scale length shown on the diagram. Tick marks along the y-axis of match the scale length presented in each figure. To alleviate potential confusion, values on the y-axis of these barplots have been removed, as including values tends to suggest an incorrect cumulative nature.

6.1.2 Centerline and Width of the ITCZ in AMIP Simulations

Figure 41 shows the differences in ITCZ centerline position between each GCM simulation and the averaged centerline of GPCP and TRMM observations. Monthly values above (below) the horizontal black line represent months where the modeled ITCZ centerline of the respective GCM was found to simulate more northward (southward) compared to the averaged centerline of GPCP and TRMM observations. Note that monthly values in Figure 41 are vertically stacked for each GCM, with a tick spacing of 2 degrees.

Figure 41 has demonstrated that most of the GCMs tend to simulate the ITCZ centerlines northward compared to GPCP and TRMM observations, with the greatest shifts occurring in March. While most of the GCMs simulate the ITCZ centerlines northward, it is worth noting that both the Chinese BCC-CSM1-1 and the BCC-CSM1-1-m tend to shift the ITCZ centerlines southward compared to the observed centerline. Some models show promise, with low biases or by a balancing of northward and

southward months, such as the ACCESS1-0, ACCESS1-3, CCSM4, CESM-CAM5, CanAM4, HadGem2-A, and the MRI-AGCM3.
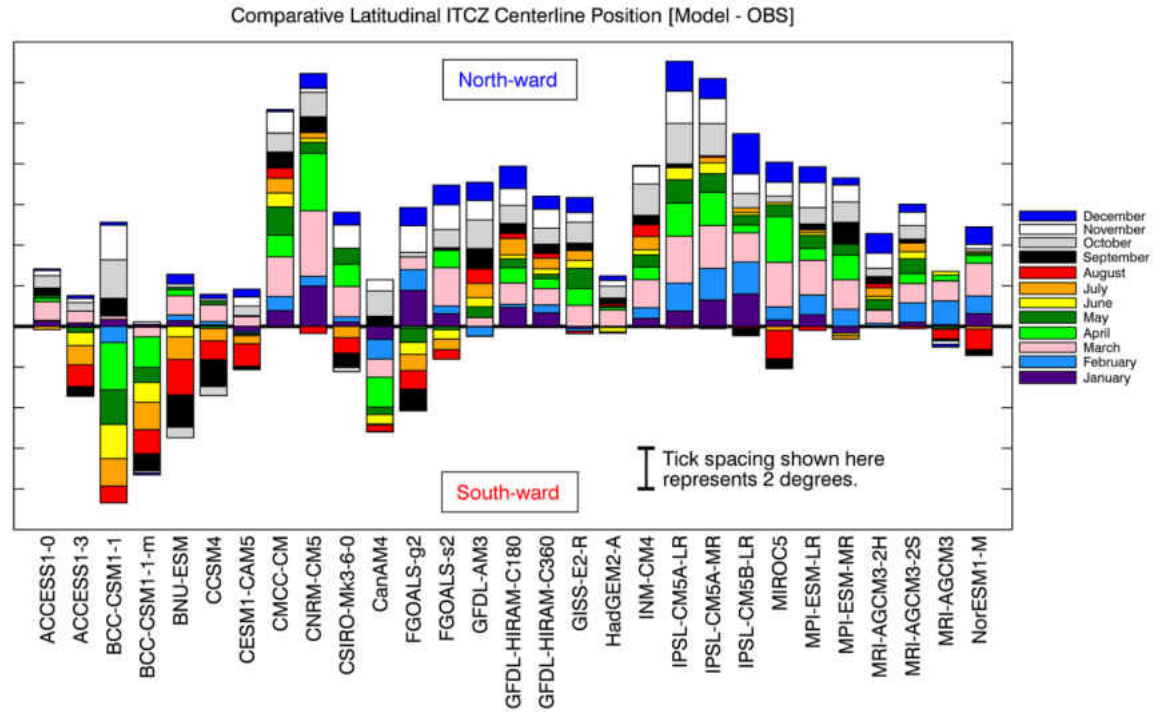
Figure 41. Position of the ITCZ centerline as derived by our algorithm, shown as each respective GCM minus observations. Each month is color coded as shown in the legend. The horizontal black line found near the center of the diagram can be interpreted as the centerline derived from GPCP and TRMM observations. As such, if the colored bar is above (below) the black line, this suggests the centerline of the ITCZ simulated by a GCM is located more northward (southward) compared to observations. Each bar is vertically stacked for each respective GCM, meaning the bias found in each month should be measured as the length of respectively colored bar and not as the distance from the black line. Bars are stacked with January closest to the black bar, and expands outward, stacked vertically, progressing by month to December.

Comparisons of the ITCZ widths between each GCM and the GPCP observation are shown in Figure 42a, while comparisons with the TRMM observations are shown in Figure 42b. Tick spacing shown in Figure 42 is 4 degrees. Monthly values above (below) the horizontal black line represent months where the vertical width of the modeled ITCZ

110

is wider (thinner) than the ITCZ observed by GPCP or TRMM. We found that the width of the ITCZ observed by TRMM is thinner than the ITCZ observed by GPCP. The thinner band found in the TRMM observations is attributed to two factors: TRMM observations have a finer native resolution, and the TRMM satellite uses the on-board precipitation radar which is able to detect precipitating clouds but is insensitive to non-precipitating clouds, while the GPCP product is primarily derived from satellite infrared brightness measurements where the cloud-top temperatures from precipitating and non-precipitating clouds are almost the same (Stenz et al. 2014, 2016).

Results shown in Figure 42 illustrate that most of the GCMs simulate a wider band of precipitation (above the horizontal black line) in the Pacific ITCZ compared to both GPCP (Figure 42a) and TRMM (Figure 42b) observations. A few of the GCMs simulate the width of the ITCZ relatively close to the ITCZ observed from GPCP, such as the ACCESS1-3, CMCC-CM, IPSL-CM5A-LR, IPSL-CM5A-MR, MPI-ESM-LR, MPI-ESM-MR, and the MRI-AGCM3. However, these models all simulate wider bands of precipitation more frequently when compared to the ITCZ observed from TRMM. The IPSL-CM5B-LR is the only model to simulate a thinner band of precipitation for nearly all months when compared to GPCP and TRMM. It should be noted that the precipitation produced by the IPSL-CM5B-LR drops below the monthly thresholds for large sections of the ITCZ. The differences between the French IPSL-CM5A-LR and IPSL-CM5B-LR are hypothesized to be a result of the changes made to parameterizations in the IPSL-CM5B-LR model (Dufresne et al. 2012, Hourdin et al. 2013). Interestingly, the BCC-CSM1-1 and the BCC-CSM1-1-m simulations show opposite results compared to each

other in Figure 42, suggesting either a significant change in modeled dynamics or that differing spatial resolution of these two models may play a role.
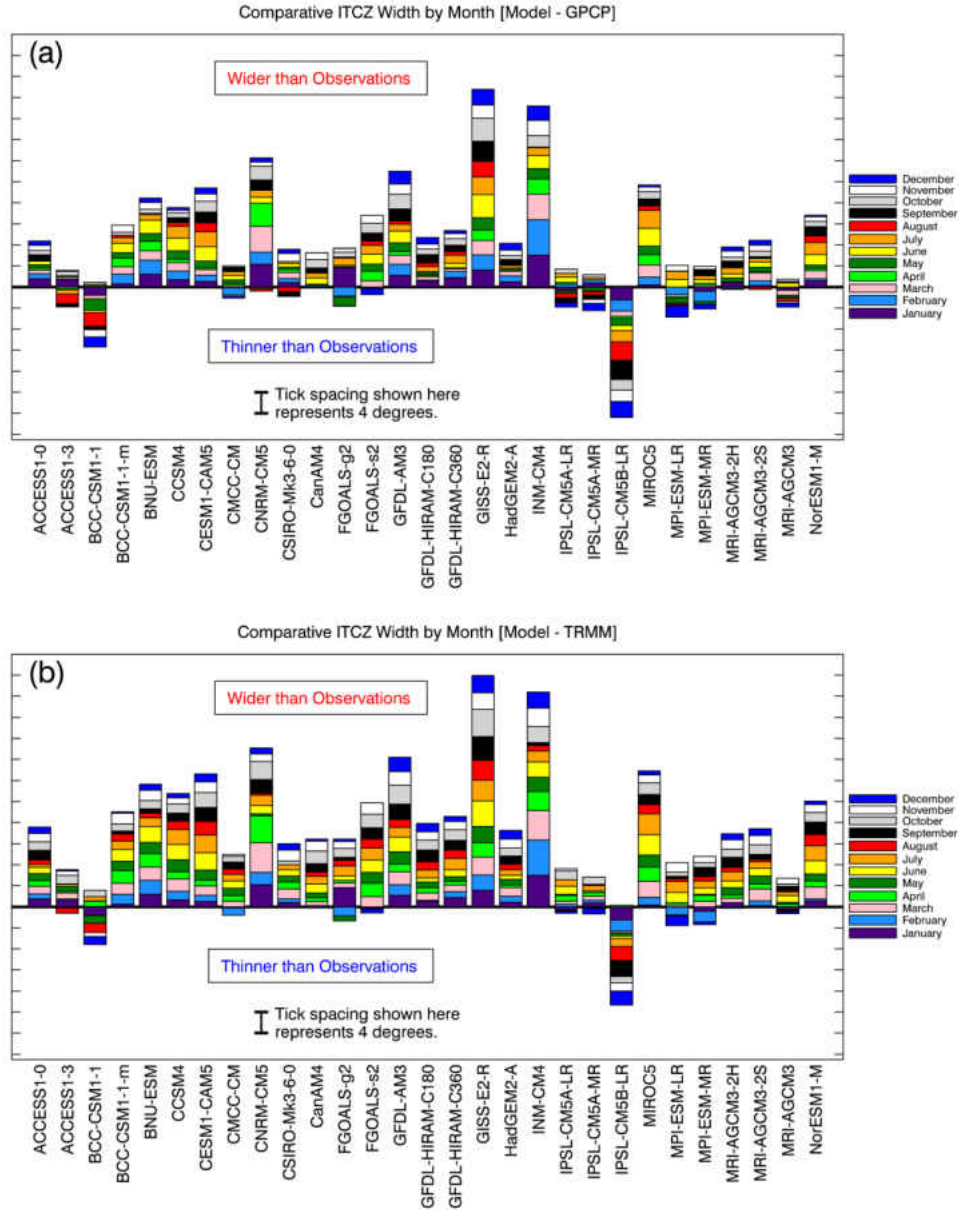
Figure 42. As in Figure 41, except showing the width of the ITCZ as derived by our algorithm, calculated as the distance between the upper and lower boundaries of the ITCZ, shown as each respective GCM minus (a) GPCP or (b) TRMM observations. The colored bars above (below) the horizontal black line represent months where the vertical width of the simulated ITCZ of the respective GCM was found to wider (thinner) than the observed ITCZ.

6.1.3 Magnitude of Precipitation in AMIP Simulations

Comparisons in the magnitude of precipitation between the GCMs and GPCP and TRMM observations are presented in Figs. 43a and 43b, respectively. The tick spacing in Figure 43 is given as 4 mm/day. Monthly values above (below) the horizontal black line represent months where the GCM simulated magnitude of precipitation in the ITCZ is stronger (weaker) than that of the respective observations. It should be noted that the biases in the magnitude of precipitation are prone to both magnitude and positional errors. Comparing GPCP and TRMM results from Fig. 43 shows only minor variations from month to month between the two results, suggesting that GPCP and TRMM precipitation estimates are roughly equal in magnitude.

Figure 43 also reveals that most of the GCMs simulated stronger precipitation compared to both GPCP and TRMM precipitation products. A few models, namely the BCC-CSM1-1 and the suite of IPSL GCMs, simulated weaker precipitation than both observations. Of the GCMs that were found to be oversimulating precipitation in the Pacific ITCZ, most of these GCMs had higher biases in the northern hemispheric summer months, with June showing the highest positive precipitation bias.

Based on the comparisons in Figure 41 through Figure 43, we can conclude that most of the models tend to simulate a stronger, wider ITCZ shifted slightly northward compared to the ITCZ observed by GPCP and TRMM.
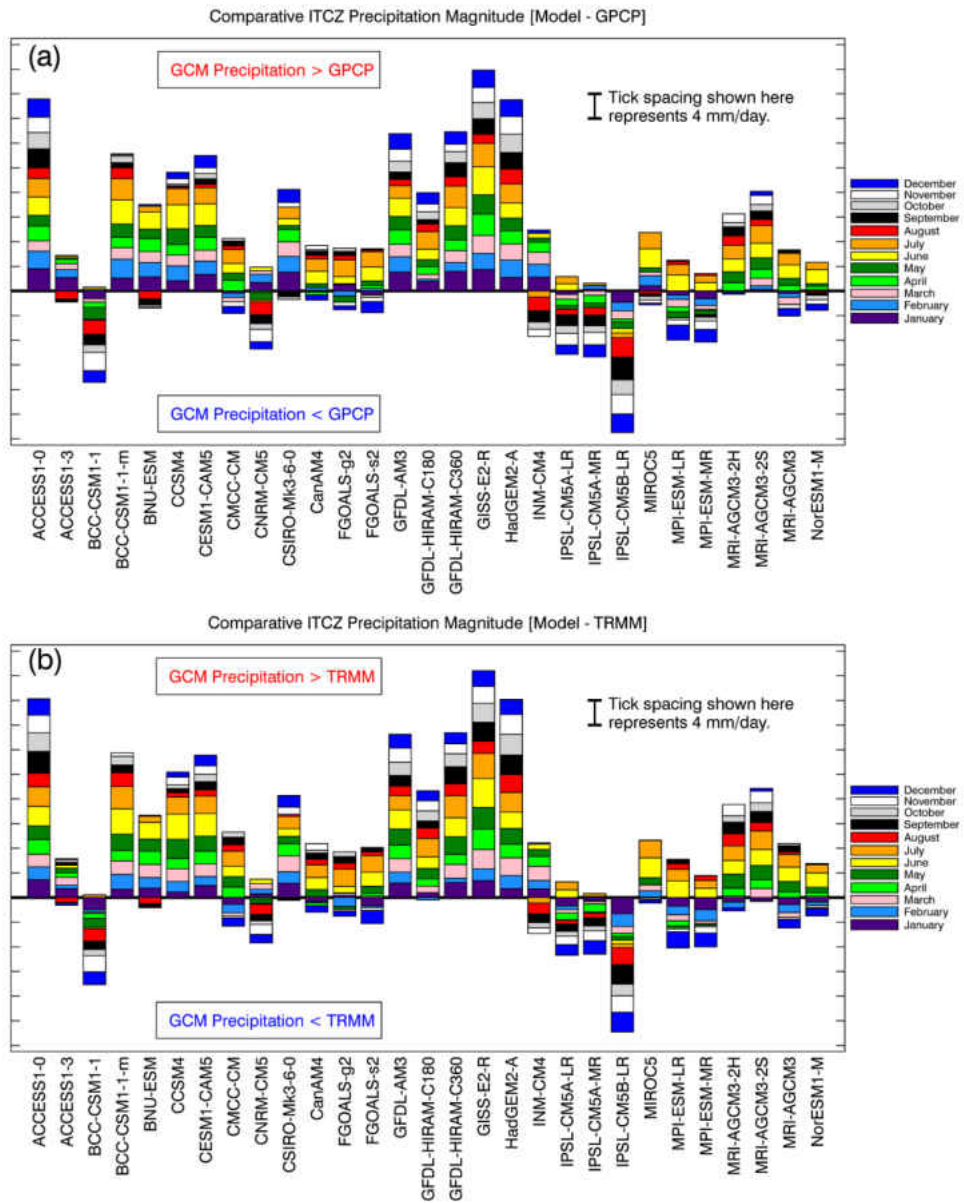
Figure 43. As in Figure 41, except showing the magnitude of precipitation within the ITCZ as derived by the algorithm in Stanfield et al. (2016), shown as each respective GCM minus (a) GPCP or (b) TRMM observations. The colored bars above (below) the horizontal black line represent months where the precipitation of the respective GCM was found to simulated stronger (weaker) than that of the respective observations.

114

6.1.4 Historical/CMIP vs AMIP Simulations

The metrics derived in this study, including the ITCZ Centerline, width of the ITCZ band, and magnitude of precipitation, are prone to both positional/dynamic and magnitude/parameterization biases. To examine the strength and role of the coupled ocean dynamics/positional biases, we compare historical and AMIP simulations with identical parameterizations. In detail, the precipitation from 20 available historical and AMIP simulations have each been averaged between ±4° latitude of the average observed centerline, and their differences are shown in Figure 44 given as the historical simulation (CMIP) minus the AMIP simulation. Since the AMIP and CMIP versions of each model compared in Figure 44 use the same parameterizations, their precipitation differences are highly attributed to dynamic/positional influences, which can be used to estimate the strength of the potential bias in each GCM. A list is provided in Table 8 to identify how this study has linked the historical and AMIP simulations between GCMs.
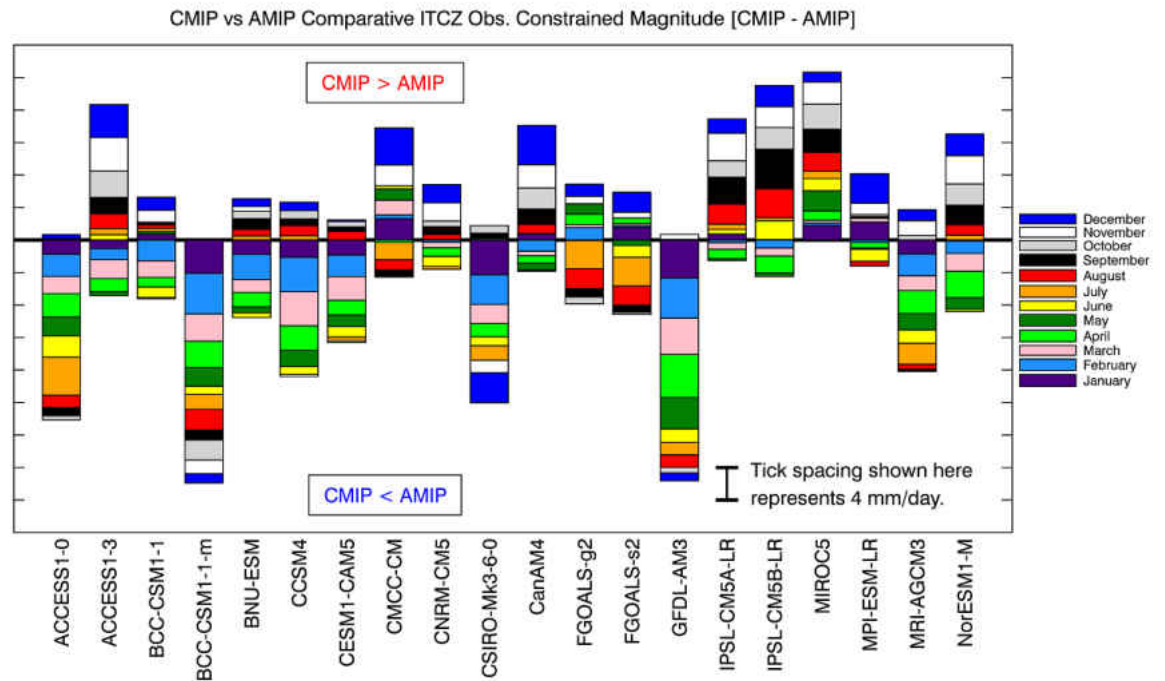
Figure 44. As in Figure 41, except showing the ITCZ precipitation comparison between AMIP and historical ocean-coupled (CMIP) precipitation given as CMIP minus AMIP. The colored bars above (below) the horizontal black line represent months where precipitation in the respective GCM is found to be greater in the CMIP (AMIP) simulation.

In general, the comparisons of precipitation simulated by identical AMIP and CMIP versions of the model are nearly equally distributed around the black line (Figure 44). More specifically, there is roughly an even split between three different scenarios where: (1) the CMIP version of the GCM simulated more precipitation than their AMIP counterparts (e.g., ACCESS1-3, CMCC-CM, CanAM4, IPSL-CM5, MIRCO5), (2) the CMIP version of the GCM simulated less precipitation than their AMIP counterparts (e.g., ACCESS1-0, BCC-CSM1-1m, CSIRO-MK3-6-0, GFDL-AM3), or (3) the model showed a monthly split between simulating more/less precipitation when comparing CMIP and AMIP simulations (e.g., BCC-CSM1-1, BNU-ESM, FGOAL, NorESM1-M).

To investigate their differences, we examined the vertical upwelling (omega, ω) fields at 850 mb and found that there is no significant difference between two simulations. Further study is warranted to understand why some of the CMIP models simulated more precipitation, while others simulated less precipitation compared to their AMIP counterparts. The role of SST during the simulations will be examined.

6.2 Update to Stanfield et al. (2016)

The global distributions of precipitation observed by GPCP and TRMM and simulated by the C5, P5 and E5 versions of the GCM have been examined in this section. Annually average precipitation rates are shown in Figure 45, given in units of millimeters per day, for GPCP and TRMM observations, and for the C5, P5, and E5 versions of the GCM. Zonal averages of annual precipitation rates are provided in Figure 46. Global means, standard deviations, and correlations and root-mean-square deviations of the GCM simulations in comparison with GPCP and TRMM precipitation products are provided in Table 9.

GPCP and TRMM observations agree well regionally (Fig. 45) and across most latitudes zonally (Fig. 46), excluding the boundary of TRMM observations around ±37° of latitude. Within the tropics, TRMM observes slightly higher precipitation rates than the GPCP product, potentially due to the onboard precipitation radar and/or the finer spatial resolution of the TRMM precipitation product. In Stanfield et al. (2016), it was found that the C5 version of the NASA GISS GCM tended to produce a wider and stronger band of precipitation over the North Pacific ITCZ in comparison to both GPCP and TRMM observations. While all three versions of the GCM agree well on a global

scale, with global means ranging across a small range (2.7 - 3.1 mm/day), the models

vary substantially on a regional scale, particularly over the defined regions of interest.
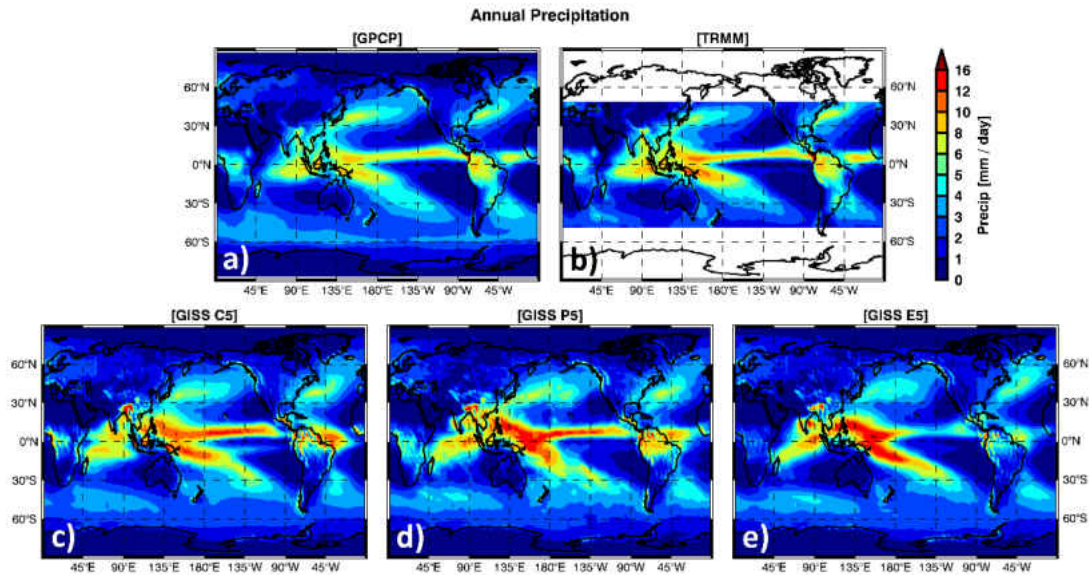
Figure 45. Annually averaged precipitation, given in units of millimeters per day, for (a) GPCP and (b) TRMM observations, and for the (c) C5, (d) P5, and (e) E5 versions of the NASA GISS GCM.
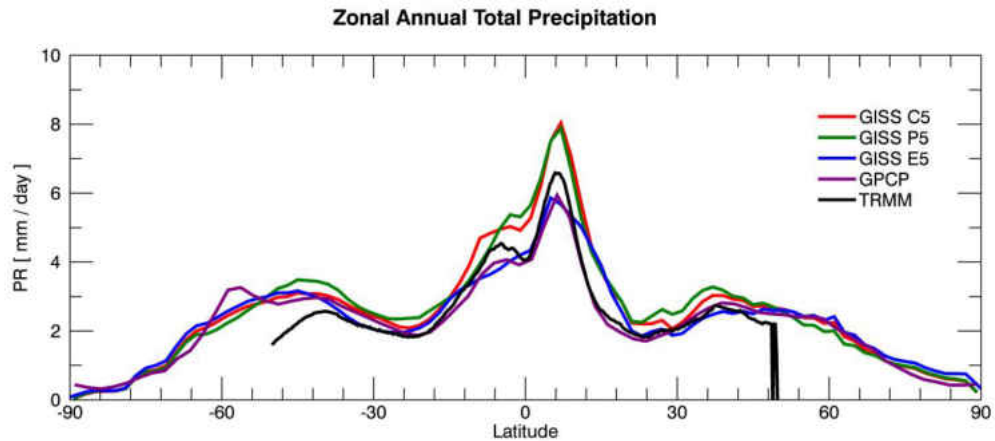
Figure 46. Zonal annually averaged precipitation rates, given in units of millimeters per day, for (purple) GPCP and (black) TRMM observations, and for the (red) C5, (green) P5, and (blue) E5 versions of the NASA GISS GCM.

118

Table 9. Annual PR weighted means, standard deviations, and correlation and root-mean-square deviation (RMSE) in relation to GPCP globally and in TRMM between ±37°

Dataset	Global Mean [mm / day]	Std. Dev. [mm / day]	Corr. [GPCP]	RMSD [GPCP]	Corr. [TRMM]	RMSD [TRMM]
GPCP	2.7	1.8	-	-	-	-
TRMM	2.9	4.9	-	-	-	-
GISS C5	3.1	2.4	0.83	1.4	0.41	4.1
GISS P5	3.2	2.5	0.85	1.4	0.42	4.1
GISS E5	2.8	2.2	0.79	1.4	0.39	4.1

PDFs and scatterplots of precipitation rates from GPCP and TRMM observations, as well as simulated from the C5, P5, and E5 versions of the GCM over the EP-ITCZ and the INDO-WP regions of focus are shown in Figures 47 and 48, respectively. Statistics of regional weighted means, standard deviations, and correlations and RMSDs in comparison with SYN1 and CCCM observations based on these focus regions are listed in Table 10.

Precipitation rates in the latest E5 simulation of the GCM have decreased substantially in the EP-ITCZ to nearly half of the precipitation found in its C5 and P5 predecessors, lowering regional correlations with GPCP (C5: 0.91; P5: 0.89; E5: 0.79) and TRMM (C5: 0.90; P5: 0.92; E5: 0.84) observations but decreasing RMSDs (Fig. 47). Over the INDO-WP, new changes in the latest version of the GCM have increased simulated precipitation over the ocean while decreasing precipitation over land (direct comparisons not shown here). This is consistent with intermodel comparisons of vertical motion, suggesting that these two factors may be linked as stronger vertical motion should promote particle growth.

Table 10. Statistics detailing PR found in the EP-ITCZ and INDO-WP regions in comparison with GPCP and TRMM precipitation products.

Region 1 – Eastern Pacific Northern ITCZ [EP-ITCZ]						
Dataset	Mean [mm / day]	Std. Dev. [mm / day]	Corr. [GPCP]	RMSD [GPCP]	Corr. [TRMM]	RMSD [TRMM]
GPCP	4.6	2.3	-	-	-	-
TRMM	4.1	2.8	-	-	-	-
GISS C5	6.6	3.6	0.91	2.7	0.90	3.0
GISS P5	6.1	3.6	0.89	2.4	0.92	2.5
GISS E5	3.5	1.7	0.79	1.8	0.84	1.7
Region 2 – Indonesia and Western Pacific [INDO-WP]						
Dataset	Mean [mm / day]	Std. Dev. [mm / day]	Corr. [GPCP]	RMSD [GPCP]	Corr. [TRMM}	RMSD [TRMM]
GPCP	5.2	2.1	-	-	-	-
TRMM	6.0	2.7	-	-	-	-
GISS C5	6.6	3.8	0.71	3.1	0.66	2.9
GISS P5	6.9	4.3	0.71	3.6	0.66	3.3
GISS E5	6.8	4.5	0.64	3.9	0.65	3.5
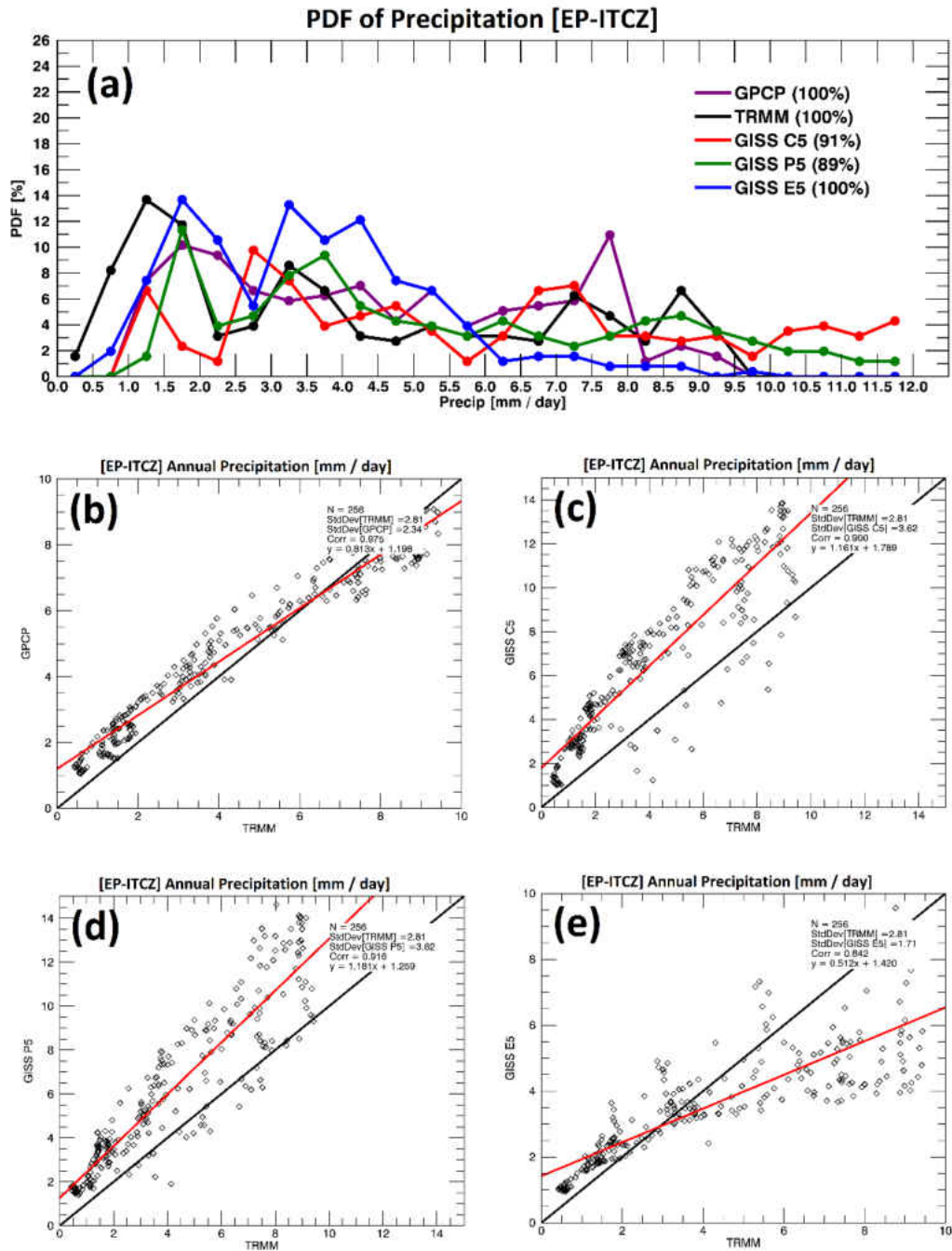
Figure 47. (a) PDFs of precipitation rates found in (purple) GPCP and (black) TRMM observations, as well as the (red) C5, (green) P5, and (blue) E5 simulations within the EP-ITCZ region, and scatterplots comparing EP-ITCZ PRs found in TRMM as compared to (b) GPCP, (c) C5, (d) P5, and the (e) E5 GCM simulations.
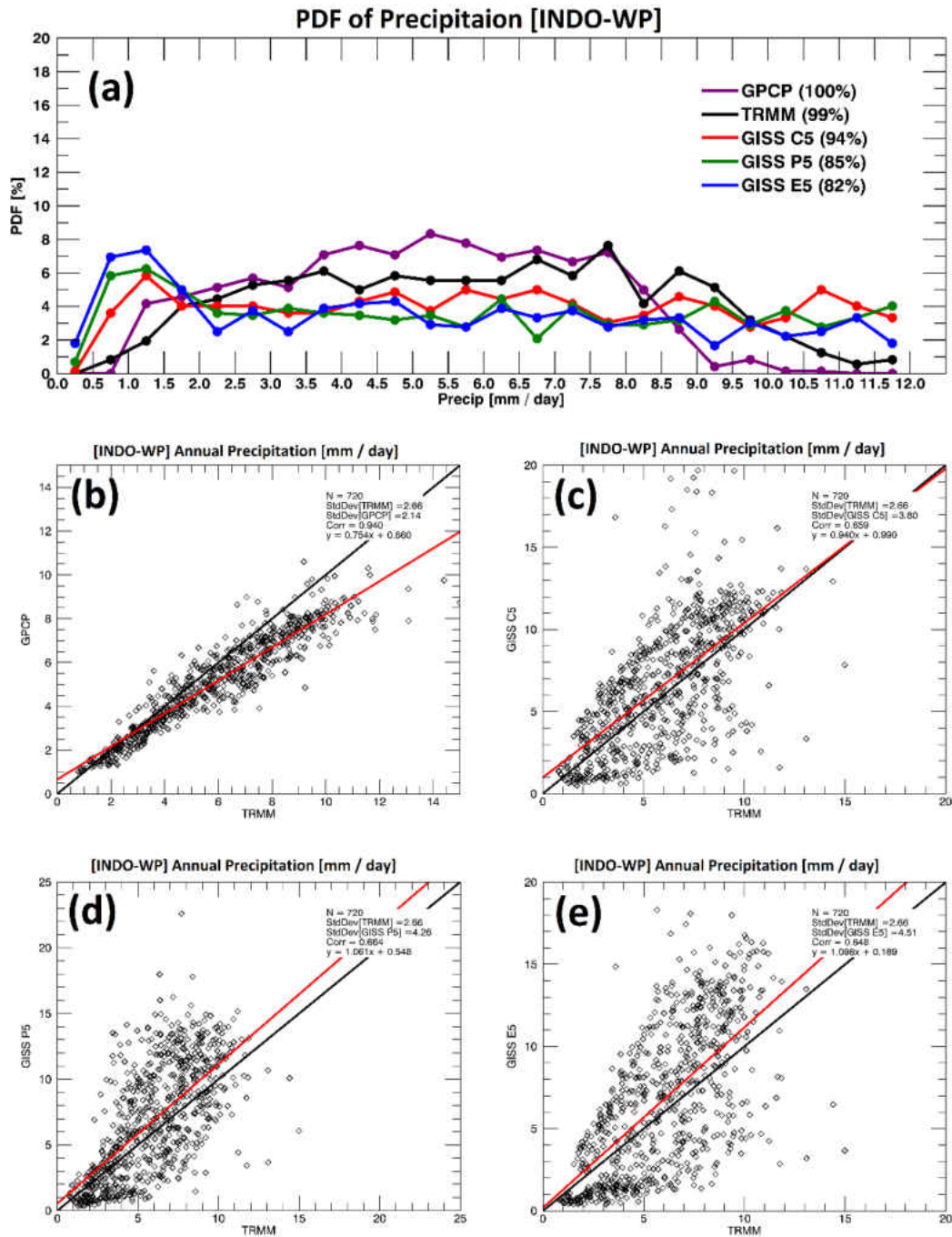
Figure 48. (a) PDFs of precipitation rates found in (purple) GPCP and (black) TRMM observations, as well as the (red) C5, (green) P5, and (blue) E5 simulations within the INDO-WR region, and scatterplots comparing INDO-WP PRs found in TRMM as compared to (b) GPCP, (c) C5, (d) P5, and the (e) E5 GCM simulations.

6.3 Summary of Precipitation

A new algorithm has been developed in Stanfield et al. (2016) to define the North Pacific ITCZ through several metrics: the centerline position of the ITCZ, the width of the ITCZ, and the magnitude of precipitation along the defined ITCZ. These metrics have allowed for a quantitative evaluation of magnitude-, location-, and width-based precipitation biases over the Pacific ITCZ from 29 CMIP5 GCMs using the GPCP and TRMM precipitation products as a ground truth. Based on the ITCZ metrics derived from our multiyear analysis and the comparisons between the model simulations and observations, the following conclusions have been made:

1) The GCMs predominately simulate the centerline of the ITCZ northward when compared to GPCP and TRMM observations, with the greatest shifts occurring in March. Few GCMs shift southward, such as the BCC-CSM1-1 and the BCC-CSM1-1-m. Some of the models show promise with either low biases or by a balancing of northward and southward biases, such as the ACCESS1-0, ACCESS1-3, CCSM4, CESM-CAM5, CanAM4, HadGem2-A, and the MRI-AGCM3.

2) Most of the GCMs simulate a much wider band of precipitation in the Pacific ITCZ compared to both GPCP and TRMM observations. A few of the GCMs simulate ITCZ widths relatively close to the observations, such as the ACCESS1-3, CMCC-CM, IPSL-CM5A-LR, IPSL-CM5A-MR, MPI-ESM-LR, MPI-ESM-MR, and the MRI-AGCM3. The IPSL-CM5B-LR is the only model to generate a thinner band of precipitation.

3) The GCMs tend to oversimulate precipitation compared to GPCP and TRMM observations. Of these GCMs, most have higher biases in the northern hemispheric summer months, with June showing the highest positive precipitation bias. A few of the models, namely the BCC-CSM1-1 and the suite of IPSL GCMs, simulate less precipitation than the observations.

4) Comparisons of precipitation simulated by identical AMIP and CMIP versions of the model are nearly equally distributed for the 20 available GCMs used in this study. In detail, an equal split is found between three scenarios. (1) Some of the GCMs simulated more precipitation in the CMIP version of the GCM compared to their AMIP counterparts, (2) while other GCMs simulated more precipitation in their AMIP counterpart. (3) Some of the GCMs showed an even monthly split between CMIP or AMIP simulations simulating more precipitation. Analysis of vertical upwelling (omega, ω) fields at 850 mb showed no significant difference between two simulations. Further study is warranted to understand why some CMIPs simulated more precipitation, while others were less than their AMIP counterparts.

With the recent changes to the E5 version of the GCM, precipitation rates remain similar on a global scale, however, large differences are observed on regional scales. Within the EP-ITCZ, precipitation in the latest E5 simulation has decreased substantially, to nearly half that of its predecessors (C5, P5). Over the INDO-WP region, mean precipitation remains similar, but closer examination has found that more/less precipitation is simulated over the ocean/land in the E5 simulation.

With regards to precipitation over the EP-ITCZ, results from Fig. 45 suggest that modifications made in the E5 version of the NASA GISS GCM may result in a thinner, more southward band of simulated precipitation in the ITCZ. A number of studies have shown how the ITCZ position is closely related to the amount of atmospheric heat transport across the equator (AHT_{EQ}) on a broad range of time scales. Chiang and Bitz (2005) found that forcing and feedbacks in the extratropics can remotely influence the location of the ITCZ. Kang et al. (2008) demonstrated a relationship between AHT_{EQ} and the ITCZ location using a slab ocean aquaplanet simulation where a hemispheric asymmetry in atmospheric heating was imposed by introducing a surface heating in the southern extratropics and an equal surface cooling in the northern extratropics. Yoshimori and Broccoli (2008 and 2009) also showed that change in AHT_{EQ} in response to hemispheric asymmetric forcing was closely related to the meridional shift in the Hadley cell, which itself was a response to the hemispheric asymmetry of the forcing and feedbacks.

Future work is recommended to examine how this potential shift of the ITCZ in the E5 GCM simulation may impact AHT_{EQ} as initial results using the precipitation centroid definition described in Frierson and Hwang (2012) suggests a potential southerly shift of the ITCZ in the E5 GCM simulation (not shown here). Calculations of AHT_{EQ} in future work of this study will use the methods described in Donohoe et al. 2013 to define AHT_{EQ}.

CHAPTER VII

SUMMARY OF UPDATED RESULTS

In this study, we analyzed how fields of cloud fraction (CF), ice water path (IWP), ice water content (IWC), vertical motion, precipitation, and precipitable water vapor (PWV) changed in three iterations of the NASA GISS ModelE GCM (the frozen CMIP5 version [C5], a post-CMIP5 version with modifications to cumulus and boundary layer turbulence parameterizations [P5], and the most recent version of the GCM which builds on the post-CMIP5 version with further modifications to the convective cloud ice parameterization [E5]). In this study, we also examine how each set of modifications has impacted the corresponding cloud, radiation, and precipitation properties in the GCM. Based on the results of this study, the following conclusions have been reached:

1) Recent changes to the E5 GCM have decreased IWP globally compared to previous versions of the model. Comparisons of IWC profiles show that the GCM simulates increasing IWC with height, peaking in the upper portions of the atmosphere, while 2C-ICE observations peak in the lower levels of the atmosphere and decrease with height, effectively opposite of each other. EP-ITCZ and INDO-WP comparisons show that the E5 simulated IWCs decrease faster with height in the EP-ITCZ than in the INDO-WP region.

2) Regional biases make large-scale comparisons unreliable and uninteresting. Vertical motion within the newest E5 simulation is greatly weakened over the

EP-ITCZ region, potentially due to atmospheric loading from enhanced ice particle fall speeds. Comparatively, E5 simulated upward motion in the INDO-WP is stronger than its predecessors. Changes in the E5 simulation have resulted in stronger/weaker upward motion over the ocean/land in the INDO-WP region in comparison with both the C5 and P5 predecessors.

3) Previous studies have shown that changes to the PBL parameterization increased CFs within the P5 simulation compared to the previous C5 model. New changes in the E5 simulation have decreased cloud fractions globally compared to P5 while maintaining the same overall spatial pattern. Profiles of CF peak at lower heights in the E5 simulation, which will potentially increase outgoing longwave radiation due to higher cloud top temperatures, which will counterbalance the decrease in reflected shortwave associated with lower CFs and the thinner optical depths associated with decreased IWC and LWC in the E5 simulation.

4) Precipitation rates remain similar on a global scale, however, large differences are observed on regional scales. Within the EP-ITCZ, precipitation in the latest E5 simulation has decreased substantially, to nearly half that of its predecessors (C5, P5). Over the INDO-WP region, mean precipitation remains similar, but closer examination has found that more/less precipitation is simulated over the ocean/land in the E5 simulation.

5) On a global-scale, E5-simulated PWV is now in perfect agreement with AMSR-E observations. Regionally, the E5 version of the GCM simulates much higher than both AMSR-E and its predecessors (C5, P5). Correlations with AMSR-E remain very high (0.99) despite regional differences.

In conclusion, while recent changes to the NASA GISS ModelE GCM suggested in Elsaesser et al. (2017) have improved the accuracy of the GCM in comparison with satellite and surface based observations, there is still room for improvement on a regional scale.

Potential Future Work and Suggestions

For future studies, running the GCM in-house should be a top priority. Without having direct access to the GCM, temporal scales and available variables are limited while forcing the investigator to perform a black box analysis wherein multiple changes are made between each iteration of the GCM and the impacts of each change as well as the interactions between each of these changes cannot be analyzed on an individual basis. Further analysis should be performed over the defined "INDO-WP" region to investigate how parameterization changes in the GCM lead to opposite results over ocean and land.

A comparison of E5-simulated radiative properties with CE observations and its predecessors is recommended based on observed changes to cloud properties in the E5 version of the GCM. With access to E5-simulated radiative fields, it is recommended to

examine how the potential shift of the ITCZ in the E5 simulation may impact AHT_{EQ} as initial results using the precipitation centroid definition detailed in Frierson and Hwang (2012) and calculations of AHT_{EQ} based on the methods described in Donohoe et al. (2013) suggests a potential southerly shift of the ITCZ in the E5 GCM simulation (not shown).

In most studies, changes made to the GCM are often observed and discussed on fairly short and recent to near-future time scales. It would be of interest to examine how each of the recent changes to the GCM might affect future climate forecasts in the distant future.

Finally, it is recommended that vertical ice water content be further examined within the GCM. While IWC generally increases towards the base of the cloud as observed in nature, this study found that the latest E5 version of the GCM still simulates increasing IWC with height in the upper levels of the atmosphere at the monthly scale. IWC magnitude is also strongly decreased in the latest version of the GCM, bringing the magnitude of IWC in the GCM much lower than is found using 2C-ICE retrievals. This comparison however may not be accurate given that 2C-ICE retrieves both stratiform and convective cloud ice while the GCM simulates only stratiform cloud ice.

REFERENCES

Adler RF et al (2003) The Version 2 Global Precipitation Climatology Project (GPCP) Monthly Precipitation Analysis (1979–Present). J. Hydrometeor., 4, 1147–1167

AghaKouchak A, Nasrollahi N, Habib E (2009) Accounting for Uncertainties of the TRMM Satellite Estimates. Remote Sens., 1, 606-619

Austin RT, A.J. Heymsfield, and G. Stephens, 2009: Retrieval of ice cloud microphysical parameters using the CloudSat millimeter-wave radar and temperature, J. Geophys. Res., 114, D00A23, doi:10.1029/2008JD010049.

Bony, S., and J.-L. Dufresne, 2005: Marine boundary layer clouds at the heart of tropical cloud feedback uncertainties in climate models, Geophys. Res. Lett., 32, L20806, doi:10.1029/2005GL023851.

Chiang, J. C. H., and C. M. Bitz, 2005: Influence of high latitude ice cover on the marine intertropical convergence zone. Climate Dyn., 25, 477–496, doi:https://doi.org/10.1007/s00382-005-0040-5

Chen L., Y. Yu, and D. Sun, 2013: Cloud and water vapor feedbacks to the El Niño warming: Are they still biased in CMIP5 models? J. Clim. doi: 10.1175/JCLI-D-12-00575.1.

Chiriaco, M. et al., 2007: Comparison of CALIPSO-Like, LaRC, and MODIS Retrievals of Ice-Cloud Properties over SIRTA in France and Florida during CRYSTAL-FACE, Journal of Applied Meteorology and Climatology, 46(3), 249-272, doi:10.1175/JAM2435.1.

Del Genio, A.D., W. Kovari, M.-S. Yao, and J. Jonas, 2005: Cumulus microphysics and climate sensitivity. J. Climate, 18, 2376-2387, doi:10.1175/JCLI3413.1.

Del Genio, A. D., M.-S. Yao, and J. Jonas (2007), Will moist convection be stronger in a warmer climate?, Geophys. Res. Lett., 34, L16703, doi:10.1029/2007GL030525.

Del Genio, A.D., Y.-H. Chen, D. Kim, and M.-S. Yao, 2012: The MJO transition from shallow to deep convection in CloudSat/CALIPSO data and GISS GCM simulations. J. Climate, 25, 3755-3770, doi:10.1175/JCLI-D-11-00384.1.

Deng, M., G. G. Mace, Z. Wang, and E. Berry, 2015: CloudSat 2C-ICE product update with a new Ze parameterization in lidar-only region, J. Geophys. Res. Atmos., 120, 12,198-12,208, doi:10.1002/2015JD023600.

Doelling, D. R., N. G. Loeb, D. F. Keyes, M. L. Nordeen, D. Morstad, C. Nguyen, B. A. Wielicki, D. F. Young, and M. Sun, 2013: Geostationary enhanced temporal interpolation for CERES flux products. J. Atmos. Oceanic Technol., 30, 1072-1090.

Dolinar E, Dong X, Xi B, Jiang J, Su H (2015a) Evaluation of CMIP5 simulated clouds and TOA radiation budgets using NASA satellite observations. Clim Dyn, 44, 2229-2247. doi:10.1007/s00382-014-2158-9

Dolinar E, Dong X, Xi B (2015b) Evaluation and Intercomparison of Clouds, Precipitation, and Radiation Budgets in Recent Reanalyses using Satellite-Surface Observations. Climate Dynamics, DOI: 10.1007/s00382-015-2693-z.

Dong, X. and G. G. Mace, 2003: Arctic Stratus Cloud Properties and Radiative Forcing Derived from Ground-Based Data Collected at Barrow, Alaska, J. Climate, 16(3), 445-461.

Dong, X, B. Xi, and P. Minnis, 2006: A Climatology of Midlatitude Continental Clouds from the ARM SGP Central Facility. Part II: Cloud Fraction and Surface Radiative Forcing, J. Climate, 19(9), 1765-1783.

Dong, X., P. Minnis, B. Xi, S. Sun-Mack, and Y. Chen, 2008: Comparison of CERES-MODIS stratus cloud properties with ground-based measurements at the DOE ARM Southern Great Plains site, J. Geophys. Res., 113, D03204.

Dong, X., B. Xi, K.Crosby, C.N.Long, and R.Stone, 2010: A 10 year climatology of Arctic cloud fraction and radiative forcing at Barrow, Alaska J. Geophys. Res. D12124, doi:10.1029/2009JD013489.

Dong, X., B. Xi, and P. Wu (2014), Investigation of the diurnal variation of marine boundary layer cloud microphysical properties at the Azores, J. Clim., 27(23), 8827–8835, doi:10.1175/jcli-d-14-00434.1.

Dong X, B Xi, S Qiu, P Minnis, S Sun-Mack, and F Rose. 2016. "A radiation closure study of Arctic stratus cloud microphysical properties using the collocated satellite-surface data and Fu-Liou radiative transfer model." Journal of Geophysical Research: Atmospheres, 121(17), 10.1002/2016jd025255.

Donohoe, A., Marshall, J., Ferreira, D. & Mcgee, D. The relationship between ITCZ location and cross-equatorial atmospheric heat transport: From the seasonal cycle to the last glacial maximum. Journal of Climate 26, 3597–3618, doi:10.1175/JCLI-D-12-00467.1 (2013).

Dufresne et al (2012) Climate change projections using the IPSL-CM5 Earth System Model: from CMIP3 to CMIP5. Clim Dyn, 40, 2123-2165. doi:10.1007/s00382-012-1636-1

Elsaesser, G.S., A.D. Del Genio, J. Jiang, and M. van Lier-Walqui, 2017: An improved convective ice parameterization for the NASA GISS Global Climate Model and impacts on cloud ice simulation. J. Clim., 30, no. 1, 317-336, doi:10.1175/JCLI-D-16-0346.1.

Fetzer, E. J., B. H. Lambrigtsen, A. Eldering, H. H. Aumann, and M. T. Chahine, 2006: Biases in total precipitable water vapor climatologies from Atmospheric Infrared Sounder and Advanced Microwave Scanning Radiometer, J. Geophys. Res., 111, D09S16, doi:10.1029/2005JD006598.

Flato G, Marotzke J, B. Abiodun B, Braconnot P, Chou SC, Collins W, Cox P, Driouech F, S. Emori S, V. Eyring V, Forest C, Gleckler P, Guilyardi E, Jakob C, Kattsov V, Reason C, Rummukainen M (2013) Evaluation of Climate Models. In: Climate Change 2013: The Physical Science Basis. Contribution of Working Group I to the Fifth Assessment Report of the Intergovernmental Panel on Climate Change [Stocker, T.F., D. Qin, G.-K. Plattner, M. Tignor, S.K. Allen, J. Boschung, A. Nauels, Y. Xia, V. Bex and P.M. Midgley (eds.)]. Cambridge University Press, Cambridge, United Kingdom and New York, NY, USA.

Frierson DMW, Hwang Y-T (2012) Extratropical influence on ITCZ shifts in slab ocean simulations of global warming. J Clim 25:720–733

Gregory D. 2001. Estimation of entrainment rate in simple models of convective clouds. Q. J. R. Meteorol. Soc. 127: 53–72.

Habib E, Krajewski WF (2002) Uncertainty Analysis of the TRMM Ground-Validation Radar-Rainfall Products: Application to the TEFLUN-B Field Campaign. J. Appl. Meteor., 41, 558–572.

Hirota N, Takayabu YN, Watanabe M, Kimoto M (2011) Precipitation reproducibility over tropical oceans and its relationship to the double ITCZ problem in CMIP3 and MIROC5 climate models. J. Climate, 24, 4859-4873.

Holton JR, Wallace JM, Young JA (1971) On boundary layer dynamics and the ITCZ. J. Atmos. Sci., 28, 275-280.

Hourdin F, Grandpeix JY, Rio C, Bony S, Jam A, Cheruy F, Rochetin N, Fairhead L, Idelkadi A, Musat I, Dufresne JL, Lefebvre MP, Lahellec A, Roehrig R (2013) From LMDZ5A to LMDZ5B: revisiting the parameterizations of clouds and convection in the atmosperic component of the IPSL-CM5 climate model. Clim Dyn. doi:10.1007/s00382-012-1343-y

Huffman GJ, Robert F, Adler RF, Arkin P, Chang A, Ferraro R, Gruber A, Janowiak J, McNab A, Rudolf B, Udo Schneider U (1997) The Global Precipitation Climatology Project (GPCP) Combined Precipitation Dataset. Bull. Amer. Meteor. Soc., 78, 5–20. doi: http://dx.doi.org/10.1175/1520-0477(1997)078<0005:TGPCPG>2.0.CO;2

Huffman GJ, Adler RF, Bolvin DT, Gu G, Nelkin EJ, Bowman KP, E.F. Stocker EF, Wolff DB (2007) The TRMM Multi-satellite Precipitation Analysis: Quasi-Global, Multi-Year, Combined-Sensor Precipitation Estimates at Fine Scale. J. Hydrometeor., 8, 33-55.

Huffman GJ, Bolvin DT (2011) Real-Time TRMM Multi-Satellite Precipitation Analysis Data Set Documentation. NASA/GSFC Laboratory for Atmospheres, 43 pp. ftp://meso.gsfc.nasa.gov/pub/trmmdocs/rt/3B4XRT_doc.pdf.

Huffman GJ, Bolvin DT (2012) GPCP Version 2.2 SG Combined Precipitation Data Set Documentation. ftp://precip.gsfc.nasa.gov/pub/gpcp-v2.2/doc/V2.2_doc.pdf, 46 pp.

Jiang, J.H., H. Su, C. Zhai, V. Perun, A.D. Del Genio, L.S. Nazarenko, L.J. Donner, L.W. Horowitz, C.J. Seman, J. Cole, A. Gettelman, M.A. Ringer, L.D. Rotstayn, S.J. Jeffrey, T. Wu, F. Brient, J.-L. Dufresne, H. Kawai, T. Koshiro, W. Masahiro, T.S. L'Écuyer, E.M. Volodin, T. Iversen, H. Drange, M. dos Santos Mesquita, W.G. Read, J.W. Waters, B. Tian, J. Teixeira, and G.L. Stephens, 2012: Evaluation of cloud and water vapor simulations in CMIP5 climate models using NASA "A-Train" satellite observations. J. Geophys. Res., 117, no. D14, D14105, doi:10.1029/2011JD017237.

Kang, S. M., I. M. Held, D. M. W. Frierson, and M. Zhao, 2008: The response of the ITCZ to extratropical thermal forcing: Idealized slab-ocean experiments with a GCM. J. Climate, 21, 3521–
3532, doi:10.1175/2007JCLI2146.1.

Kato, S., and N.G. Loeb, 2005: Top-of-atmosphere shortwave broadband observed radiance and estimated irradiance over polar regions from Clouds and the Earth's Radiant Energy System (CERES) instruments on Terra. J. Geophys. Res., 110, doi:10.1029/2004JD005308.

Kato, S., S. Sun-Mack, W.F. Miller, F.G. Rose, Y. Chen, P. Minnis, and B.A. Wielicki, 2010: Relationships among cloud occurrence frequency, overlap, and effective thickness derived from CALIPSO and CloudSat merged cloud vertical profiles, J. Geophys. Res., 115, D00H28, doi:10.1029/2009JD012277.

Kato S, N.G. Loeb, F.G. Rose, D.R. Doelling, D.A. Rutan, T.E. Caldwell, L. Yu, R.A. Weller, 2013: Surface Irradiances Consistent with CERES-Derived Top-of-Atmosphere Shortwave and Longwave Irradiances. J. Climate, 26, 2719–2740. doi: http://dx.doi.org/10.1175/JCLI-D-12-00436.1

Kendon EJ, Roberts NM, Fowler HJ, Roberts MJ, Chan SC, Senior CA (2014) Heavier summer downpours with climate change revealed by weather forecast resolution model. Nature Climate Change 4:570-576. doi: 10.1038/nclimate2258

Kennedy, A.D., X. Dong, B. Xi, P. Minnis, A.D. Del Genio, A.B. Wolf, and M.M. Khaiyer, 2010: Evaluation of the NASA GISS Single Column Model simulated clouds using combined surface and satellite observations. J. Climate, 23, 5175-5192, doi:10.1175/2010JCLI3353.1.

Kim, D., A.H. Sobel, A.D. Del Genio, Y. Chen, S.J. Camargo, M.-S. Yao, M. Kelley and L. Nazarenko, 2012: The tropical subseasonal variability simulated in the NASA GISS general circulation model. J. Climate, 25, 4641-4659.

Klein, S.A., Y. Zhang, M.D. Zelinka, R. Pincus, J. Boyle, and P.J. Gleckler, 2013: Are climate model simulations of clouds improving? An evaluation using the ISCCP simulator. J. Geophys. Res. Atmos. 118 ,1329-1342. doi: 10.1002/jgrd.50141.

Kopp, G., and G. Lawrence, 2005: The Total Irradiance Monitor (TIM): Instrument design. Solar Phys. 230, 91-109.

Lauer, A., and K. Hamilton, 2012: Simulating clouds with global climate models: A comparison on CMIP5 results with CMIP3 and satellite data. J. Clim., doi:10.1175/JCLI-D-12-00451.1.

Li G, Xie SP (2014) Tropical biases in CMIP5 multimodel ensemble: The excessive equatorial Pacific cold tongue and double ITCZ problems. J. Climate, 27, 1765-1780.

Li G, Du Y, Xu H, Ren B (2015) An intermodel approach to identify the source of excessive equatorial Pacific cold tongue in CMIP5 models and uncertainty in observational datasets. J. Climate, 28, 7630-7640.

Li, J.-L.F., D.E. Waliser, G. Stephens, S. Lee, T. L'Ecuyer, S. Kato, N. Loeb, and H.-Y. Ma, 2013: Characterizing and understanding radiation budget biases in CMIP3/CMIP5 GCMs, contemporary GCM, and reanalysis. J. Geophys. Res. Atmos. 118, 8166–8184, doi:10.1002/jgrd.50378.

Lin J-L (2007) The double-ITCZ problem in IPCC AR4 Coupled GCMs: Oceanatmosphere feedback analysis. J. Clim., 20, 4497–4525.

Loeb, N.G., K.J. Priestley, D.P. Kratz, E.B. Geier, R.N. Green, B.A. Wielicki, P.O.R. Hinton, and S.K. Nolan, 2001: Determination of unfiltered radiances from the Clouds and the Earth's Radiant Energy System (CERES) instrument. J. Appl. Meteor., 40, 822–835.

Loeb N, N.M. Smith, S. Kato, W.F. Miller, S.K. Gupta, P. Minnis, and B.A. Wielicki, 2003: Angular distribution models for top-of-atmosphere radiative flux estimation from the Clouds and the Earth's Radiant Energy System instrument on the Tropical Rainfall Measuring Mission Satellite. Part I: Methodology. J. Appl. Meteor., 42, 240–265.

Loeb N, S. Kato, K. Loukachine, and N.M. Smith, 2005: Angular distribution models for top-of-atmosphere radiative flux estimation from the Clouds and the Earth's Radiant Energy System instrument on the the Terra satellite. Part I: Methodology. J. Atmos. Oceanic Technol., 22, 338–351.

Loeb N, W. Sun, W.F. Miller, K. Loukachine, and R. Davies, 2006: Fusion of CERES, MISR and MODIS measurements for top-of-atmosphere radiative flux validation. J. Geophys. Res., 111, D18209, doi:10.1029/2006JD007146.

Loeb N, B.A. Wielicki, W. Su, K. Loukachine, W. Sun, T. Wong, K.J. Priestley, G. Matthews, W.F. Miller, and R. Davies, 2007: Multi-instrument comparison of top-of-atmosphere reflected solar radiation. J. Climate, 20, 575-591.

Loeb N, B.A. Wielicki, D.R. Doelling, G.L. Smith, D.F. Keyes, S. Kato, N. Manalo-Smith, T. Wong, 2009: Toward optimal closure of the Earth's top-of-atmosphere radiation budget. J. Climate, 22, 748-766, doi:10.1175/2008JCLI2637.1.

Loeb N, S. Kato, W. Su, T. Wong, F. G. Rose, D. R. Doelling, J. R. Norris, and X. Huang, 2012: Advances in understanding top-of-atmosphere radiation variability from satellite observations. Surv. Geophys., 33, 359-385. DOI 10.1007/s10712-012-9175-1.

Mace, G.G., Y. Zhang, S. Platnick, M.D. King, P. Minnis, and P. Yang, 2005: Evaluation of cirrus cloud properties from MODIS radiances using cloud properties derived from ground-based data collected at the ARM SGP site. J. Appl. Meteorol., 44, 221-240.

Marchand, R., G.G. Mace, T. Ackerman and G. Stephens, 2008: Hydrometeor detection using CloudSat – an Earth-orbiting 94-GHz cloud radar. J. Atmos. Ocean Tech., 25, 519-533.

Minnis, Patrick; Huang, Jianping; Lin, Bing; Yi, Yuhong; Arduini, Robert F.; Fan, Tai-Fang; Ayers, J. Kirk; Mace, Gerald G. (2007) Ice cloud properties in ice-over-water cloud systems using Tropical Rainfall Measuring Mission (TRMM) visible and infrared scanner and TRMM Microwave Imager data Journal of Geophysical Research: Atmospheres, 112(D6), D06206. http://dx.doi.org/10.1029/2006JD007626.

Minnis, P., Q.Z. Trepte, S. Sun-Mack, Y. Chen, D.R. Doelling, D.F. Young, D.A. Spangenberg, W.F. Miller, B.A. Wielicki, R.R. Brown, S.C. Gibson, and E.B. Geier, 2008: Cloud detection in non-polar regions for CERES using TRMM VIRS and Terra and Aqua MODIS data. IEEE Trans. Geosci. Remote Sens., 46, 3857-3884.

Minnis P. et al. (2011a) CERES Edition-2 cloud property retrievals using TRMM VIRS and Terra and Aqua MODIS Data—Part I: Algorithms, Geosci. Remote Sens., 49, 4374-4400.

Minnis P et al. (2011b) CERES Edition-2 cloud property retrievals using TRMM VIRS and Terra and Aqua MODIS data, Part II: Examples of average results and comparisons with other data, IEEE Trans. Geosci. Remote Sens., 49, 4401-4430.

Misra V, Marx L, Brunke M, Zeng X (2008) The equatorial Pacific cold tongue bias in a coupled climate model, J. Climate, 21, 5852-5869.

Molod, A., Takacs, L., Suarez, M., and Bacmeister, J (2015) Development of the GEOS-5 atmospheric general circulation model: evolution from MERRA to MERRA2, Geosci. Model Dev., 8, 1339-1356, doi:10.5194/gmd-8-1339-2015, 2015.

Naud, C.M., A.D. Del Genio, M. Bauer, and W. Kovari, 2010: Cloud vertical distribution across warm fronts observed with CloudSat and CALIPSO and modeled with a general circulation model. J. Clim., 23, 3397–3415.

Nicholson SE, Some B, McCollum J, Nelkin E, Klotter D, Berte Y, Diallo BM, Gaye I, Kpabeba G, Ndiaye O, Noukpozounkou JN, Tanu MM, Thiam A, Toure AA, Traore AK (2003) Validation of TRMM and Other Rainfall Estimates with a High-Density Gauge Dataset for West Africa. Part II: Validation of TRMM Rainfall Products. J. Appl. Meteor., 42, 1355–1368.

Olsen, E.T., et al., 2007a: AIRS/AMSU/HSB Version 5 Data Disclaimer, report, 21 pp., Jet Propul. Lab., Pasadena, Calif. [Available at http:// http://disc.gsfc.nasa.gov/AIRS/documentation/v5_docs/AIRS_V5_Release_User_Docs/V 5_Data_Disclaimer.pdf]

Olsen ET, S. Granger, E. Manning, and J. Blaisdell, 2007b: AIRS/AMSU/HSB Version 5 Level 3 Quick Start, report, 25 pp., Jet Propul. Lab., Pasadena, Calif. [Available at http://disc.sci.gsfc.nasa.gov/AIRS/documentation/v5_docs/AIRS_V5_Release_User_Doc s/V5_L3_QuickStart.pdf]

Pincus R, Batstone CP, Hofmann RJP, Taylor KE, Glecker PJ (2008) Evaluating the present-day simulation of clouds, precipitation, and radiation in climate models. J. Geophys. Res. Atmos., 113, D14209.

Platnick, S., M.D. King, S.A. Ackerman, W.P. Menzel, B.A. Baum, J.C. Riedi, and R.A. Frey, 2003: The MODIS cloud products: algorithms and examples from Terra, Trans. Geosci, Remote Sens., 41(2), 459-473.

Ramanathan, V., R.D. Cess, E.F. Harrison, P. Minnis, B.R. Barkstrom, E. Ahmad, and D. Hartmann, 1989: Cloud-Radiative Forcing and Climate: Results from the Earth Radiation Budget Experiment, Science, 243(4887), 57-63.

Rossow, W.B., and R.A. Schiffer, 1999: Advances in understanding clouds from ISCCP. Bull. Amer. Meteorol. Soc., 80, 2261-2288, doi:10.1175/1520-0477(1999)080<2261:AIUCFI>2.0.CO;2.

Schmidt, G.A. et al., 2006: Present-Day Atmospheric Simulations Using GISS ModelE: Comparison to In Situ, Satellite, and Reanalysis Data, J. Climate, 19(2), 153-192.

Schmidt, G.A., M. Kelley, L. Nazarenko, R. Ruedy, G.L. Russell, I. Aleinov, M. Bauer, S.E. Bauer, M.K. Bhat, R. Bleck, V. Canuto, Y.-H. Chen, Y. Cheng, T.L. Clune, A. Del Genio, R. de Fainchtein, G. Faluvegi, J.E. Hansen, R.J. Healy, N.Y. Kiang, D. Koch, A.A. Lacis, A.N. LeGrande, J. Lerner, K.K. Lo, E.E. Matthews, S. Menon, R.L. Miller, V. Oinas, A.O. Oloso, J.P. Perlwitz, M.J. Puma, W.M. Putman, D. Rind, A. Romanou, M. Sato, D.T. Shindell, S. Sun, R.A. Syed, N. Tausnev, K. Tsigaridis, N. Unger, A. Voulgarakis, M.-S. Yao, and J. Zhang, 2014: Configuration and assessment of the GISS ModelE2 contributions to the CMIP5 archive. J. Adv. Model. Earth Syst., 6, no. 1, 141-184, doi:10.1002/2013MS000265.

Sohn, B., J. Schmetz, R. Stuhlmann, and J. Lee, 2006: Dry Bias in Satellite-Derived Clear-Sky Water Vapor and Its Contribution to Longwave Cloud Radiative Forcing, J. Climate, 19(21), 5570-5580.

Sohn, B.. and R. Bennartz, 2008: Contribution of water vapor to observational estimates of longwave cloud radiative forcing, J. Geophys. Res., 113, D20107.

Stanfield, R., 2012: Assessment of NASA GISS CMIP5 ModelE Simulated Clouds and TOA Radiation Budgets Using Satellite Observations Over the Southern Mid-Latitudes, Master's Thesis, University of North Dakota.

Stanfield RE, Dong X, Xi B, Kennedy A, Del Genio AD, Minnis P, Jiang JH (2014) Assessment of NASA GISS CMIP5 and post-CMIP5 simulated clouds and TOA radiation budgets using satellite observations: Part I: Cloud fraction and properties. J. Climate, 27, no. 11, 4189-4208, doi:10.1175/JCLI-D-13-00558.1.

Stanfield RE, Dong X, Xi B, Del Genio AD, Minnis P, Doelling D, Loeb N (2015) Assessment of NASA GISS CMIP5 and Post-CMIP5 simulated clouds and TOA radiation budgets using satellite observations. Part II: TOA radiation budget and CREs. J Clim 28(5):1842–1864. doi:10.1175/JCLI-D-14-00249.1

Stanfield RE, Jiang J, Dong X, Xi B, Su H, Donner L, Rotstayn L, Wu T, Cole J, and Shinodo E (2016) A Quantitative Assessment of Precipitation Associated with the ITCZ in the CMIP GCM Simulations. Climate Dynamics, 47: 1863. doi:10.1007/s00382-015-

2937-yWinker, D.M., W.H. Hunt, and M.J. McGill, 2007: Initial performance assessment of CALIOP, Geophys. Res. Lett., 34, L19803, doi:10.1029/2007GL030135.

Stenz R, Dong X, Xi B, Kuligowski RJ (2014) Assessment of SCaMPR and NEXRAD Q2 Precipitation Estimates Using Oklahoma Mesonet Observations. J. Hydrometeor, 15, 2484–2500.

Stenz, R., X. Dong, B. Xi, Z. Feng, and R.J. Kuligowski, 2016: Improving Satellite Quantitative Precipitation Estimation Using GOES-Retrieved Cloud Optical Depth. J. Hydrometeor., 17, 557–570, https://doi.org/10.1175/JHM-D-15-0057.1

Stephens, G.L., et al., 2002: The CloudSat Mission and the A-Train, Bull. Amer. Meteor. Soc., 83(12), 1771-1790.

Stubenrauch, C.J., and Co-Authors, 2013: Assessment of global cloud datasets from satellites: Project and database initiated by the GEWEX Radiation Panel. Bull. Amer. Meteor. Soc., 94, 1031-1049.

Su, H., et al., 2013: Diagnosis of Regime-dependent Cloud Simulation Errors in CMIP5 Models Using A-Train Satellite Observations, J. Geophys. Res. 118, 7, 2762-2780, doi:10.1029/2012JD018575 (2013).

Taylor KE (2001) Summarizing multiple aspects of model performance in a single diagram. J. Geophys. Res., 106 (D7), 7183–7192.

Taylor KE, Balaji V, Hankin S, Juckes M, Lawrence B (2010) CMIP5 Data Reference Syntax (DRS) and controlled vocabularies, 13 pp.

Taylor KE, Ronald J. Stouffer, Gerald A. Meehl (2012) An Overview of CMIP5 and the Experiment Design. Bull. Amer. Meteor. Soc., 93, 485–498.

Waliser, D., F. Li, C. Woods, R. Austin, J. Bacmeister, J. Chern, A. DelGenio, J. Jiang, Z. Kuang, H. Meng, P. Minnis, S. Platnick, W.B. Rossow, G. Stephens, S. Sun-Mack, W. K. Tao, A. Tompkins, D. Vane, C. Walker, and D. Wu, 2009: Cloud ice: A climate model challenge with signs and expectations of progress. J. Geophys. Res., 114, D00A21, doi:10.1029/2008JD010015.

Wang, H., and W. Su (2013), Evaluating and understanding top of the atmosphere cloud radiative effects in Intergovernmental Panel on Climate Change (IPCC) Fifth Assessment Report (AR5) Coupled Model Intercomparison Project Phase 5 (CMIP5) models using satellite observations, J. Geophys. Res. Atmos., 118, 683–699, doi:10.1029/2012JD018619.

Wentz, F.J., 1997: A well calibrated ocean algorithm for Special Sensor Microwave/Imager, J. Geophys. Res., 102, 8703–8718, doi:10.1029/96JC01751.

Winker, D.M., W.H. Hunt, and M.J. McGill, 2007: Initial performance assessment of CALIOP, Geophys. Res. Lett., 34, L19803, doi:10.1029/2007GL030135.

Xi, B., X. Dong, P. Minnis, and M.M. Khaiyer, 2010: A 10-year climatology of cloud cover and vertical distribution derived from both surface and GOES observations over the DOE ARM SGP Site. J. Geophys. Res.115, D12124, doi:10.1029/2009JD012800.

Xi, B., X. Dong, P. Minnis, and S. Sun-Mack, 2013: Comparison of CERES-MODIS Stratus Cloud Properties with Ground-Based Measurements at the DOE ARM AMF at AZORES Site. In preparation for JGR.

Xi, B., X.Dong, P.Minnis, and S.Sun-Mack (2014), Comparison of marine boundary layer cloud properties from CERES-MODIS Edition 4 and DOE ARM AMF measurements at the Azores, J. Geophys. Res.Atmos.,119, doi:10.1002/2014JD021813

Yao, M.-S., and Y. Cheng, 2012: Cloud simulations in response to turbulence parameterizations in the GISS Model E GCM. J. Climate, 25, 4963-4974, doi:10.1175/JCLI-D-11-00399.1.

Yoshimori, M., and A. J. Broccoli (2008), Equilibrium response of an atmosphere-mixed layer ocean model to different radiative forcing agents: Global and zonal mean response, J. Clim., 21, 4399–4423, doi:10.1175/2008JCLI2172.1.

Yoshimori, M., and A. J. Broccoli (2009), On the link between Hadley circulation changes and radiative feedback processes, Geophys. Res. Lett., 36, L20703, doi:10.1029/2009GL040488.

Young, D.F., P. Minnis, D.R. Doelling, G.G. Gibson, and T. Wong, 1998: Temporal Interpolation Methods for the Clouds and Earth's Radiant Energy System (CERES) Experiment. J. Appl. Meteorol., 37, 572-590.